

**Development and Application of Reliable
Methods for the Calculation of Excited States:
From Light-Harvesting Complexes to
Medium-Sized Molecules**

Dissertation
zur Erlangung des Doktorgrades
der Naturwissenschaften

vorgelegt beim Fachbereich 14
der Johann Wolfgang Goethe – Universität
in Frankfurt am Main

von
Michael Wormit
aus Speyer

Frankfurt, Januar 2009

vom Fachbereich FB 14 Biochemie, Chemie und Pharmazie der
Johann Wolfgang Goethe–Universität als Dissertation angenommen.

Dekan:

Gutachter:

Datum der Disputation:

In memory of my father.

Abstract

Photo-initiated processes, like photo-excitation and -deexcitation, internal conversion, excitation energy transfer and electron transfer, are of importance in many areas of physics, chemistry and biology. For the understanding of such processes, detailed knowledge of excitation energies, potential energy surfaces and excited state properties of the involved molecules is an essential prerequisite. To obtain these informations, quantum chemical calculations are required. Several quantum chemical methods exist which allow for the calculation of excited states. Most of these methods are computationally costly what makes them only applicable to small molecules. However, many biological systems where photo-processes are of interest like light-harvesting complexes in photosynthesis or the reception of light in the human eye by rhodopsin are quite large. For large systems, however, only few theoretical methods remain applicable. The currently most widely used method is time-dependent density functional theory (TD-DFT), which can treat systems of up to 200–300 atoms with the excitation energies of some excited states exhibiting errors of less than 0.5 eV. Yet, TD-DFT has several drawbacks. The most severe failure of TD-DFT is the false description of charge transfer states which is particularly problematic in case of larger systems where it yields a multitude of artificially low-lying charge transfer states. But also Rydberg states and states with large double excitation character are not described correctly. Still, if these deficiencies are kept in mind during the interpretation of results, TD-DFT is a useful tool for the calculation of excited states.

In my thesis, TD-DFT is applied in investigations of excitation energy and electron transfer processes in light-harvesting complexes. Since light-harvesting complexes, which consist of thousands of atoms, are by far too large to be calculated, model complexes for the processes of interest are constructed from available crystal structures. The model complexes are used to calculate potential energy curves along meaningful reaction coordinates. Artificial charge transfer states are corrected with the help of the so-called Δ DFT method. The resulting potential energy curves are then interpreted by comparison with experimental results.

For the light-harvesting complex LH2 from purple bacteria the experimentally observed formation of carotenoid radical cations is studied. It is shown that the carotenoid radical cation is formed most likely via the optically forbidden S_1 state of the carotenoid. In light-harvesting complex LHC-II of green plants the fast component of the so-called non-photochemical quenching (NPQ) is investigated. Two of several different hypotheses on the mechanism of NPQ, which have been proposed recently, are studied in detail. The first one suggests that NPQ proceeds via simple replacement of violaxanthin by zeaxanthin in the binding pocket in LHC-II. However, the calculated potential energy curves exhibit no difference between violaxanthin and zeaxanthin in the binding pocket. In combination with experimental results it is thus shown that simple replacement alone does not mediate NPQ in LHC-II. The second hypothesis proposes conformational changes

of LHC-II that lead to quenching at the central lutein and chlorophyll molecules during NPQ. My TD-DFT calculations demonstrate that if this mechanism is operative, only the lutein 1 which is one of two central luteins present in LHC-II can take part in the quenching process. This is corroborated by recent experiments.

Though several conclusions can be drawn from the investigations using TD-DFT, the interpretability of the results is limited due to the deficiencies of the method and of the models. To overcome the methodological deficiencies, more accurate methods have to be employed. Therefore, the so-called algebraic diagrammatic construction scheme (ADC) is implemented. ADC is a widely overlooked *ab initio* method for the calculation of excited states, which is based on propagator theory. Its theoretical derivation proceeds via perturbation expansion of the polarization propagator, which describes electronic excitations. This yields separate schemes for every order of perturbation theory. The second order scheme ADC(2), which is employed here, is the equivalent to the Møller-Plesset ground state method MP(2), but for excited states. It represents the computationally cheapest excited state method which can correctly describe doubly excited states, as well as Rydberg and charge transfer states. The quality of ADC(2) results is demonstrated in calculations on linear polyenes which serve as model systems for the larger carotenoid molecules. The calculations show that ADC(2) describes the three lowest excited states of polyenes sufficiently well, particularly the optically forbidden S_1 state which is known to possess large double excitation character. Yet, the applicability of the method is limited compared to TD-DFT due to the much larger computational requirements.

To facilitate the calculation of larger systems with ADC(2) a new variant of the method is developed and implemented. The variant employs the short-range behavior of electron correlation to reduce the computational effort. As a first step, the working equations of ADC(2) are transformed into a basis of local orbitals. In this basis negligible contributions of the equations which are due to electron correlation can be identified based on the distances of local orbitals. A so-called “bumping” scheme is implemented which removes the negligible parts during a calculation. This way, the computation times as well as the disk space requirements can be reduced. With the “bumping” scheme several new parameters are introduced that regulate the amount of “bumping” and thereby the speed and the accuracy of computations. To determine useful values for the parameters an evaluation is performed using the linear polyene octatetraene as test molecule. From the evaluation an optimal set of parameter values is obtained, so that the computation times become minimal, while the errors in the excitation energies due to the “bumping” do not exceed 0.15 eV. With further calculations on various molecules of different sizes it is tested if these parameter values are universal, i.e. if they can be used for all molecules. The test calculations show that the errors in the excitation energies are below 0.15 eV for all test systems. Additionally, no trend is visible for the errors that their magnitude might depend on the system. In contrast, the amount of disregarded contributions in the calculations increases drastically with growing system size. Thus, the local variant of ADC(2) can be used in future to reliably calculate excited states of systems which are not accessible with conventional ADC(2).

Zusammenfassung

Lichtinduzierte Prozesse, wie Absorption, Emission, interne Konversion und Energie- und Elektronentransfer, sind in vielen Bereichen von Physik, Chemie und Biologie von Bedeutung. Zum Verständnis solcher Prozesse ist die genaue Kenntnis von Anregungsenergien, Potentialenergieflächen und Eigenschaften angeregter Zustände unabdingbar. Zum Erwerb dieser Informationen werden quantenchemische Verfahren benötigt, die die Berechnung angeregter Zustände erlauben. Die meisten der entsprechenden Methoden sind aufgrund ihrer Hardware-Anforderungen nur auf kleine Moleküle anwendbar. Viele der hier interessierenden Systeme, wie z.B. die Lichtsammelkomplexe in Pflanzen oder das Rhodopsin im menschlichen Auge, sind jedoch sehr groß, so dass nur wenige Methoden für die Berechnung dieser Systeme in Frage kommen. Eine häufig verwendete Methode ist die zeitabhängige Dichtefunktionaltheorie (TD-DFT), mit deren Hilfe sich Systeme von bis zu 200–300 Atomen berechnen lassen, ohne dass die Fehler in den Anregungsenergien mancher Zustände 0.5 eV überschreiten. Allerdings, hat TD-DFT auch einige Nachteile. Der schwerwiegendste davon ist das Versagen bei der Berechnung von Ladungstransferzuständen, was besonders für große Systeme zu einer Fülle solcher Zustände mit viel zu niedrigen Anregungsenergien führt. Desweiteren können auch sogenannte Rydberg-Zustände und Zustände mit starkem Doppelanregungscharakter nicht richtig beschrieben werden. Trotzdem lässt sich die Methode gut zur Berechnung von angeregten Zuständen einsetzen, wenn man bei der Interpretation der entsprechenden Ergebnisse die vorhandenen Probleme berücksichtigt.

In dieser Arbeit wird TD-DFT zur Untersuchung von Energie- und Elektronentransferprozessen in Lichtsammelkomplexen eingesetzt. Da Lichtsammelkomplexe mit ihren weit über 1000 Atomen auch für TD-DFT viel zu groß sind, werden zunächst anhand von Röntgenstrukturen Modellkomplexe für die jeweiligen Prozesse konstruiert. Mit diesen werden dann Potentialenergiekurven entlang geeigneter Reaktionskoordinaten berechnet. Die dabei auftretenden, schon erwähnten artifiziellen Ladungstransferzustände werden mit Hilfe der sogenannten Δ DFT-Methode korrigiert bzw. aussortiert. Durch Vergleich mit experimentellen Daten lassen sich die Potentialenergiekurven interpretieren.

Beim in Purpurbakterien vorkommenden Lichtsammelkomplex LH2 wurde die photoinduzierte Bildung von Radikalkationen von Karotenoiden theoretisch studiert. Dabei zeigt sich, dass die Radikalkationen höchstwahrscheinlich über die S_1 Zustände der jeweiligen Karotenoide entstehen. Desweiteren wurde der Mechanismus des nicht-photochemischen Quenchens (NPQ) in Lichtsammelkomplexen LHC-II von Pflanzen untersucht. Für den NPQ werden verschiedene mögliche Prozesse diskutiert, von denen hier zwei betrachtet wurden. Bei dem einen soll NPQ schon durch bloßen Austausch von Violaxanthin gegen Zeaxanthin in der Bindungstasche des LHC-II ablaufen. Allerdings zeigen die berechneten Potentialenergiekurven für Violaxanthin und Zeaxanthin keine entsprechenden Unterschiede. Daher lässt sich, gestützt durch weitere experimentelle Befunde, folgern, dass dieser einfache Mechanismus für NPQ nicht in Frage kommt.

Beim zweiten Prozess lässt eine Konformationsänderung des LHC-II das Quenchen an den zentralen Lutein- und Chlorophyll-Molekülen stattfinden. Aus den Rechnungen dazu ergibt sich, dass, sollte dies der maßgebliche Mechanismus für NPQ sein, höchstens eins der zwei zentralen Luteine im LHC-II, das Lutein 1, am Quenchen teilnehmen kann.

Trotz der obigen, aus TD-DFT-Rechnungen gewonnenen Erkenntnisse, bleibt die Interpretierbarkeit der Ergebnisse aufgrund der Unzulänglichkeiten der Methode und den stark vereinfachten Modellen doch beschränkt. Um die Probleme von TD-DFT zu umgehen, ist die Verwendung genauerer Methoden unausweichlich. Daher wurde hier als genauere Methode zur Berechnung angeregter Zustände die algebraisch-diagrammatische Konstruktion (ADC) weiterentwickelt. ADC ist eine weitgehend übersehene *ab initio*-Methode zur Berechnung angeregter Zustände, die auf dem Propagator-Formalismus beruht. Die Herleitung der Methode erfolgt über die störungstheoretische Entwicklung des Polarisationspropagators, der elektronische Anregungen beschreibt. Dabei ergibt sich für jede Ordnung der Störungstheorie eine neue Variante von ADC. In zweiter Ordnung ist das die im Folgenden verwendete ADC(2)-Methode. Sie entspricht für angeregte Zustände in etwa dem, was die bekannte Møller-Plesset-Störungstheorie MP(2) für Grundzustände darstellt. ADC(2) ist außerdem die am wenigsten aufwändige Methode, mit der doppelt angeregte Zustände, als auch Rydberg- und Ladungstransferzustände prinzipiell richtig beschrieben werden können. Die Qualität der ADC(2)-Ergebnisse wird in dieser Arbeit durch Rechnungen an linearen Polyenen demonstriert, die als Modelle für Karotenoide dienen. Die dabei erhaltenen, niedrigsten drei angeregten Zustände weisen eine ausreichende Genauigkeit auf. Allerdings lässt sich ADC(2) aufgrund des erhöhten Rechenaufwands nur auf wesentlich kleinere Systeme anwenden als TD-DFT.

Um auch größere Systeme mit ADC(2) beschreiben zu können, habe ich in meiner Arbeit eine neue lokale Variante von ADC(2) entwickelt und implementiert. Diese Variante nutzt die Kurzreichweitigkeit der Elektronenkorrelation, um Rechenaufwand zu verringern. Für die Implementierung der Variante wurden die ADC-Gleichungen zunächst in eine Basis aus lokalen Orbitalen transformiert. In dieser Basis können mit Hilfe eines sogenannten „Bumping“-Schemas Teile der Berechnungen aufgrund des Abstandes der lokalen Orbitale vernachlässigt werden, was sowohl Rechenzeit verkürzt, als auch benötigten Speicher reduziert. Die Einführung des „Bumping“-Schemas resultiert in einer Reihe zusätzlicher Parameter. Diese Parameter sollten so gewählt sein, dass möglichst viel vernachlässigt werden kann, ohne dass jedoch der durch das „Bumping“-Schema verursachte Fehler in den Anregungsenergien 0.15 eV übersteigt. Ein Satz optimaler Parameterwerte wurde mittels Rechnungen an *trans*-Octatetraen bestimmt. Anschließend wurde die Qualität der Parameterwerte durch Rechnungen an mehreren, verschieden großen Molekülen überprüft. Dabei zeigt sich, dass die Fehler in den Anregungsenergien unabhängig vom Molekül etwa konstant bleiben. Gleichzeitig lässt sich bei den Rechnungen mit wachsender Systemgröße aber immer mehr vernachlässigen. Daher können mit der neuen, lokalen Variante von ADC(2) Rechnungen an Systemen durchgeführt werden, die mit dem konventionellen Verfahren nicht möglich sind, ohne dass dabei die Qualität der Ergebnisse leidet.

Contents

1	German Summary	1
2	Introduction	7
3	Theoretical Methods	13
3.1	Basic Approximations	13
3.1.1	Born-Oppenheimer Approximation	13
3.1.2	Self-consistent Field Methods	15
3.1.3	Electron Correlation	20
3.2	CIS and TD-DFT	26
3.2.1	Configuration Interaction Singles	26
3.2.2	Time-Dependent Density Functional Theory	27
3.2.3	Calculating Charge Transfer States	31
3.3	Algebraic Diagrammatic Construction	33
3.3.1	Theoretical Foundations	33
3.3.2	Implementation of ADC(2)	45
3.3.3	Local ADC	51
4	Applications	61
4.1	Energy and Electron Transfer Processes in Photosynthesis	61
4.1.1	Quantum Chemical Approach	62

4.1.2	Light-Harvesting Complex 2 in Purple Bacteria	65
4.1.3	Light-Harvesting Complex 2 in Green Plants	78
4.2	Calculations on Model Systems using ADC	89
4.2.1	Linear Polyenes	90
4.2.2	Model Systems for Local ADC	95
5	Conclusions and Outlook	107
5.1	Energy and Electron Transfer Processes in Photosynthesis	107
5.2	ADC Calculations on Model Systems	109
A	Algebraic Diagrammatic Construction	111
A.1	The Original ADC Equations	111
A.2	Multiplying the ADC Matrix	115
A.3	ADC in Spin Components	116
A.4	Restricted ADC Equations	122
B	Molecular Parameters	125
B.1	Molecules Employed in Section 4.2.2	125

List of Tables

4.1	Evaluation of model complexes for LH2	68
4.2	Evaluation of bumping models on C ₈ H ₁₀ using ADC(2)	97
4.3	Bumping information for various molecules	102
4.4	Comparison of vertical excitation energies of various molecules . . .	105

List of Figures

3.1	Building blocks of Feynman diagrams	39
3.2	Feynman diagrams of the polarization propagator	40
3.3	Functions employed to determine the bumping	55
3.4	Bumping models	58
4.1	Structure of LH2 of <i>Rps. acidophila</i>	66
4.2	Structures of chromophores in LH2	67
4.3	β Arg ₂₀ -BChl model complex.	70
4.4	Intermolecular distance coordinate R in LH2 model complexes . . .	71
4.5	Attachment and detachment densities of Car-BChl complex	72
4.6	Potential energy curves of Car-BChl model complexes	73
4.7	Energy level diagram of Car-BChl complexes	76
4.8	Structure of LHC-II of green plants	78
4.9	Structures of chromophores in LHC-II relevant for NPQ	80
4.10	Structure of Vio-Chl 9 α -Tyr24	82
4.11	Potential energy curves of Vio-Chl and Zea-Chl model complexes .	83
4.12	Structure of the Lut1 and Lut2 model complexes	87
4.13	Potential energy curves of Lut-Chl model complexes	88
4.14	Structure of polyenes.	90
4.15	Lowest excited states of all- <i>trans</i> polyenes	92

4.16	Neglected doubles as function of bumping distance on C_8H_{10}	98
4.17	Evaluation of the bumping distance on C_8H_{10}	99
4.18	Deviations in oscillator strength using local ADC on C_8H_{10}	100

Kapitel 1

Deutsche Zusammenfassung

Das Hauptthema dieser Arbeit ist die theoretische Beschreibung von elektronisch angeregten Zuständen mittelgroßer und großer molekularer Systeme mit Hilfe von quantenchemischen Methoden. Dabei stehen besonders die Qualität der erhaltenen Resultate und deren Interpretierbarkeit im Vordergrund.

Angeregte Zustände spielen bei allen Arten von lichtinduzierten Prozessen, wie Absorption, Fluoreszenz, Phosphoreszenz, interne Konversion, Energie- und Elektronentransfer, eine entscheidende Rolle. Solche Prozesse treten sowohl in der Natur, als auch in technischen Anwendungen auf. Beispiele sind die Energietransferprozesse in der Photosynthese nach Absorption von sichtbarem Licht, die Wahrnehmung von Licht durch das menschliche Auge, der Start von Polymerisationsreaktionen durch Lichtabsorption oder die Erzeugung von Elektrizität in Solarzellen. Zum theoretischen Verständnis dieser Prozesse ist die genaue Kenntnis von Anregungsenergien, Potentialenergieflächen und Eigenschaften der beteiligten angeregten Zustände unabdingbar. Um diese Informationen über die relevanten angeregten Zustände zu erhalten, werden quantenchemische Verfahren benötigt. Heutzutage stehen viele verschiedene quantenchemische Methoden zur Verfügung, die die numerische Berechnung angeregter Zustände erlauben. Allerdings sind die meisten dieser Methoden aufgrund ihrer Anforderungen an die Computerhardware nur auf kleine Moleküle anwendbar. Viele Systeme, in denen die genannten Prozesse ablaufen, sind jedoch häufig sehr groß, so dass nur wenige Methoden zur Berechnung der angeregten Zustände in Frage kommen. Diese Methoden sind meist stark genähert, so dass die erhaltenen Resultate nur nach detaillierter Evaluation zur

Interpretation von experimentellen Beobachtungen verwendet werden können.

Eine der für große Systeme am häufigsten verwendeten Methoden ist die zeitabhängige Dichtefunktionaltheorie (TD-DFT). Mit ihrer Hilfe lassen sich Moleküle mit mehreren hundert Atomen ohne weiteres beschreiben. Die erhaltenen Anregungsenergien weisen dabei für viele Zustände Fehler von weniger als 0.5 eV auf, was eine akzeptable Abweichung darstellt. Leider versagt TD-DFT bei der Berechnung bestimmter Zustände völlig. Dazu gehören die Ladungstransferzustände, Rydberg-Zustände und Zustände mit starkem Doppelanregungscharakter. Die fehlerhafte Berechnung von Ladungstransferzuständen führt besonders bei typischen Donor-Akzeptor-Systemen und bei großen Systemen zu einer Fülle solcher Zustände mit artifiziell niedrigen Anregungsenergien. Die Probleme von TD-DFT bei der Beschreibung von angeregten Zuständen mit starkem Doppelanregungscharakter treten speziell bei großen konjugierten Systemen, wie z.B. den Karotenoiden in Lichtsammelkomplexen zutage. Hier werden zwar die Anregungsenergien teilweise aufgrund von vorhandener Fehlerkompensation noch gut beschrieben, diese ist aber für weitere Eigenschaften nur bedingt gegeben. Trotz der Schwierigkeiten lässt sich TD-DFT zur Berechnung von angeregten Zuständen einsetzen, wenn man bei der Interpretation der Ergebnisse die vorhandenen Probleme berücksichtigt.

In dieser Arbeit wird TD-DFT zur Untersuchung von Energie- und Elektronentransferprozessen in Lichtsammelkomplexen eingesetzt. Da Lichtsammelkomplexe aus weit über 1000 Atomen bestehen, ist es notwendig Modellkomplexe für die jeweiligen Prozesse zu konstruieren, um mit TD-DFT quantenchemische Rechnungen durchführen zu können. Die Modellkomplexe werden auf Basis von Röntgenstrukturen durch Ausschneiden der relevanten Pigmentmoleküle erzeugt. Danach werden Ungenauigkeiten in den Röntgenstrukturen durch Optimierung der Komplexe ausgeglichen, ohne jedoch die prinzipielle Anordnung der Pigmentmoleküle zu zerstören. An den resultierenden Komplexen werden Potentialkurven entlang geeigneter Reaktionskoordinaten berechnet. Dabei treten eine Vielzahl der oben erwähnten artifiziellen Ladungstransferzustände auf, die mit Hilfe der sogenannten Δ DFT-Methode korrigiert bzw. aussortiert werden. Die korrigierten Potentialenergiekurven lassen sich dann durch Vergleich mit experimentellen Daten interpretieren.

Als erstes System wurde der Lichtsammelkomplex LH2 in Purpurbakterien bezüglich der Frage der Entstehung der Radikalkationen von Karotenoiden nach

Lichtabsorption theoretisch untersucht. Dazu wurden Komplexe bestehend aus einem Karotenoid und einem Bakteriochlorophyll konstruiert. Anhand von Rechnungen an mehreren solcher Komplexe zeigt sich, dass die Radikalkationen der Karotenoide höchstwahrscheinlich nach Population des schwingungsangeregten S_1 Zustands gebildet werden. Ebenso könnte der Prozess aber auch über den S^* Zustand ablaufen, der in den TD-DFT Rechnungen nicht gefunden wird.

Desweiteren wurde der Mechanismus des nicht-photochemischen Quenchens (NPQ) in Lichtsammelkomplexen LHC-II von Pflanzen studiert. Der genaue Ablauf dieses Prozesses ist weitgehend unklar. Mehrere Hypothesen zu NPQ, wo und wie er stattfindet, sind Thema aktueller Forschung. Zwei der Vorschläge wurden hier mit Hilfe von TD-DFT-Rechnungen theoretisch betrachtet. In der ersten Hypothese wird der bloße Austausch von Violaxanthin gegen Zeaxanthin in der Bindungstasche des LHC-II als Mechanismus für NPQ vorgeschlagen. Die Modellkomplexe für die entsprechenden TD-DFT-Rechnungen bestehen daher aus Violaxanthin bzw. Zeaxanthin und einem Chlorophyll. Anhand der erhaltenen Potentialenergiekurven lassen sich für Violaxanthin und Zeaxanthin keine signifikanten Unterschiede in der Bindungstasche des LHC-II erkennen. Daher ist es äußerst unwahrscheinlich, dass dieser einfache Mechanismus für NPQ in Frage kommt. Dies wird durch neuere experimentelle Befunde unterstützt. Der zweite untersuchte Vorschlag zum Mechanismus von NPQ beinhaltet eine Konformationsänderung des LHC-II, welche das Quenchen der Anregungsenergie an den zentralen Lutein- und Chlorophyll-Molekülen durch Änderung ihrer relativen Positionen ermöglichen soll. Zur Überprüfung dieser Hypothese wurden TD-DFT-Rechnungen an zwei unterschiedlichen Lutein-Chlorophyll-Modellkomplexen durchgeführt, die den zwei leicht verschiedenen, zentralen Lutein-Molekülen im LHC-II entsprechen. Die berechneten Potentialenergiekurven lassen keinen eindeutigen Schluss zu, ob der vorgeschlagene Mechanismus so abläuft. Allerdings lässt sich aus den Rechnungen folgern, dass nur eines der beiden Luteine, nämlich das Lutein 1, am Quenchen beteiligt sein kann, sollte der Mechanismus für NPQ maßgeblich sein.

Trotz dieser aus den TD-DFT-Potentialenergiekurven gewonnen Erkenntnisse ist die Interpretierbarkeit der Ergebnisse aufgrund der methodischen Probleme und der stark vereinfachten Modelle erheblich eingeschränkt. Um dies zu verbessern, sind zum einen bessere Modelle nötig, die auch den Einfluß der Proteinumgebung miteinbeziehen, zum anderen müssen genauere Methoden verwendet werden, um

die Schwierigkeiten von TD-DFT bei der Berechnung angeregter Zustände zu umgehen. Der Einfluss der Proteinumgebung lässt sich zum Beispiel durch ein Feld von Punktladungen als Modell für das Protein in den Rechnungen berücksichtigen. Dies soll in weiterführenden Forschungsarbeiten intensiv getestet werden. Einige erste Rechnungen mit Punktladungen als Proteinumgebung zeigen auch schon viel versprechende Ergebnisse.

Als genauere Methode zur Berechnung von angeregten Zuständen wurde in dieser Arbeit das algebraisch-diagrammatische Konstruktionsschema (ADC) weiterentwickelt, um es für große Systeme anwendbar zu machen. ADC ist eine weitgehend übersehene *ab initio*-Methode zur Berechnung elektronisch angeregter Zustände. Ihre Grundlagen beruhen auf dem Propagator-Formalismus für Vielteilchensysteme. Bei der Herleitung von ADC wird der Polarisationspropagator, der die elektronischen Anregungen beschreibt, als störungstheoretische Reihe entwickelt. Dadurch erhält man für jede Ordnung Störungstheorie eine neue Variante von ADC. In zweiter Ordnung ist das die im Folgenden verwendete ADC(2)-Methode, mit der die angeregten Zustände und ihre Anregungsenergien konsistent in zweiter Ordnung beschrieben werden. Damit stellt die Methode das Pendant für angeregte Zustände zur bekannten Møller-Plesset-Störungstheorie MP(2) für Grundzustandsrechnungen dar. Außerdem ist ADC(2) die Methode mit dem geringsten Rechenaufwand, die sowohl doppelt angeregte Zustände, als auch Rydberg- und Ladungstransferzustände prinzipiell richtig und konsistent beschreiben kann. Um die Qualität der von ADC(2) gelieferten angeregten Zustände zu bewerten, wurden zunächst Rechnungen an linearen Polyenen durchgeführt, die als Modellsysteme für die wesentlich größeren Karotenoide dienen. Dabei wurden die berechneten Anregungsenergien mit TD-DFT-Resultaten und experimentellen Werten verglichen. Es zeigt sich, dass die ADC(2)-Anregungsenergien der niedrigsten drei Zustände eine ausgesprochen hohe Genauigkeit aufweisen, die im Gegensatz zu TD-DFT nicht auf Fehlerkompensation zurückzuführen ist. Damit eignet sich ADC(2) gut für die Untersuchung von Modellkomplexen, welche Karotenoide enthalten. Allerdings lässt sich ADC(2) aufgrund des erhöhten Rechenaufwands im Gegensatz zu TD-DFT nicht auf so große Systeme anwenden.

Um ADC(2) auch für Rechnungen an größeren molekularen Systemen verwenden zu können, habe ich in meiner Arbeit eine neue, lokale Variante von ADC(2) entwickelt und implementiert. Diese Variante nutzt statt der kanonischen Hartree-

Fock-Orbitale eine neue Basis aus lokalen Orbitalen bei der Berechnung der angeregten Zustände. In dieser Basis lässt sich die Kurzreichweitigkeit der Elektronenkorrelation ausnutzen, um Rechenzeit und Speicherplatz zu reduzieren. Zunächst müssen allerdings die ADC-Gleichungen in die Basis der lokalen Orbitale transformiert werden. Danach kann die Lokalität der Orbitale benutzt werden, um Beiträge zu den Gleichungen, die von der Elektronenkorrelation herrühren und weit voneinander entfernten, lokalen Orbitalen zuzuordnen sind, zu vernachlässigen. Bei der Implementierung wurde dies durch ein sogenanntes „Bumping“-Schema erreicht, welches Beiträge basierend auf dem Abstand und der Ausdehnung der beteiligten Orbitale vorselektiert und auf Null setzt. Die Verwendung des „Bumping“-Schemas resultiert in einer Reihe zusätzlicher neuer Parameter, die bestimmen, wie viele und welche Beiträge während einer Rechnung vernachlässigt werden. Je nachdem wie die Parameter gewählt werden, können die Rechenzeiten kürzer oder länger, die Ergebnisse aber auch fehlerhafter oder genauer werden. Im besten Fall sollten durch die Wahl der Parameter gleichzeitig die Rechenzeit und die Fehler in den Ergebnissen minimiert werden. Um dies zu erreichen, wurden Testrechnungen mit verschiedenen Parameterwerten an *trans*-Octatetraen durchgeführt. Anhand der Ergebnisse wurde dann ein optimaler Satz an Parametern bestimmt, so dass möglichst viele Beiträge in einer Rechnung vernachlässigt werden, ohne dass der durch das „Bumping“-Schema verursachte Fehler in den Anregungsenergien 0.15 eV übersteigt. Die daraus resultierenden Parameterwerte wurden dann durch Rechnungen an mehreren, verschieden großen Molekülen auf ihre Qualität überprüft. Dabei stand im Vordergrund, dass sich mit den gegebenen Parameterwerten bei anderen Systemen der Fehler nicht vergrößert, während die Menge der vernachlässigten Beiträge mit wachsender Systemgröße steigt. Die Rechnungen an den Testmolekülen zeigen, dass der Fehler für alle Zustände bei den verwendeten Testsystemen unter den geforderten 0.15 eV bleibt, wobei die Größe der Abweichung zum Teil zustandsabhängig, aber nicht molekülabhängig ist. Außerdem steigt der Anteil der vernachlässigten Beiträge von 5% für die kleinsten Testmoleküle auf bis zu 33% für die größeren. Dies hängt allerdings nicht allein von der Größe, sondern auch von der Form des Moleküls ab. So lassen sich bei linearen Molekülen mehr Beiträge vernachlässigen als bei kompakteren. Insgesamt kann man aus den Testrechnungen folgern, dass mit der neuen, lokalen Variante von ADC(2) mit weniger Rechenaufwand Rechnungen an Systemen durchgeführt

werden können, ohne größere Fehler in den Ergebnissen zu erhalten. Dadurch lassen sich dann auch größere System berechnen, für die kanonisches ADC(2) nicht möglich ist.

Chapter 2

Introduction

The calculation of electronic excited states of molecules is one of the major concerns in contemporary quantum chemistry. The detailed knowledge of excitation energies, potential energy surfaces, and excited state properties of molecules is an essential ingredient in the theoretical description of absorption and emission of light, and of excitation energy and electron transfer processes. Such processes are of importance in many areas of physics, chemistry and biology. During photosynthesis, for example, the conversion of carbon dioxide into organic compounds is triggered by absorption of light and a subsequent series of excitation energy and electron transfer steps [1, 2]. Vision and color perception of animals and humans in the retina of the eye involves an isomerization process of the retinal pigment molecule in a protein called rhodopsin using the energy of a previously absorbed photon [3]. Other examples are photo-induced chemical reactions like polymerizations [4, 5], charge separation in quantum dots after absorption of a photon [6], conversion of solar energy to electricity in photovoltaic cells, or the potential use of photo-switchable molecules in medical applications.

When visible light is absorbed by a molecule, the energy of the photon promotes the molecule from its electronic ground state to an optically allowed excited state. Thereby, the molecule normally becomes also vibrationally excited. Subsequent photo-initiated processes strongly depend on the molecule in consideration and its surroundings. In the most simple cases the molecule relaxes within the electronic excited state towards the vibrational ground level at the minimum of the potential energy surface of the excited state. Eventually, it decays back to the electronic

ground state via fluorescence, i.e. emission of a photon. Then the molecule ends up in a vibrationally excited level of the ground state from which it can again cool down to the ground level. The absorbed and the emitted photon differ in energy due to the two cooling processes. This energy difference is visible in experimental measurements as Stokes shift between absorption and fluorescence spectra.

In more complicated systems additional energetically low-lying excited states might exist which provide competing pathways to fluorescence decay. If crossings of the potential energy surfaces of the initially excited state and other states are energetically accessible after excitation, the molecule can also decay radiationless to these states. Such decay processes can lead to isomerization, proton transfer, and other conformational changes of the molecule due to relaxation within the newly populated states. If the newly populated state is an optically forbidden, so-called dark state as it is often the case, no fluorescence from this state will be observed experimentally. Since the number of possible decay pathways, in general, grows with increasing molecular size, the excited state dynamics of the molecules become more and more complicated the larger the molecules are. The situation becomes even more complex, if other molecules possessing excited states with similar energies are located in the vicinity of the initially excited one. Then, excitation energy transfer or electron transfer processes between the molecules can occur in addition to fluorescence and radiationless decay on the excited molecule itself. In the end, the decay process will proceed along those pathways which exhibit the largest transition probabilities on their way.

Experimentally, the excited states of molecules can be studied by means of absorption and fluorescence spectroscopy. With these methods the observation of optically allowed states is straightforward. Signals of dark states, however, can hardly be detected. Only high-resolution fluorescence or two-photon absorption measurements can provide to some extent information about dark states. The invention of ultrafast spectroscopic techniques has enabled experimentalists to study excited state dynamics, and thereby also measure state transitions involving dark states. With methods like transient absorption spectroscopy [7] and fluorescence upconversion [8] having sub-picosecond time resolution most of the decay processes mentioned above can be observed [9–14]. In recent years, a multitude of physical, chemical and biological systems have been studied by these methods [15–19]. The resulting spectra are often quite complex and difficult to interpret, particu-

larly in case of the larger biological systems like light-harvesting complexes. Then, theoretical calculations become necessary to help with the interpretation of the experimental spectra.

To support the experimental findings by theoretical investigations, the relevant excited states of the systems must be identified and calculated using quantum chemical methods. However, highly accurate quantum chemical methods have huge computational requirements which limit the molecular size of the systems the methods can be applied to. At present, ground state calculations yielding accuracies of 0.05 eV in relative energies and of 1% in equilibrium geometries are feasible for molecules with approximately 20 atoms of the second row of the periodic table. For excited state methods the size of molecules which are computable is even smaller. Yet, systems in typical biological and chemical applications consist of hundreds and thousands of atoms with even more electronic and nuclear degrees of freedom. Thus, for the quantum chemical description of large systems one has to resort to approximate methods and molecular models. All relevant physical properties of the system in consideration must be incorporated in those models and methods, so that the processes of interest can be properly described. If the interest is only in the excitation and the subsequent ultra-fast decay processes, everything happens within a spatially localized region of the system, and along few nuclear coordinates of the excited pigment molecule. Thus, only one or two pigment molecules need to be included in the model, while most of the environment can be neglected. Such molecular models then comprise 30 to 300 atoms, and the excitation energies and transition moments of the model system can be calculated using an approximate excited states method.

In general, the excited state calculations are performed at the equilibrium geometries of the molecular ground state which has been obtained previously by ground state calculations. The resulting so-called vertical excitation energies specify the differences between the potential energy surfaces of ground and excited states at the given molecular geometry. In most cases they are good estimates of the excitation energies measured in absorption experiments. The calculations also yield the excitation energies of the dark states which are not observed experimentally. To obtain information on the excited state dynamics, multiple excited state calculations can be performed at different molecular geometries. The molecular geometries have to be chosen along suitable reaction coordinates, so that the

resulting cut-outs of the potential energy surfaces of the system will exhibit the relevant crossings via which the decay pathways of the excited state dynamics proceed.

Today, several quantum chemical approaches exist which facilitate the calculation of excited states and their properties. They can be grouped into wave function-based, semi-empirical and density functional-based methods. When it comes to application to large molecular systems, however, most of them must be excluded, since they are too expensive with respect to their computational costs. Among the remaining methods, there are many semi-empirical methods [20–22], configuration interaction singles [23, 24], time-dependent Hartree-Fock [25], and complete active space self-consistent field [26, 27] as wave function-based methods, and time-dependent density functional theory [28, 29] as density functional based method. All of them can be applied to systems of up to at least 300 atoms. Though, this is in principle possible, the application of the methods is hampered by serious drawbacks. Large errors in excitation energies, wrongly described classes of excited states, or the requirement of *a priori* knowledge about the excited states of the systems necessitate extensive testing of the obtained excited states against experimental data to allow for thorough interpretation of the results. More reliable methods can be employed if only medium-sized systems need to be considered. In this regime, excitation energies with errors of less than 0.4 eV can be obtained for molecules with 20–40 atoms. Among the respective methods are several coupled cluster methods, and the algebraic diagrammatic construction schemes of second order. To have the quality of these methods also available at larger system sizes, several attempts have been recently made to reduce the computational costs of the methods [30, 31]. One of the most promising approaches is to employ the locality of electron correlation effects which are most expensive to calculate, and thereby to reduce the complexity of the calculation without losing much of the accuracy. This route has also been followed in this work for developments of the algebraic diagrammatic construction schemes.

This thesis is organized as follows. In Chapter 3, the basic approximations inherent in every quantum chemical calculation are introduced. Then, the theoretical foundations of the excited state methods configuration interaction singles and time-dependent density functional theory are outlined. Thereby, also the drawbacks of these methods are discussed. In the last part of this chapter the

algebraic diagrammatic construction scheme is derived. The working equations for its second order variants are given, and it is shown how these equations have been modified to extend the applicability of the method to larger systems. The subsequent chapter covers the applications of the described excited state methods to various systems. First, the works on excitation energy and electron transfer processes in light-harvesting complexes of plants and purple bacteria using TD-DFT and CIS is presented. Afterwards, the application of conventional and local ADC to several test systems is described. We close with some conclusions and an outlook on further developments.

Chapter 3

Theoretical Methods

Quantum chemical calculations always deal with the solution of the molecular time-independent Schrödinger equation. This highly dimensional, non-linear differential equation is not solvable analytically. Several approximations have to be introduced to facilitate numerical calculations. This chapter gives a short overview of the basic approximations which are inherent in most quantum chemical methods. Afterwards, excited state methods which are topic of this work will be described.

Throughout this chapter the equations will be given in atomic units with the Planck constant \hbar , the elementary charge e , the electron mass m_e and the speed of light c set to 1. If not stated otherwise, upper-case letters will represent nuclear parameters, like nuclear charge Z and mass M , while lower-case letters will be reserved for electronic parameters.

3.1 Basic Approximations

3.1.1 Born-Oppenheimer Approximation

A first step towards the solution of the full molecular Schrödinger equation

$$\left[-\sum_I \frac{1}{2M_I} \nabla_I^2 - \sum_i \frac{1}{2} \nabla_i^2 - \sum_{i,I} \frac{Z_I}{|\mathbf{r}_i - \mathbf{R}_I|} + \frac{1}{2} \sum_{i,j} \frac{1}{|\mathbf{r}_i - \mathbf{r}_j|} + \frac{1}{2} \sum_{I,J} \frac{Z_I Z_J}{|\mathbf{R}_I - \mathbf{R}_J|} \right] |\Phi(\mathbf{r}, \mathbf{R})\rangle = E |\Phi(\mathbf{r}, \mathbf{R})\rangle \quad (3.1)$$

is the separation of electronic and nuclear coordinates. An electronic Schrödinger equation is constructed by considering only those terms in equation (3.1) which depend on electronic coordinates \mathbf{r} , and the nuclear coordinates \mathbf{R} as fixed parameters:

$$\underbrace{\left[-\sum_i \frac{1}{2} \nabla_i^2 - \sum_{i,I} \frac{Z_I}{|\mathbf{r}_i - \mathbf{R}_I|} + \sum_{i,j} \frac{1}{|\mathbf{r}_i - \mathbf{r}_j|} \right]}_{\hat{\mathcal{H}}_{\text{el}}} |\Psi(\mathbf{r}|\mathbf{R})\rangle = E^{\text{el}}(\mathbf{R}) |\Psi(\mathbf{r}|\mathbf{R})\rangle \quad (3.2)$$

Finding one or multiple solutions to this equation is subject to most quantum chemical methods and will be the topic of the following sections.

But before, let us assume that one could obtain the exact solutions $|\Psi_i(\mathbf{r}|\mathbf{R})\rangle$ and $E_i^{\text{el}}(\mathbf{R})$ to equation (3.2) for all points in nuclear coordinate space. Then, the full Schrödinger equation could still be solved without approximation by using

$$|\Phi_\alpha(\mathbf{r}, \mathbf{R})\rangle = \sum_j |\Lambda_\alpha^j(\mathbf{R})\rangle |\Psi_j(\mathbf{r}|\mathbf{R})\rangle \quad (3.3)$$

as ansatz for the complete wave function. Plugging this into equation (3.1) and projecting onto $\langle \Psi_i(\mathbf{r}|\mathbf{R}) |$ yields the nuclear Schrödinger equation

$$\begin{aligned} & \left[-\sum_I \frac{1}{2M_I} \nabla_I^2 + E_i^{\text{el}}(\mathbf{R}) + \sum_{I,J} \frac{Z_I Z_J}{|\mathbf{R}_I - \mathbf{R}_J|} \right] |\Lambda_\alpha^i(\mathbf{R})\rangle \\ & - \sum_j \left[\sum_I \frac{1}{2M_I} \langle \Psi_i(\mathbf{r}|\mathbf{R}) | \nabla_I^2 | \Psi_j(\mathbf{r}|\mathbf{R}) \rangle \right] |\Lambda_\alpha^j(\mathbf{R})\rangle \\ & - \sum_j \left[\sum_I \frac{1}{M_I} \langle \Psi_i(\mathbf{r}|\mathbf{R}) | \nabla_I | \Psi_j(\mathbf{r}|\mathbf{R}) \rangle \nabla_I \right] |\Lambda_\alpha^j(\mathbf{R})\rangle = E |\Lambda_\alpha^i(\mathbf{R})\rangle. \quad (3.4) \end{aligned}$$

Its solutions are the missing terms in the solution to the full Schrödinger equation.

At this point, the Born-Oppenheimer approximation is introduced by neglecting the last two terms on the left-hand side in equation (3.4). The total potential energy of a molecule then becomes

$$E_j^{\text{tot}}(\mathbf{R}) = E_j^{\text{el}}(\mathbf{R}) + \sum_{I,J} \frac{Z_I Z_J}{|\mathbf{R}_I - \mathbf{R}_J|} \quad (3.5)$$

and the ansatz for the full wave function reduces to a simple product of a nuclear and an electronic wave function. This means the nuclei are treated moving in an external potential created by all electrons, but independently of the motion of individual electrons.

Obviously, the approximation is valid if the change in the electronic wave function with respect to the nuclear coordinates is negligible compared to the nuclear mass. In general, this is the case for energetically well separated electronic states. However, there are always regions in nuclear coordinate space where two electronic states approach each other, e.g. near conical intersections, avoided crossings, etc. Such regions occur more frequently the higher the energies of the electronic states become. There, the picture of nuclei moving in external potentials created by the electrons becomes invalid. This shall be kept in mind for later discussions of potential energy surfaces of electronic states $E_j^{\text{tot}}(\mathbf{R})$.

3.1.2 Self-consistent Field Methods

The next step after separating electronic and nuclear coordinates is the solution of the electronic Schrödinger equation (3.2). Still this equation is too complicated to be solved analytically. Thus, the concern of all quantum chemical methods is to introduce a set of approximations which yields good estimates to electronic states and energies.

The most basic approaches to obtain an estimate to the electronic ground state are Hartree-Fock (HF) and Kohn-Sham density functional theory (DFT). They can be summarized as self-consistent field (SCF) methods which are the basis of many other ground and excited state methods. The basic idea of self-consistent field methods is to transform the Schrödinger equation (3.2) for N electrons into a set of N differential equations, one for each electron. The individual electrons are then described by single-electron wave functions (orbitals). Due to the electron-electron interaction potential the single-electron equations are coupled, i.e. every equation implicitly depends on the orbitals of all electrons. Thus, the solutions for the single-electron orbitals have to be found in a way that they are consistent with the single-electron orbitals used to calculate the electron-electron interaction potential.

The transformation of the electronic Schrödinger equation to a set of single-

electron equations differs for HF and DFT. Yet, both methods assume that an N -electron wave function $|\Psi_0\rangle$ can be expressed as an anti-symmetrized product of single-electron orbitals $\phi_p(\mathbf{r})$, which is a Slater determinant

$$\Psi_0(\mathbf{r}_1, \dots, \mathbf{r}_N) = \frac{1}{\sqrt{N!}} \begin{vmatrix} \phi_1(\mathbf{r}_1) & \dots & \phi_1(\mathbf{r}_N) \\ \vdots & \ddots & \vdots \\ \phi_N(\mathbf{r}_1) & \dots & \phi_N(\mathbf{r}_N) \end{vmatrix}. \quad (3.6)$$

A variational principle guarantees in both cases that any change in the orbitals which lowers the energy of the system yields a better estimate to the ground state energy.

Hartree-Fock

In Hartree-Fock the variational principle is employed in the minimization of the expectation value of the electronic Hamiltonian $\langle \Psi_0 | \hat{\mathcal{H}}_{\text{el}} | \Psi_0 \rangle$. The minimization is performed by variation of the single-electron orbitals in $\langle \Psi_0 |$ which have to obey the constraints $\int d\mathbf{r} \phi_i^*(\mathbf{r}) \phi_j(\mathbf{r}) = \delta_{ij}$. As result, the Hartree-Fock equations for the single-electron orbitals are obtained, and eq. 3.2 reduces to

$$\left[-\frac{1}{2}\nabla^2 - \sum_I \frac{Z_I}{|\mathbf{r} - \mathbf{R}_I|} \right] \phi_i(\mathbf{r}) + \sum_{j=1}^N \int d\mathbf{r}' \frac{\phi_j^*(\mathbf{r}') \phi_j(\mathbf{r}')}{|\mathbf{r} - \mathbf{r}'|} \phi_i(\mathbf{r}) - \sum_{j=1}^N \int d\mathbf{r}' \frac{\phi_j^*(\mathbf{r}') \phi_i(\mathbf{r}')}{|\mathbf{r} - \mathbf{r}'|} \phi_j(\mathbf{r}) = \epsilon_i \phi_i(\mathbf{r}), \quad i = 1, \dots, N \quad (3.7)$$

with ϵ_i being the Lagrange multipliers to enforce the constraints on the single-electron orbitals. They are normally referred to as orbital energies. The set of single-electron orbitals $\phi_i(\mathbf{r})$ which are the self-consistent solutions to the HF equations can be used to calculate the HF ground state energy

$$E_{\text{HF}} = \sum_i h_{ii} + \frac{1}{2} \sum_{i,j} \underbrace{[\langle ij|ij\rangle - \langle ij|ji\rangle]}_{=\langle ij||ij\rangle} = \sum_i \epsilon_i - \frac{1}{2} \sum_{i,j} \langle ij||ij\rangle. \quad (3.8)$$

with

$$h_{ii} = \int d\mathbf{r} \phi_i^*(\mathbf{r}) \left[-\frac{1}{2} \nabla^2 - \sum_I \frac{Z_I}{|\mathbf{r} - \mathbf{R}_I|} \right] \phi_i(\mathbf{r})$$

$$\langle ij | ij \rangle = \int d\mathbf{r} d\mathbf{r}' \frac{\phi_i^*(\mathbf{r}) \phi_j^*(\mathbf{r}') \phi_j(\mathbf{r}') \phi_i(\mathbf{r})}{|\mathbf{r} - \mathbf{r}'|}$$

E_{HF} differs from the exact ground state energy E_0 by a contribution normally called correlation energy $E_{\text{corr}} = E_0 - E_{\text{HF}}$. This is due to the partial disregard of the electron-electron interaction potential in the Hartree-Fock approach. The last two terms on the left-hand side of the HF equations (3.7) result from the electron-electron interaction potential. They only describe the electron-electron interaction as an interaction of each electron with the Coulomb field created by the static charge distribution of all other electrons. Dynamic effects due to the movement of the electrons are neglected. Thus, the Hartree-Fock approach is often called mean-field approach.

Density functional theory

Density functional theory derives the set of single-electron equations in a different manner and thereby tries to avoid the problem of electron correlation. Based on the Hohenberg-Kohn theorems [32] which provide proofs of existence for a ground state energy functional of the density $E[\rho]$, and for a variational principle to this functional, an artificial system of non-interacting electrons in some external potential v_s is introduced [33]. For such system the solutions of the single-electron equations (Kohn-Sham equations)

$$\left[-\frac{1}{2} \nabla^2 + v_s(\mathbf{r}) \right] \phi_i(\mathbf{r}) = \epsilon_i \phi_i(\mathbf{r}), \quad i = 1, \dots, N \quad (3.9)$$

yield the exact wave function and density, since the correlation energy is zero by definition. Now, it is assumed that for any interacting system there exist a non-interacting system which shares the same ground state density

$$\rho_0(\mathbf{r}) = \rho_0^s(\mathbf{r}) = \sum_i |\phi_i(\mathbf{r})|^2. \quad (3.10)$$

Thus, finding the solutions of the non-interacting system also yields the exact solutions of the corresponding interacting system. Only the external potential v_s for the non-interacting system has to be determined so that it recovers all many-particle effects of the interacting system. Certainly, the external potential must comprise the electron-nuclear interaction and the mean-field Coulomb interaction of the electrons. All other effects due to the electron correlation are less obvious. They are gathered in the so-called exchange-correlation (xc) potential which is a functional of the density:

$$v_s(\mathbf{r}) = - \sum_I \frac{Z_I}{|\mathbf{r} - \mathbf{R}_I|} + \underbrace{\int d\mathbf{r}' \frac{\rho(\mathbf{r}')}{|\mathbf{r} - \mathbf{r}'|}}_{v_H([\rho], \mathbf{r})} + v_{xc}([\rho], \mathbf{r}). \quad (3.11)$$

An exact expression for the xc potential has not been found yet. This prevents the calculation of the exact density of the interacting system. However, there exist several approximations for the xc potential, like LDA [34], BLYP [35], B3LYP [36, 37] or BP86 [38], which may yield good estimates of the ground state density depending on the system in consideration.

We should note that the approximation of the xc potential does not obey any variational principle: The DFT ground state energy is an upper bound to the exact ground state energy of the model Hamiltonian formed by the xc potential, but not to the full Hamiltonian in the molecular Schrödinger equation. Thus, the DFT ground state energy can be lower than the exact ground state energy what necessitates the evaluation of approximated xc potentials for the systems of interest.

Basis Sets

Up to now, we have only stated that the single-electron equations in HF and DFT have to be solved self-consistently, but not how this is done in numerical practice. The simplest way to do so is to expand the single-electron orbitals in a set of basis functions (basis set)

$$\phi_p(\mathbf{r}) = \sum_{\mu} C_{\mu p} \chi_{\mu}(\mathbf{r}). \quad (3.12)$$

Typical basis sets are plane waves (solid state calculations) or nucleus-centered Gaussian-type orbitals (GTO).

With this expansion the single-electron equations can be solved by adjusting the coefficients $C_{\mu p}$ to optimal values. This transforms the single-electron differential equations into a matrix equation which can be solved numerically.

$$\sum_{\nu} F_{\mu\nu} C_{\nu p} = \sum_{\nu} S_{\mu\nu} C_{\nu p} \epsilon_p \quad (3.13)$$

$$\mathbf{FC} = \mathbf{SC}\epsilon$$

Here, $F_{\mu\nu}$ refers to the Fock operator which contains the single-electron operators and potentials in eq. (3.7) or eq. (3.9). $S_{\mu\nu}$ is the so-called overlap matrix

$$S_{\mu\nu} = \int d\mathbf{r} \chi_{\mu}^*(\mathbf{r}) \chi_{\nu}(\mathbf{r}) \quad (3.14)$$

which has to be introduced, if the basis functions are not orthonormalized.

Again, the expansion in a basis set represents an approximation to the single-electron equations, since in real calculations the basis set must consist of a finite number of basis functions while the complete basis would be infinitely large. Yet, the SCF ground state energy in the complete basis can be estimated by extrapolating the ground state energies of multiple calculations with increasing basis set size towards the so-called complete basis set limit. This also yields error estimates of the ground state energies for the individual basis sets. Naturally, the errors become smaller with increasing size of the basis set. But larger basis sets also result in longer computation times, since SCF calculations scale like $O(M^3)$ with the number of basis functions M . This can be deduced from equation (3.13). Thus, for every system an optimal basis set size has to be found which yields only small errors within acceptable computation time.

Electron spin

In the single-electron SCF equations the electron spin was always included implicitly via the index i or p of the single-electron orbitals. Explicit treatment of the electron spin results in an additional spin index σ for the orbitals ϕ_p and the

coefficients $C_{\mu p}$ in eq. (3.12)

$$\phi_p^\sigma(\mathbf{r}) = \sum_{\mu} C_{\mu p}^\sigma \chi_{\mu}(\mathbf{r}), \sigma \in \{\alpha, \beta\}. \quad (3.15)$$

Similarly, the Fock operator and the orbital energies change to $F_{\mu\nu}^\sigma$ and ϵ_p^σ , respectively. The matrix equation (3.13) then splits into two independent equations, one for α -spin electrons and one for β -spin electrons. Both equations are identical if a system with even number of electrons and zero total spin is considered. In this case solving only one of the equations is sufficient to obtain the SCF ground state determinant. This is generally referred to as restricted calculation. The resulting ground state determinant is an eigenstate of the total spin operator \hat{S}^2 . Since the Hamiltonian $\hat{\mathcal{H}}_{\text{el}}$ (3.2) does commute with \hat{S}^2 , any exact eigenstate of $\hat{\mathcal{H}}_{\text{el}}$ possesses the same property. When the equations for α - and β -spin electrons are solved separately, the calculation is called unrestricted. Then, the ground state determinant is no longer eigenstate of the total spin operator.

In the following, the electron spin will remain implicitly included in the orbital indices, if not stated otherwise.

3.1.3 Electron Correlation

As mentioned above, the HF ground state energy deviates from the exact ground state energy by the correlation energy. This rather small energy contribution (about 5% of the total energy) is relevant in most systems, since energy differences of isomers, reaction barriers, and curvatures of potential energy surfaces are of the same magnitude. Several quantum chemical methods exist which try to improve the HF ground state energy by including the electron correlation to some extent. Among them are the Møller-Plesset (MP) perturbation theory, the configuration interaction (CI) scheme and the coupled cluster (CC) scheme. All these methods and also most excited state methods rely on the fact that any SCF calculation with an arbitrary basis set yields more single-electron orbitals than necessary to construct the N -electron HF ground state determinant. The unused or virtual orbitals are employed to construct further N -electron determinants. The resulting set of N -electron states is then used to improve the HF ground state or to construct excited states. For this, the technique of second quantization is very helpful, since

it greatly simplifies the derivation and discussion of equations in many-particle systems.

Second Quantization

To introduce second quantization we start from a complete orthonormal basis of single-particle states (orbitals). With this basis an arbitrary many-particle state can be expressed in terms of occupation numbers n_s of single-particle orbitals $|\phi_s\rangle$: $|n_1 n_2 \dots n_\infty\rangle$. For electronic (fermionic) systems the occupation numbers can only assume the values 0 or 1, since each orbital can be occupied by no more than one electron. Additionally, any state $|n_1 n_2 \dots n_\infty\rangle$ must be antisymmetric with respect to permutation of two electrons.

To change occupation numbers of a many-particle state while preserving the required symmetry, the so-called annihilation and creation operators are introduced. They act on the many-particle states. The annihilation operator \hat{c}_p reduces the occupation number n_p by one, thereby removing the particle in orbital $|\phi_p\rangle$:

$$\hat{c}_p |n_1 \dots n_\infty\rangle = \begin{cases} (-1)^{n_1 + \dots + n_{p-1}} |n_1 \dots n_p - 1 \dots n_\infty\rangle, & \text{if } n_p = 1 \\ 0, & \text{otherwise} \end{cases}$$

Its hermitian adjoint operator, the creation operator \hat{c}_p^\dagger , meanwhile increases n_p by one, i.e. it adds an additional particle in orbital $|\phi_p\rangle$:

$$\hat{c}_p^\dagger |n_1 \dots n_\infty\rangle = \begin{cases} (-1)^{n_1 + \dots + n_{p-1}} |n_1 \dots n_p + 1 \dots n_\infty\rangle, & \text{if } n_p = 0 \\ 0, & \text{otherwise} \end{cases}$$

Both operators acting successively on the many-particle state yield the occupation number n_p without changing its value:

$$\hat{c}_p^\dagger \hat{c}_p |n_1 \dots n_p \dots n_\infty\rangle = n_p |n_1 \dots n_p \dots n_\infty\rangle.$$

These properties of the annihilation and creation operators give rise to the following anti-commutation relations

$$\{\hat{c}_p, \hat{c}_q\} = 0 \quad \{\hat{c}_p^\dagger, \hat{c}_q^\dagger\} = 0 \quad \{\hat{c}_p, \hat{c}_q^\dagger\} = \delta_{pq} \quad (3.16)$$

with $\{\hat{A}, \hat{B}\} = \hat{A}\hat{B} + \hat{B}\hat{A}$. Furthermore, annihilation and creation operators can be employed to derive an alternative formulation of any operator acting on a many-particle system.

Let us consider a single-particle operator $\hat{O} = \sum_{i=1}^N \hat{o}(i)$ in a N -particle system. Using the single-particle basis this operator assumes the form

$$\hat{O} = \sum_{pq} \underbrace{\langle \phi_p | \hat{o} | \phi_q \rangle}_{O_{pq}} \sum_{i=1}^N |\phi_p(\mathbf{r}_i)\rangle \langle \phi_q(\mathbf{r}_i)|. \quad (3.17)$$

When \hat{O} acts on a N -particle state, the effect of the latter part $\sum_{i=1}^N |\phi_p(\mathbf{r}_i)\rangle \langle \phi_q(\mathbf{r}_i)|$ is exactly identical to applying \hat{c}_q and \hat{c}_p^\dagger one after the other on that state. Additionally, the use of $\hat{c}_p^\dagger \hat{c}_q$ is not restricted to the N -particle system. Thus, the single-particle operator \hat{O} in any many-particle system is given by

$$\hat{O} = \sum_{pq} O_{pq} \hat{c}_p^\dagger \hat{c}_q. \quad (3.18)$$

Similarly, a two-particle operator can be written as

$$\hat{V} = \sum_{pqrs} V_{pqrs} \hat{c}_p^\dagger \hat{c}_q^\dagger \hat{c}_s \hat{c}_r. \quad (3.19)$$

Since the electronic Hamiltonian is just a sum of single- and two-particle operators it takes the following second quantized form

$$\hat{\mathcal{H}} = \sum_{pq} h_{pq} \hat{c}_p^\dagger \hat{c}_q + \frac{1}{2} \sum_{pqrs} \langle pq | rs \rangle \hat{c}_p^\dagger \hat{c}_q^\dagger \hat{c}_s \hat{c}_r \quad (3.20)$$

where the notation from eq. (3.8) was adopted.

The anti-commutation relations of the annihilation and creation operators, as well as the reformulation of operators are the parts of second quantization which simplify all subsequent derivations.

Møller-Plesset perturbation theory

The Møller-Plesset perturbation theory [39] is a special variant of the Rayleigh-Schrödinger perturbation theory [40]. The full Hamiltonian $\hat{\mathcal{H}}$ is partitioned into

a part $\hat{\mathcal{H}}_0$ for which the complete spectrum is known

$$\hat{\mathcal{H}}_0 \left| \Psi_J^{(0)} \right\rangle = E_J^{(0)} \left| \Psi_J^{(0)} \right\rangle, \quad J = 0, \dots \quad \text{and} \quad \left\langle \Psi_J^{(0)} \left| \Psi_{J'}^{(0)} \right\rangle = \delta_{JJ'} \quad (3.21)$$

and a small perturbing part $\hat{\mathcal{H}}_1$. Assuming that the ground state and the ground state energy of $\hat{\mathcal{H}}$ can be written as $E_0 = \sum_i E_0^{(i)}$ and $|\Psi_0\rangle = \sum_i |\Psi_0^{(i)}\rangle$ the Schrödinger equation for $\hat{\mathcal{H}}$ can be separated into multiple equations.

$$\hat{\mathcal{H}}_0 \left| \Psi_0^{(0)} \right\rangle = E_0^{(0)} \left| \Psi_0^{(0)} \right\rangle \quad (3.22)$$

$$\hat{\mathcal{H}}_0 \left| \Psi_0^{(1)} \right\rangle + \hat{\mathcal{H}}_1 \left| \Psi_0^{(0)} \right\rangle = E_0^{(0)} \left| \Psi_0^{(1)} \right\rangle + E_0^{(1)} \left| \Psi_0^{(0)} \right\rangle \quad (3.23)$$

$$\hat{\mathcal{H}}_0 \left| \Psi_0^{(2)} \right\rangle + \hat{\mathcal{H}}_1 \left| \Psi_0^{(1)} \right\rangle = E_0^{(0)} \left| \Psi_0^{(2)} \right\rangle + E_0^{(1)} \left| \Psi_0^{(1)} \right\rangle + E_0^{(2)} \left| \Psi_0^{(0)} \right\rangle \quad (3.24)$$

...

The projection of the first order equation (3.23) onto $\left\langle \Psi_0^{(0)} \right|$ yields the first order energy correction

$$\begin{aligned} E_0^{(0)} \left\langle \Psi_0^{(0)} \left| \Psi_0^{(1)} \right\rangle + \left\langle \Psi_0^{(0)} \left| \hat{\mathcal{H}}_1 \left| \Psi_0^{(0)} \right\rangle \right\rangle &= E_0^{(0)} \left\langle \Psi_0^{(0)} \left| \Psi_0^{(1)} \right\rangle + E_0^{(1)} \left\langle \Psi_0^{(0)} \left| \Psi_0^{(0)} \right\rangle \right. \\ \Rightarrow E_0^{(1)} &= \left\langle \Psi_0^{(0)} \left| \hat{\mathcal{H}}_1 \left| \Psi_0^{(0)} \right\rangle \right\rangle \end{aligned} \quad (3.25)$$

The first order correction to the ground state results from the projection of the same equation on $\left\langle \Psi_J^{(0)} \right|$, $J \neq 0$

$$\left| \Psi_0^{(1)} \right\rangle = \sum_{J \neq 0} \left| \Psi_J^{(0)} \right\rangle \frac{\left\langle \Psi_J^{(0)} \left| \hat{\mathcal{H}}_1 \left| \Psi_0^{(0)} \right\rangle \right\rangle}{E_0^{(0)} - E_J^{(0)}} \quad (3.26)$$

The higher order corrections can be obtained by successively applying the same procedure on the higher order equations.

In Møller-Plesset perturbation theory the molecular Hamiltonian is separated into the Hartree-Fock Hamiltonian

$$\hat{\mathcal{H}}_0 = \sum_p \epsilon_p \hat{c}_p^\dagger \hat{c}_p \quad (3.27)$$

and the perturbation

$$\hat{\mathcal{H}}_1 = - \sum_i \langle pi || qi \rangle \hat{c}_p^\dagger \hat{c}_q + \frac{1}{2} \sum_{pqrs} \langle pq || rs \rangle \hat{c}_p^\dagger \hat{c}_q^\dagger \hat{c}_s \hat{c}_r. \quad (3.28)$$

\sum_i signifies the sum over all orbitals with occupation number 1 adopting the convention that indices of occupied orbitals are denoted with i, j, \dots , while virtual orbitals are denoted with a, b, \dots , and general orbitals with p, q, \dots . This convention is followed, subsequently.

The complete set of eigenstates $|\Psi_n^{(0)}\rangle$ of $\hat{\mathcal{H}}_0$ is given by the Hartree-Fock ground state $|\Phi_0\rangle$ and all other N -electron determinants which can be constructed from $|\Phi_0\rangle$ by replacing occupied orbitals with virtual orbitals. This is most easily done by applying one or more pairs of annihilation and creation operators to $|\Phi_0\rangle$.

$$|\Psi_J^{(0)}\rangle = \hat{C}_J |\Phi_0\rangle, \text{ with } \hat{C}_J \in \left\{ \hat{c}_a^\dagger \hat{c}_i; \hat{c}_b^\dagger \hat{c}_j \hat{c}_a^\dagger \hat{c}_i, a < b, i < j; \dots \right\} \quad (3.29)$$

The resulting states are normally referred to as singly- ($|\Phi_i^a\rangle$), doubly- ($|\Phi_{ij}^{ab}\rangle$), ... excited determinants.

Plugging everything in the above equations for the energy and ground state corrections we obtain in first order

$$E_0^{(1)} = -\frac{1}{2} \sum_{ij} \langle ij || ij \rangle, \quad |\Psi_0^{(1)}\rangle = \sum_{\substack{i < j \\ a < b}} |\Phi_{ij}^{ab}\rangle \frac{\langle ab || ij \rangle}{\epsilon_i + \epsilon_j - \epsilon_a - \epsilon_b}. \quad (3.30)$$

The resulting total energy is given by $E_0^{(0)} + E_0^{(1)} = \sum_i \epsilon_i - \frac{1}{2} \sum_{ij} \langle ij || ij \rangle$. This is identical to the Hartree-Fock energy E_{HF} from eq. (3.8) which means first order MP perturbation theory does not provide any energy correction to Hartree-Fock. Thus, the second order energy correction

$$E_0^{(2)} = \sum_{\substack{i < j \\ a < b}} \frac{|\langle ab || ij \rangle|^2}{\epsilon_i + \epsilon_j - \epsilon_a - \epsilon_b}. \quad (3.31)$$

provides the first improvement to the Hartree-Fock energy.

Configuration Interaction

The configuration interaction (CI) scheme [41–43] is a method to improve the HF ground state, as well as to calculate excited states. Using the same basis of N -particle states (3.29) as MP perturbation theory, CI establishes a matrix representation \mathbf{H} of the Hamiltonian $\hat{\mathcal{H}}$ with matrix elements

$$H_{I,J} = \langle \Phi_0 | \hat{C}_I^\dagger \hat{\mathcal{H}} \hat{C}_J | \Phi_0 \rangle, \quad \text{with } \hat{C}_I \in \left\{ \hat{1}; \hat{c}_a^\dagger \hat{c}_i; \hat{c}_b^\dagger \hat{c}_j \hat{c}_a^\dagger \hat{c}_i, a < b, i < j; \dots \right\}. \quad (3.32)$$

By diagonalization of the complete Hamiltonian matrix \mathbf{H} the exact eigenvalues E_n and eigenstates $|\Psi_n\rangle$ of the Hamiltonian within the given basis are obtained

$$E_n = \sum_{IJ} X_I^{n*} H_{I,J} X_J^n, \quad |\Psi_n\rangle = \sum_I X_I^n \hat{C}_I |\Phi_0\rangle, \quad (3.33)$$

and are normally referred to as “full CI” results.

However, for most systems “full CI” calculations are not feasible with present-day computers, since the number of excited determinants scales exponentially with system size. Only small molecules like H_2 or H_2O can be calculated using “full CI”. Consequently, approximations to the CI scheme have been introduced which truncate the CI basis of N -particle determinants. The simplest approximation is the configuration interaction singles (CIS) scheme which will be described in the following section. Better approximations are provided by CID, CISD, CISDT,

The main drawback of the CI scheme is that its approximations are no longer size consistent [44]. That means that the joint calculation of two non-interacting systems yields a different result than the sum of separate calculations of the two systems.

3.2 CIS and TD-DFT

Configuration interaction singles (CIS) [23, 24] and time-dependent density functional theory (TD-DFT) [28, 29, 45, 46] are among the cheapest first-principle methods to calculate electronic excited states of molecules. Both scale with approximately $O(M^4)$ what makes them applicable to quite large systems of up to a few hundred second-row atoms. However, the accuracy of both methods is rather limited, so that thorough evaluation and testing against experimental values or benchmark results is unavoidable. In the following subsections theoretical basics, working equations and problems of both methods will be described.

3.2.1 Configuration Interaction Singles

As already mentioned before, configuration interaction singles (CIS) [23, 24] is the simplest approximation to the configuration interaction (CI) scheme. It truncates the N -particle basis (3.29) after the singly-excited determinants. Unlike “full CI” and its other approximations, CIS does not provide an improvement to the HF ground state. It only yields excited states and their energies. This is due to Brillouin’s theorem which states that the singly-excited determinants do not couple to the HF ground state [43].

$$\langle \Phi_i^a | \hat{\mathcal{H}} | \Phi_{\text{HF}} \rangle = \langle \Phi_{\text{HF}} | \hat{\mathcal{H}} | \Phi_i^a \rangle = 0 \quad (3.34)$$

From Brillouin’s theorem also follows that CIS is the only approximation to “full CI” which is still size consistent [43].

The calculation of excited states and excitation energies is performed by diagonalization of the CIS part of the Hamiltonian matrix (3.32)

$$H_{ia,jb}^{\text{CIS}} = \langle \Phi_i^a | \hat{\mathcal{H}} - E_{\text{HF}} | \Phi_j^b \rangle = (\epsilon_a - \epsilon_i) \delta_{ij} \delta_{ab} - \langle aj || bi \rangle \quad (3.35)$$

Here, the original Hamiltonian has been shifted by the HF energy to obtain excitation energies instead of absolute energies of the excited states. The corresponding eigenvalue equation reads

$$(\epsilon_a - \epsilon_i) X_{ia} - \sum_{jb} \langle aj || bi \rangle X_{jb} = \omega X_{ia}. \quad (3.36)$$

To solve this eigenvalue equation, normally, the Davidson algorithm [47] is employed. It avoids the full diagonalization of the CIS matrix by approximating the calculation of the K smallest eigenvalues. If only a few excitation energies are of interest, i.e. as long as K is much smaller than the dimension of the CIS matrix, the algorithm scales like $O(M^4)$ instead of $O(M^6)$ for full diagonalization where M is the size of the single-particle basis.

The quality of the excitation energies resulting from the diagonalization of the CIS matrix strongly depends on the system and the type of excited state in consideration. In general, CIS overestimates the excitation energies by up to 1 eV [24, 48, 49]. This is due to an unbalanced description of excitations in the dominating terms $\epsilon_a - \epsilon_i$ of the CIS matrix. These terms treat an excitation as ionization and attachment of one electron with respect to the N -electron system. However, the better description would be to treat the attachment of one electron with respect to the $N - 1$ -particle system. The additional integral term corrects for this, but not sufficiently much. Thus, CIS energies can give only a rough estimate to the true excitation energies and have to be thoroughly evaluated.

An useful extension to CIS is provided by CIS(D) [50]. CIS(D) uses perturbation theory to improve the excitation energies obtained by CIS. Thereby, it retains the size consistency of the results which is not the case in other extensions like CISD.

3.2.2 Time-Dependent Density Functional Theory

Time-dependent density functional theory is the extension of DFT to time-dependent systems. Its theoretical foundations have been published by Runge and Gross [28]. Similar to the Hohenberg-Kohn theorems for DFT, the Runge-Gross theorems prove the existence of an one-to-one mapping between time-dependent density and external potential up to a time-dependent constant. They establish an action functional of the time-dependent density $A[\rho]$ for which the exact density is a stationary point. Based on this a Kohn-Sham like system of non-interacting particles is introduced

$$i\frac{\partial}{\partial t}\phi_i(\mathbf{r}t) = \left[-\frac{1}{2}\nabla^2 + v_s(\mathbf{r}t) \right] \phi_i(\mathbf{r}t). \quad (3.37)$$

By choosing the potential to be

$$v_s(\mathbf{r}t) = v_s[\rho](\mathbf{r}t) = v_{\text{ext}}(\mathbf{r}t) + v_H[\rho](\mathbf{r}) + \frac{\delta A_{\text{xc}}[\rho](\mathbf{r}t)}{\delta \rho(\mathbf{r}t)} \quad (3.38)$$

the resulting density of the non-interacting system should be identical to the density of the interacting system if the exact exchange-correlation action functional A_{xc} is known. Since this is not the case, approximations to the xc functional as in DFT must be introduced. Additionally, it has been shown recently [51] that some proofs of the Runge-Gross theorems are erroneous. The use of the action integral is not appropriate to derive time-dependent Kohn-Sham equations, and the *ad hoc* derivation via the mapping theorem (Runge-Gross I) does not yield physical equations of motion. The current status, thus, is that TD-DFT lacks any formal justification as an exact theory. It is not at all predictive, and the evolution of the system is just reproduced once the exact time-dependent xc potential has been obtained from the time-dependent Schrödinger equation. Further work will be necessary to obtain a TD-DFT scheme with sound theoretical foundations which can yield the exact time-dependent density.

However, TD-DFT can still be employed in the linear-response regime as an *ad hoc* extension of DFT to calculate excited states. Excited states calculations are anyway the most frequent applications of TD-DFT. In these calculations, usually, the same exchange-correlation functionals as in DFT are employed.

In linear response theory, the working equations of TD-DFT become very similar to the CIS working equations (3.36). Their derivation [52] starts with the formulation of the density in terms of the time-independent KS orbitals $\phi_p(\mathbf{r})$ obtained from ground-state DFT calculations

$$\rho(\mathbf{r}t) = \sum_i \psi_i(\mathbf{r}t) \psi_i^*(\mathbf{r}t) = \sum_{pq} P_{pq}(t) \phi_p(\mathbf{r}) \phi_q^*(\mathbf{r}) \quad (3.39)$$

where $P_{pq}(t) = \sum_i c_{pi}(t) c_{qi}^*(t)$ and $c_{pi}(t) = \langle \phi_p | \psi_i(t) \rangle$. The time-dependence of the density is completely transferred to the so-called reduced density matrix $P_{pq}(t)$. $P_{pq}(t)$ obeys a differential equation which can be derived directly from the time-

dependent KS equations (3.37):

$$i \frac{\partial}{\partial t} P_{pq}(t) = \sum_r (F_{pr}[\rho] P_{rq}(t) - P_{pr}(t) F_{rq}[\rho]) \quad (3.40)$$

with

$$F_{pq}[\rho] = \left\langle \phi_p \left| -\frac{1}{2} \nabla^2 + v_{\text{ext}}(\mathbf{r}t) + v_{\text{H}}[\rho](\mathbf{r}) + v_{\text{xc}}[\rho](\mathbf{r}) \right| \phi_q \right\rangle. \quad (3.41)$$

Suppose the explicit time-dependence of F_{pq} comprises only of a small perturbation $g(\mathbf{r}t)$ in $v_{\text{ext}}(\mathbf{r}t)$. Then, F_{pq} and P_{pq} can be expanded in time series. Plugging these into (3.40) results in several differential equations. The zeroth order contributions yield an equivalent to ground-state DFT

$$\sum_r \{F_{pr}^{(0)} P_{rq}^{(0)} - P_{pr}^{(0)} F_{rq}^{(0)}\} = 0 \quad (3.42)$$

where $F_{pq}^{(0)}$ and $P_{pq}^{(0)}$ are given by $F_{pq}^{(0)} = \epsilon_p \delta_{pq}$ and $P_{pq}^{(0)} = \delta_{pq, p \in \text{occ}}$. In first order, the following linear-response equation is obtained

$$i \frac{\partial}{\partial t} P_{pq}^{(1)}(t) = \sum_r \{F_{pr}^{(0)} P_{rq}^{(1)}(t) - P_{pr}^{(1)}(t) F_{rq}^{(0)}\} \\ + \sum_r \{(F_{pr}^{(1)} + G_{pr}) P_{rq}^{(0)} - P_{pr}^{(0)} (F_{rq}^{(1)} + G_{rq})\}. \quad (3.43)$$

with $G_{pq} = \langle \psi_p | g(\mathbf{r}t) | \psi_q \rangle$ and $F_{pq}^{(1)} = \left\langle \phi_p \left| \int d\mathbf{r}_1 \int dt_1 \frac{\delta(v_{\text{H}}[\rho] + v_{\text{xc}}[\rho])}{\delta\rho(\mathbf{r}_1 t_1)} \Delta\rho(\mathbf{r}_1 t_1) \right| \phi_q \right\rangle$. The first order changes of the reduced density matrix $P_{pq}^{(1)}$ are non-zero, only if p refers to occupied and q to virtual orbitals or the other way round. This is caused by the idempotency relation $\rho^2 = \rho$ for the density and the corresponding relation $\sum_r P_{pr} P_{rq} = P_{pq}$ for the reduced density matrix. As result, equation (3.43) splits into two coupled equations, one for $P_{ai}^{(1)}$ and one for $P_{ia}^{(1)}$. The Fourier transform

of these equations with respect to time yields the TD-DFT working equations:

$$\begin{aligned} \omega X_{ia} = (\epsilon_a - \epsilon_i) X_{ia} + \sum_{jb} [\langle aj|ib\rangle + \langle aj|\delta v_{xc}|ib\rangle] X_{jb} \\ + \sum_{jb} [\langle ab|ij\rangle + \langle ab|\delta v_{xc}|ij\rangle] Y_{jb} \end{aligned} \quad (3.44)$$

and

$$\begin{aligned} -\omega Y_{ia} = (\epsilon_a - \epsilon_i) Y_{ia} + \sum_{jb} [\langle ib|aj\rangle + \langle ib|\delta v_{xc}|aj\rangle] Y_{jb} \\ + \sum_{jb} [\langle ij|ab\rangle + \langle ij|\delta v_{xc}|ab\rangle] X_{jb}. \end{aligned} \quad (3.45)$$

Here, $\Delta P_{ai}(\omega)$ and $\Delta P_{ia}(\omega)$ have been renamed as X_{ia} and Y_{ia} , respectively. The perturbation $g(\mathbf{r}t)$ has been neglected by choosing it to be infinitesimal small. $F_{pq}^{(0)}$ and $P_{pq}^{(0)}$ have been replaced by the expressions from above. The other terms originate from the Fourier transformed $F_{pq}^{(1)}$. Especially, $\langle ps|\delta v_{xc}|qr\rangle$ results from the change of the xc potential with respect to the density matrix at $P_{pq}^{(0)}$.

The equations (3.44) and (3.45) form the pseudo-eigenvalue equation

$$\begin{pmatrix} \mathbf{A} & \mathbf{B} \\ \mathbf{B}^* & \mathbf{A}^* \end{pmatrix} \begin{pmatrix} \mathbf{X} \\ \mathbf{Y} \end{pmatrix} = \omega \begin{pmatrix} \mathbf{1} & \mathbf{0} \\ \mathbf{0} & -\mathbf{1} \end{pmatrix} \begin{pmatrix} \mathbf{X} \\ \mathbf{Y} \end{pmatrix} \quad (3.46)$$

with

$$\begin{aligned} A_{ia,jb} &= (\epsilon_a - \epsilon_i) \delta_{ij} \delta_{ab} + \langle aj|ib\rangle + \langle aj|\delta v_{xc}|ib\rangle \\ B_{ia,jb} &= \langle ab|\delta v_{xc}|ij\rangle \end{aligned}$$

which has to be solved to obtain TD-DFT excited states and excitation energies. A much simpler, hermitian eigenvalue problem is obtained by neglecting the matrix \mathbf{B}

$$\mathbf{A}\mathbf{X} = \omega\mathbf{X}. \quad (3.47)$$

This is referred to as Tamm-Dancoff approximation (TDA) [25, 53].

Both, TD-DFT and TDA, can yield surprisingly good results for the excitation energies of many systems [54–57]. Deviations in excitation energies of less

than 0.3 eV can be obtained. In contrast to CIS, the dominating orbital energy differences do not yield an unbalanced treatment of the excitation. Both occupied and virtual orbital energies just suffer from approximately the same so-called self-interaction error, so that their differences are good zeroth order estimates for the excitation energies. Still, thorough evaluation of xc functionals and variants (TD-DFT or TDA) has to be performed, since it is not known *a priori* which xc functional and variant works best with a given system. Besides, there exist certain types of excited states which TD-DFT and TDA completely fail to describe. Among those are Rydberg states [58], states with large double excitation character [59–61] and charge transfer (CT) states [62–64]. The energetically high-lying Rydberg states are excited states in which one or more electrons reside in relatively large distance from the molecule. CT states represent full or partial transfer of an electron from one side of a system to another. These failures hinders the application of TD-DFT to various systems, in particular donor-acceptor or large systems.

3.2.3 Calculating Charge Transfer States

As mentioned above, TD-DFT fails to calculate CT states correctly. The excitation energies of such states are greatly underestimated. This is due to the inappropriate description of the long-range Coulomb interaction in available xc functionals for DFT. When an electron is transferred from a part A of the system in consideration to another part B, it experiences the Coulomb attraction of the now positively charged part A. This attraction is represented by matrix elements of the type $\langle ia|jb\rangle$. Such matrix elements are present in the response of the exchange term in CIS. In TD-DFT, the presence of the exchange term depends on the chosen xc functional. Hybrid xc functionals, like B3LYP, include attenuated HF exchange, while pure xc functionals lack the exchange term completely. As result, the potential energy curves of CT states along a distance coordinate R between part A and part B of the system do not display the expected $\frac{1}{R}$ -dependence when calculated with TD-DFT. They show a rather flat curve. CIS, on the other hand, yields the correct $\frac{1}{R}$ -behavior.

Several approaches have been proposed in the literature [65–69] to overcome this problem. Most of these approaches rely on modification of xc functionals to

include the long-range Coulomb interaction. However, if no such modified xc functional is available, there exist a simple work-around to the CT problem called Δ DFT [63, 70]. This is applicable, if the potential energy curve along R can in fact be calculated, e.g. if the system in consideration consists of two independent molecules. Then, the potential energy curves of the non-CT states are calculated using TD-DFT, while CIS is employed to calculate the lowest CT potential energy curve. At large distance R_0 , an additional ground-state DFT calculation is performed. By imposing constraints, this calculation is forced to converge to the charge-separated ground state. Using the resulting CT ground-state energy, the CT potential energy curve obtained with CIS is shifted to

$$\omega_{\text{CT}}(R) = \omega^{\text{CIS}}(R) - \omega^{\text{CIS}}(R_0) + E_{\text{CT}}^{\text{DFT}}(R_0) - E_0^{\text{DFT}}(R_0). \quad (3.48)$$

This yields a good estimate of the CT potential energy curve which is comparable to the other potential energy curves calculated with TD-DFT.

3.3 Algebraic Diagrammatic Construction

3.3.1 Theoretical Foundations

The algebraic diagrammatic construction (ADC) scheme [71–74] is an excited state method based on many-body Green’s function theory. Thus, it is useful to give a short introduction to Green’s function theory before explaining the ADC scheme.

Green’s Function Theory

In mathematics and physics Green’s functions are a successful technique to solve inhomogeneous differential equations. For any such differential equation the Green’s function is defined as solution of a similar differential equation with the inhomogeneity being replaced by the Dirac delta distribution $\delta(\mathbf{r} - \mathbf{r}')$. The solutions of the full differential equation are then given by

$$f(\mathbf{r}) = \int d\mathbf{r}' G(\mathbf{r} - \mathbf{r}') I(\mathbf{r}') \quad (3.49)$$

where $I(\mathbf{r}')$ is the inhomogeneity in the original differential equation.

Similarly, a Green’s function can be defined for the time-dependent single-particle Schrödinger equation

$$\left\{ i\partial_t - \hat{\mathcal{H}}(\mathbf{r}) \right\} G(\mathbf{r}t; \mathbf{r}'t') = \delta(\mathbf{r} - \mathbf{r}') \delta(t - t') \quad (3.50)$$

This is particularly useful if the Hamiltonian $\hat{\mathcal{H}}$ can be separated into one part $\hat{\mathcal{H}}_0$ for which the Schrödinger equation can be solved and a small perturbation $\hat{V}(\mathbf{r})$. Then, the solution of the Schrödinger equation with $\hat{\mathcal{H}}$ is given by

$$|\Psi(\mathbf{r}t)\rangle = |\Psi_0(\mathbf{r}t)\rangle + \int d\mathbf{r}' \int dt' G(\mathbf{r}t; \mathbf{r}'t') \hat{V}(\mathbf{r}') |\Psi_0(\mathbf{r}'t')\rangle \quad (3.51)$$

where $|\Psi_0(\mathbf{r}t)\rangle$ is the solution of the Schrödinger equation with $\hat{\mathcal{H}}_0$.

In many-body systems the definition of a Green’s function as in the single-particle case is no longer possible. However, it is possible to define similar building blocks which yield solutions to certain problems within the many-body system. These building blocks are also called Green’s functions or propagators. Most im-

portant are the one- and two-particle Green's function which are defined as

$$G_{p,q}(t_p, t_q) = -i \left\langle \Psi_0 \left| \hat{T} \left[\hat{c}_{Hp}(t_p) \hat{c}_{Hq}^\dagger(t_q) \right] \right| \Psi_0 \right\rangle \quad (3.52)$$

$$G_{p,q;r,s}(t_p, t_q; t_r, t_s) = (-i)^2 \left\langle \Psi_0 \left| \hat{T} \left[\hat{c}_{Hp}(t_p) \hat{c}_{Hq}(t_q) \hat{c}_{Hs}^\dagger(t_s) \hat{c}_{Hr}^\dagger(t_r) \right] \right| \Psi_0 \right\rangle \quad (3.53)$$

where $|\Psi_0\rangle$ refers to the exact N-particle ground state. Thus, the many-body Green's functions are ground-state expectation values of a time-ordered series of creation ($\hat{c}_{Hp}^\dagger(t)$) and annihilation ($\hat{c}_{Hp}(t)$) operators in the Heisenberg picture which, respectively, create or annihilate a particle at time t in a single-particle orbital $\phi_p(\mathbf{r})$. The operators in the Heisenberg picture are related to the time-independent annihilation and creation operators in the Schrödinger picture via the transformation

$$\begin{aligned} \hat{c}_{Hp}(t) &= e^{i\hat{H}t} \hat{c}_p e^{-i\hat{H}t} \\ \hat{c}_{Hp}^\dagger(t) &= e^{i\hat{H}t} \hat{c}_p^\dagger e^{-i\hat{H}t} \end{aligned} \quad (3.54)$$

The time-ordering of the operators is introduced by the time-ordering operator \hat{T} which is defined as

$$\hat{T} \left[\hat{A}_H(t) \hat{B}_H(t') \right] = \hat{A}_H(t) \hat{B}_H(t') \theta(t - t') - \hat{B}_H(t') \hat{A}_H(t) \theta(t' - t) \quad (3.55)$$

where the “−” is valid in fermionic systems, e.g. electrons.

The use of ground-state expectation values for the Green's functions implies loss of information about the ground state of the system compared to the ground-state wave function. However, the information content of the one-particle Green's function (eq. (3.52)) is still sufficient to calculate the ground-state expectation value of any single-particle operator, the ground-state energy, as well as the ionization and absorption spectra of the system. The two-particle Green's function (eq. (3.53)) can be employed to calculate the ground-state expectation value of two-particle operators and the excitation spectrum.

To rationalize these statements we first consider the second quantized form of an arbitrary single-particle operator in a single-particle basis from (3.18). The

expectation value of \hat{O} with respect to $|\Psi_0\rangle$ is given by

$$\langle \Psi_0 | \hat{O} | \Psi_0 \rangle = \sum_{pq} O_{pq} \langle \Psi_0 | \hat{c}_p^\dagger \hat{c}_q | \Psi_0 \rangle = -i \lim_{t' \searrow t} \sum_{pq} O_{pq} G_{q,p}(t, t') \quad (3.56)$$

where \searrow refers to t' being always larger than t . The second equality shows how the one-particle Green's function can be used to calculate expectation values of single-particle operators. Similarly, it can be shown, that the two-particle Green's function is sufficient to determine the expectation value of any two-particle operator. To express the ground state energy, i.e. the expectation value of the Hamiltonian, in terms of the one-particle Green's function is more involved. Since the Hamiltonian in general comprises particle-particle interaction potentials which are by definition two-particle operators, one would expect that also the two-particle Green's function is necessary for the calculation of the ground state energy. However, it is possible to derive an expression for the expectation value of the interaction potential in terms of the one-particle Green's function by transforming the Schrödinger equation.

At last, it shall be shown that the two-particle Green's function contains all information about the excitation spectrum of the system. Actually, this information is already present in the simpler polarization propagator

$$\begin{aligned} \Pi_{pq,rs}(t, t') &= \lim_{t_q \searrow t} \lim_{t_s \searrow t'} i \{ G_{p,s;q,r}(t, t_s; t_q, t') - G_{p,q}(t, t_q) G_{s,r}(t_s, t') \} \\ &= -i \langle \Psi_0 | \hat{T} \left[\hat{c}_{Hq}^\dagger(t) \hat{c}_{Hp}(t) \hat{c}_{Hr}^\dagger(t') \hat{c}_{Hs}(t') \right] | \Psi_0 \rangle \\ &\quad + i \langle \Psi_0 | \hat{c}_{Hq}^\dagger(t) \hat{c}_{Hp}(t) | \Psi_0 \rangle \langle \Psi_0 | \hat{c}_{Hr}^\dagger(t') \hat{c}_{Hs}(t') | \Psi_0 \rangle \end{aligned} \quad (3.57)$$

When inserting a complete set of N-particle eigenstates of the system into the equation for the polarization propagator we obtain

$$\begin{aligned} \Pi_{pq,rs}(t, t') &= -i \sum_{n \neq 0} \langle \Psi_0 | \hat{c}_{Hq}^\dagger(t) \hat{c}_{Hp}(t) | \Psi_n \rangle \langle \Psi_n | \hat{c}_{Hr}^\dagger(t') \hat{c}_{Hs}(t') | \Psi_0 \rangle \theta(t - t') \\ &\quad - i \sum_{n \neq 0} \langle \Psi_0 | \hat{c}_{Hr}^\dagger(t') \hat{c}_{Hs}(t') | \Psi_n \rangle \langle \Psi_n | \hat{c}_{Hq}^\dagger(t) \hat{c}_{Hp}(t) | \Psi_0 \rangle \theta(t' - t) \end{aligned} \quad (3.58)$$

and

$$\begin{aligned} \Pi_{pq,rs}(t, t') &= -i \sum_{n \neq 0} \left[e^{-i(E_n - E_0)(t - t')} \theta(t - t') \langle \Psi_0 | \hat{c}_q^\dagger \hat{c}_p | \Psi_n \rangle \langle \Psi_n | \hat{c}_r^\dagger \hat{c}_s | \Psi_0 \rangle \right. \\ &\quad \left. + e^{-i(E_n - E_0)(t' - t)} \theta(t' - t) \langle \Psi_0 | \hat{c}_r^\dagger \hat{c}_s | \Psi_n \rangle \langle \Psi_n | \hat{c}_q^\dagger \hat{c}_p | \Psi_0 \rangle \right] \end{aligned} \quad (3.59)$$

The latter equality is obtained by using equation (3.54) and the fact that $|\Psi_0\rangle$ and $|\Psi_n\rangle$ are eigenstates of the system. This expression for the polarization propagator shows that $\Pi_{pq,rs}(t, t')$ only depends on the time difference $\tau = t - t'$. A Fourier transform with respect to τ then yields the spectral representation of the polarization propagator

$$\begin{aligned} \Pi_{pq,rs}(\omega) &= \int d\tau e^{i\omega\tau} \Pi_{pq,rs}(\tau) \\ &= \underbrace{\sum_{n \neq 0} \frac{\langle \Psi_0 | \hat{c}_q^\dagger \hat{c}_p | \Psi_n \rangle \langle \Psi_n | \hat{c}_r^\dagger \hat{c}_s | \Psi_0 \rangle}{\omega - (E_n - E_0) + i\eta}}_{\Pi_+(\omega)} + \underbrace{\sum_{n \neq 0} \frac{\langle \Psi_0 | \hat{c}_r^\dagger \hat{c}_s | \Psi_n \rangle \langle \Psi_n | \hat{c}_q^\dagger \hat{c}_p | \Psi_0 \rangle}{-\omega - (E_n - E_0) + i\eta}}_{\Pi_-(\omega)} \end{aligned} \quad (3.60)$$

In this representation it becomes obvious that the polarization propagator consists of two parts, and both parts contain the information about the excitation spectrum of the system: the excitation energies are the poles of $\Pi_+(\omega)$ and $\Pi_-(\omega)$; the nominators can be used to obtain the transition amplitudes, since the transition moment of an arbitrary single-particle transition operator \hat{D} can be written as

$$T_n = \langle \Psi_n | \hat{D} | \Psi_0 \rangle = \sum_{pq} D_{pq} \langle \Psi_n | \hat{c}_p^\dagger \hat{c}_q | \Psi_0 \rangle \quad (3.61)$$

The statements for the one-particle Green's function about ionization and absorption spectra can be shown likewise by inserting a complete set of $(N - 1)$ - and $(N + 1)$ -particle eigenstates into the equation of the one-particle Green's function.

Perturbation Theory and Feynman Diagrams

Up to now, only the definition of the many-body Green's functions in terms of the exact N -particle ground state has been given. But how can the Green's functions be

calculated for a real system, especially if the exact ground state is unknown? One possibility is the use of perturbation theory, if the Hamiltonian is separable into one part $\hat{\mathcal{H}}_0$ for which the solutions of the Schrödinger equation are known and a small perturbation $\hat{\mathcal{H}}_1$. In this case, the definitions of the Green's functions (3.52), (3.53) and the polarization propagator (3.57) are transformed to yield the respective perturbation expansions.

First, the ground state $|\Psi_0\rangle$ to the full Hamiltonian is expressed in terms of the unperturbed ground state $|\Phi_0\rangle$ to $\hat{\mathcal{H}}_0$ by employing the so-called adiabatic “switching on” procedure in the interaction picture. The adiabatic “switching on” introduces an additional exponential factor in the Hamiltonian

$$\hat{\mathcal{H}} = \hat{\mathcal{H}}_0 + e^{-\epsilon|t|}\hat{\mathcal{H}}_1. \quad (3.62)$$

which allows an adiabatic switching between $\hat{\mathcal{H}}_0$ at $t = \pm\infty$ and $\hat{\mathcal{H}}_0 + \hat{\mathcal{H}}_1$ at $t = 0$. The modified Hamiltonian is employed in the interaction picture where the states and the operators are redefined as

$$|\Psi_I(t)\rangle = e^{i\hat{\mathcal{H}}_0 t} |\Psi(t)\rangle \quad \text{and} \quad \hat{O}(t) = e^{i\hat{\mathcal{H}}_0 t} \hat{O} e^{-i\hat{\mathcal{H}}_0 t}. \quad (3.63)$$

They now obey new differential equations

$$i\frac{\partial}{\partial t} |\Psi_I(t)\rangle = \hat{\mathcal{H}}_1(t) |\Psi_I(t)\rangle, \quad \text{with} \quad \hat{\mathcal{H}}_1(t) = e^{i\hat{\mathcal{H}}_0 t} e^{-\epsilon|t|} \hat{\mathcal{H}}_1 e^{-i\hat{\mathcal{H}}_0 t}, \quad (3.64)$$

$$\text{and} \quad i\frac{\partial}{\partial t} \hat{O}_I(t) = [\hat{O}_I(t), \hat{\mathcal{H}}_1]. \quad (3.65)$$

By solving equation (3.64) in the limits from $t = \pm\infty$ to $t = 0$, the sought-after expression for the ground state of the total system is obtained

$$|\Psi_0\rangle = \hat{U}_\epsilon(0, \pm\infty) |\Phi_0\rangle \quad (3.66)$$

with

$$\hat{U}_\epsilon(t, t_0) = \sum_{n=0}^{\infty} (-i)^n \frac{1}{n!} \int_{t_0}^t dt_1 \cdots \int_{t_0}^{t_1} dt_n e^{-\epsilon(|t_1| + \cdots + |t_n|)} \cdot \hat{T}[\hat{\mathcal{H}}_1(t_1) \cdots \hat{\mathcal{H}}_1(t_n)] \quad (3.67)$$

where the limit $\epsilon \rightarrow 0$ has to be taken in the end.

In a second step, the Heisenberg annihilation and creation operators are written in terms of the respective operators in the interaction picture. Solving equation (3.65) yields these expressions:

$$\hat{O}_H(t) = U_\epsilon(0, t) \hat{O}_I(t) U_\epsilon(t, 0), \quad \text{with} \quad \hat{O} \in \{\hat{c}, \hat{c}^\dagger, \dots\} \quad (3.68)$$

Now, equations (3.66) and (3.68) are used to derive the perturbation expansions. For the single-particle Green's function and the polarization propagator they are given by

$$G_{p,q}(t, t') = -i \sum_{n=0}^{\infty} (-i)^n \frac{1}{n!} \int_{-\infty}^{\infty} dt_1 \cdots \int_{-\infty}^{\infty} dt_n e^{-\epsilon(|t_1| + \dots + |t_n|)} \cdot \left\langle \Phi_0 \left| \hat{T} \left[\hat{\mathcal{H}}_1(t_1) \cdots \hat{\mathcal{H}}_1(t_n) \hat{c}_{I_p}(t) \hat{c}_{I_q}^\dagger(t') \right] \right| \Phi_0 \right\rangle \quad (3.69)$$

and

$$\begin{aligned} \Pi_{pq,rs}(t, t') &= (-i) \sum_{n=0}^{\infty} (-i)^n \frac{1}{n!} \int_{-\infty}^{\infty} dt_1 \cdots \int_{-\infty}^{\infty} dt_n e^{-\epsilon(|t_1| + \dots + |t_n|)} \\ &\quad \left\langle \Phi_0 \left| \hat{T} \left[\hat{\mathcal{H}}_1(t_1) \cdots \hat{\mathcal{H}}_1(t_n) \hat{c}_{I_q}^\dagger(t) \hat{c}_{I_p}(t) \hat{c}_{I_r}^\dagger(t') \hat{c}_{I_s}(t') \right] \right| \Phi_0 \right\rangle \\ &\quad + G_{p,q}(t, t) G_{s,r}(t', t'). \end{aligned} \quad (3.70)$$

Zeroth, first, second, ... order approximations to these expressions are obtained by truncating the sum over n at $n = 0, 1, 2, \dots$, respectively. Hence, the n -th summand represents the n -th order correction in the perturbation expansion. It consists of n time integrals over a matrix element of time-ordered operators in the interaction picture. The operators are all annihilation and creation operators, since the second quantized form of $\hat{\mathcal{H}}_1(t)$ is essentially a sum over products of annihilation and creation operators. Thus, evaluation of the matrix element is best done in a single-particle basis in which the representation of $\hat{\mathcal{H}}_0$ is diagonal, like in the HF basis if the HF Hamiltonian $\hat{\mathcal{H}}_0 = \sum_p \epsilon_p \hat{c}_p^\dagger \hat{c}_p$ is used. In this basis the time-dependence of the annihilation and creation operators is most simple:

$$\hat{c}_{I_p}(t) = e^{-i\epsilon_p t} \hat{c}_p \quad \text{and} \quad \hat{c}_{I_p}^\dagger(t) = e^{i\epsilon_p t} \hat{c}_p^\dagger. \quad (3.71)$$

The computation of zeroth order approximations then results in

$$\begin{aligned} G_{p,q}^0(t,t') &= -i \left\langle \Phi_0 \left| \hat{T} \left[\hat{c}_{I_p}(t) \hat{c}_{I_q}^\dagger(t') \right] \right| \Phi_0 \right\rangle \\ &= -i \delta_{pq} e^{-i\epsilon_p(t-t')} [\delta_{p \in \text{virt}} \theta(t-t') - \delta_{p \in \text{occ}} \theta(t'-t)] \end{aligned} \quad (3.72)$$

for the single-particle Green's function and

$$\begin{aligned} \Pi_{pq,rs}^0(t,t') &= -i \delta_{pr} \delta_{qs} e^{i(\epsilon_q - \epsilon_p)(t-t')} \\ &\quad \cdot [\delta_{p \in \text{virt}} \delta_{q \in \text{occ}} \theta(t-t') + \delta_{p \in \text{occ}} \delta_{q \in \text{virt}} \theta(t'-t)] \\ &= i G_{p,r}^0(t,t') G_{q,s}^0(t',t) \end{aligned} \quad (3.73)$$

for the polarization propagator. The calculation of higher order terms becomes increasingly complicated, since each $\hat{\mathcal{H}}_1(t)$ adds more annihilation and creation operators to the respective matrix element.

A systematic way to evaluate those matrix elements is provided by the so-called Feynman diagrams. A set of construction rules enables to build graphical representations of all non-vanishing contributions to the matrix elements. From those graphs the corresponding equations can be derived in a straightforward way. Each graph or Feynman diagram is constructed of a fixed number of vertical solid lines and horizontal wavy lines or squares (see Fig. 3.1) which represent zeroth-order single-particle Green's functions (3.72) and interaction terms stemming from $\hat{\mathcal{H}}_1$, respectively. The n -th order Feynman diagrams consist of n interactions and

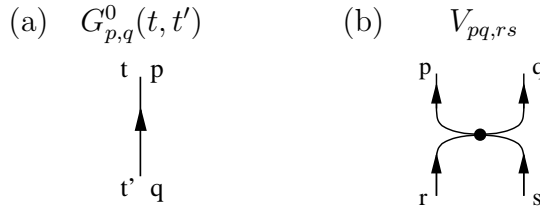


Figure 3.1: Building blocks of Feynman diagrams: (a) zeroth order single-particle Green's function, (b) particle-particle interaction line.

$2n+1$ solid lines in case of the single-particle Green's function or $2n+2$ solid lines in case of the polarization propagator. For example, the only zeroth order Feynman diagram for the polarization propagator consists of two solid lines (Fig. 3.2), as the

second part of equation (3.73) suggested. The complete set of Feynman diagrams for the polarization propagator up to second order is displayed in Figure 3.2.

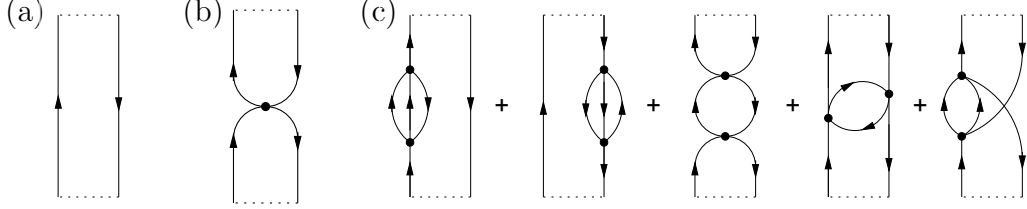


Figure 3.2: Zeroth (a), first (b) and second (c) order Feynman diagrams of the polarization propagator

Evaluation of the Feynman diagrams yields expressions for Green's functions in the time domain. To obtain similar expressions in the frequency domain, the Feynman diagrams can be transformed into Goldstone diagrams. Each Feynman diagram results in one or more Goldstone diagrams which then can be evaluated. A more detailed explanation of Goldstone and Feynman diagrams can be found in the literature [25, 75].

Derivation of the ADC Equations

The ADC scheme is based on the perturbation expansion of the transition function in terms of Feynman and Goldstone diagrams [71]. The transition function is defined as

$$T(\omega) = \mathbf{D}^\dagger \mathbf{\Pi}_+(\omega) \mathbf{D} \quad (3.74)$$

with \mathbf{D} being the matrix representation of an arbitrary transition operator (e.g. the dipole operator). For the perturbation expansion the Hamiltonian is partitioned in the same way as in Møller-Plesset perturbation theory (see (3.27) and (3.28)). The resulting perturbation series is given by

$$T(\omega) = \sum_{n=0}^{\infty} T^{(n)}(\omega) = \sum_{n=0}^{\infty} \mathbf{D}^\dagger \mathbf{\Pi}_+^{(n)}(\omega) \mathbf{D}, \quad (3.75)$$

where the equations for $\mathbf{\Pi}_+^{(n)}(\omega)$ can be determined from the Goldstone diagrams in n -th order.

Now, it is assumed that an expression similar to (3.74) exists which describes the transition function in terms of new vector and matrix objects

$$T(\omega) = \mathbf{F}^\dagger \mathbf{\Gamma}(\omega) \mathbf{F}, \quad \text{with } \mathbf{\Gamma}(\omega) = [\omega \mathbf{1} - (\mathbf{K} + \mathbf{C})]^{-1}. \quad (3.76)$$

where the so-called modified transition moments \mathbf{F} , and the matrices $\mathbf{\Gamma}(\omega)$, \mathbf{K} and \mathbf{C} are expressed in terms of singly, doubly, ... excited configurations. It is obvious that solving the eigenvalue problem

$$(\mathbf{K} + \mathbf{C}) \mathbf{X} = \mathbf{X} \Omega \quad (3.77)$$

yields the poles of $\mathbf{\Gamma}(\omega)$ and also the poles of the transition function. From eq. (3.74) we know that the poles of the transition function are as well the poles of $\mathbf{\Pi}_+^{(n)}(\omega)$ which in turn represent the excitation energies of the system in consideration. As result, the excitation energies of the system are given by the eigenvalues of $\mathbf{K} + \mathbf{C}$. The corresponding eigenvectors can be used to calculate the transition amplitudes by multiplication with the modified transition moments $\mathbf{F}^\dagger \mathbf{X}$.

But, how does \mathbf{K} , \mathbf{C} and \mathbf{F} look like? To relate them to the perturbation expansions of the transition function (3.75), \mathbf{F} and $\mathbf{K} + \mathbf{C}$ are written in perturbation series

$$\mathbf{F} = \sum_{n=0}^{\infty} \mathbf{F}^{(n)} \quad \text{and} \quad \mathbf{K} + \mathbf{C} = \mathbf{K} + \sum_{n=1}^{\infty} \mathbf{C}^{(n)} \quad (3.78)$$

Plugging these expressions into eq. (3.76), another perturbation expansion of the transition function is obtained. Its zeroth, first and second order terms are given by

$$T^{(0)}(\omega) = \mathbf{F}^{(0)\dagger} [\omega \mathbf{1} - \mathbf{K}]^{-1} \mathbf{F}^{(0)} \quad (3.79)$$

$$\begin{aligned} T^{(1)}(\omega) = & \mathbf{F}^{(0)\dagger} [\omega \mathbf{1} - \mathbf{K}]^{-1} \mathbf{C}^{(1)} [\omega \mathbf{1} - \mathbf{K}]^{-1} \mathbf{F}^{(0)} \\ & + \mathbf{F}^{(1)\dagger} [\omega \mathbf{1} - \mathbf{K}]^{-1} \mathbf{F}^{(0)} + \mathbf{F}^{(0)\dagger} [\omega \mathbf{1} - \mathbf{K}]^{-1} \mathbf{F}^{(1)} \end{aligned} \quad (3.80)$$

$$\begin{aligned}
T^{(2)}(\omega) = & \mathbf{F}^{(1)\dagger} [\omega \mathbf{1} - \mathbf{K}]^{-1} \mathbf{F}^{(1)} + \mathbf{F}^{(0)\dagger} [\omega \mathbf{1} - \mathbf{K}]^{-1} \mathbf{C}^{(2)} [\omega \mathbf{1} - \mathbf{K}]^{-1} \mathbf{F}^{(0)} \\
& + \mathbf{F}^{(0)\dagger} [\omega \mathbf{1} - \mathbf{K}]^{-1} \mathbf{C}^{(1)} [\omega \mathbf{1} - \mathbf{K}]^{-1} \mathbf{C}^{(1)} [\omega \mathbf{1} - \mathbf{K}]^{-1} \mathbf{F}^{(0)} \\
& + \mathbf{F}^{(1)\dagger} [\omega \mathbf{1} - \mathbf{K}]^{-1} \mathbf{C}^{(1)} [\omega \mathbf{1} - \mathbf{K}]^{-1} \mathbf{F}^{(0)} \\
& + \mathbf{F}^{(0)\dagger} [\omega \mathbf{1} - \mathbf{K}]^{-1} \mathbf{C}^{(1)} [\omega \mathbf{1} - \mathbf{K}]^{-1} \mathbf{F}^{(1)}
\end{aligned} \tag{3.81}$$

Comparison of the terms with the diagrammatic perturbation expansion (3.75) results in expressions for $\mathbf{F}^{(n)}$, $\mathbf{C}^{(n)}$, and \mathbf{K} .

In zeroth and first order the obtained matrices are restricted to the space of singly excited configurations:

$$\text{zeroth order: } K_{ia,jb} = (\epsilon_a - \epsilon_i) \delta_{ab} \delta_{ij} \quad F_{ia}^{(0)} = D_{ia} \tag{3.82}$$

$$\text{first order: } C_{ia,jb}^{(1)} = -\langle aj || bi \rangle \quad F_{ia}^{(1)} = \sum_{bj} \frac{\langle ab || ji \rangle}{\epsilon_a - \epsilon_j + \epsilon_b - \epsilon_i} D_{jb} \tag{3.83}$$

Starting from second order also the space of doubly excited configurations has to be taken into account. The respective expressions for \mathbf{C} are obtained as

$$C_{ia,jb}^{(2)} = C_{ia,jb}^{(2)A} + C_{ia,jb}^{(2)B} + C_{ia,jb}^{(2)C} \tag{3.84}$$

$$C_{ia,kcld}^{(1)} = \langle kl || id \rangle \delta_{ac} - \langle kl || ic \rangle \delta_{ad} - \langle al || cd \rangle \delta_{ik} + \langle ak || cd \rangle \delta_{il} \tag{3.85}$$

$$C_{iajb,kc}^{(1)} = \langle kb || ij \rangle \delta_{ac} - \langle ka || ij \rangle \delta_{bc} - \langle ab || cj \rangle \delta_{ik} + \langle ab || ci \rangle \delta_{jk} \tag{3.86}$$

$$K_{iajb,kcld} = (\epsilon_a - \epsilon_i + \epsilon_b - \epsilon_j) \delta_{ac} \delta_{bd} \delta_{ik} \delta_{jl} \tag{3.87}$$

with

$$\begin{aligned}
C_{ia,jb}^{(2)A} &= \frac{1}{4} \delta_{ij} \sum_{ckl} \left[\frac{\langle ac || kl \rangle \langle kl || bc \rangle}{\epsilon_a - \epsilon_k + \epsilon_c - \epsilon_l} + \frac{\langle ac || kl \rangle \langle kl || bc \rangle}{\epsilon_b - \epsilon_k + \epsilon_c - \epsilon_l} \right] \\
C_{ia,jb}^{(2)B} &= \frac{1}{4} \delta_{ab} \sum_{cdk} \left[\frac{\langle cd || ik \rangle \langle jk || cd \rangle}{\epsilon_c - \epsilon_i + \epsilon_d - \epsilon_k} + \frac{\langle cd || ik \rangle \langle jk || cd \rangle}{\epsilon_c - \epsilon_j + \epsilon_d - \epsilon_k} \right] \\
C_{ia,jb}^{(2)C} &= -\frac{1}{2} \sum_{ck} \left[\frac{\langle ac || ik \rangle \langle jk || bc \rangle}{\epsilon_a - \epsilon_i + \epsilon_c - \epsilon_k} + \frac{\langle ac || ik \rangle \langle jk || bc \rangle}{\epsilon_b - \epsilon_j + \epsilon_c - \epsilon_k} \right].
\end{aligned}$$

The corresponding modified transition moments consist of thirteen terms in the

space of singly excited configurations

$$F_{ia}^{(2)} = F_{ia}^{(2)A} + F_{ia}^{(2)B} + F_{ia}^{(2)C} + \sum_{I=1}^{10} F_{ia}^{(2,I)} \quad (3.88)$$

(the individual terms can be found in Appendix A.1) and one term in the space of doubly excited configurations

$$\begin{aligned} F_{iajb}^{(2)} = & \sum_k \frac{\langle ab || ki \rangle}{\epsilon_a - \epsilon_k + \epsilon_b - \epsilon_i} D_{kj} - \sum_k \frac{\langle ab || kj \rangle}{\epsilon_a - \epsilon_k + \epsilon_b - \epsilon_j} D_{ki} \\ & + \sum_c \frac{\langle cb || ij \rangle}{\epsilon_c - \epsilon_i + \epsilon_b - \epsilon_j} D_{ac} - \sum_c \frac{\langle ca || ij \rangle}{\epsilon_c - \epsilon_i + \epsilon_a - \epsilon_j} D_{bc}. \end{aligned} \quad (3.89)$$

As can be seen, the part of $\mathbf{K} + \mathbf{C}$ referring to doubly excited configurations consists only of the diagonal of orbital energy differences. This results in a rather limited treatment of doubly excited configurations with second order ADC. However, by including the following term originating from third order ADC

$$\begin{aligned} C_{abij,cdkl}^{(1)} = & \langle ab || cd \rangle \delta_{ik} \delta_{jl} + \langle kl || ij \rangle \delta_{ac} \delta_{bd} \\ & - \left[\langle ak || ci \rangle \delta_{bd} \delta_{jl} + \langle al || cj \rangle \delta_{bd} \delta_{ik} + \langle bk || di \rangle \delta_{ac} \delta_{jl} + \langle bl || dj \rangle \delta_{ac} \delta_{ik} \right] \\ & + \left[\langle al || ci \rangle \delta_{bd} \delta_{jk} + \langle ak || cj \rangle \delta_{bd} \delta_{il} + \langle bl || di \rangle \delta_{ac} \delta_{jk} + \langle bk || dj \rangle \delta_{ac} \delta_{il} \right] \\ & + \left[\langle ak || di \rangle \delta_{bc} \delta_{jl} + \langle al || dj \rangle \delta_{bc} \delta_{ik} + \langle bk || ci \rangle \delta_{ad} \delta_{jl} + \langle bl || cj \rangle \delta_{ad} \delta_{ik} \right] \\ & - \left[\langle al || di \rangle \delta_{bc} \delta_{jk} + \langle ak || dj \rangle \delta_{bc} \delta_{il} + \langle bl || ci \rangle \delta_{ad} \delta_{jk} + \langle bk || cj \rangle \delta_{ad} \delta_{il} \right] \end{aligned} \quad (3.90)$$

the treatment of doubly excited configurations can be improved yielding an extended second order ADC scheme called ADC(2)-x.

The Intermediate State Representation

An alternative derivation for the ADC equations is provided via the so-called intermediate state representation (ISR) [76]. The starting point of the derivation is the construction of a many-particle basis for excited states based on the exact ground state $|\Psi_0\rangle$. Therefore, a set of excitation operators \hat{C}_I is applied to the ground state. The excitation operators consist of pairs of annihilation and creation

operators as in (3.29)

$$\hat{C}_I \in \left\{ \hat{c}_a^\dagger \hat{c}_i; \hat{c}_b^\dagger \hat{c}_j \hat{c}_a^\dagger \hat{c}_i, a < b, i < j; \dots \right\}. \quad (3.91)$$

The resulting states $|\Psi_I^\#\rangle = \hat{C}_I |\Psi_0\rangle$ can naturally be grouped into classes of single, double, ... excitations. In contrast to the singly, doubly, ... excited determinants obtained by applying the same set of excitation operators onto the HF ground state, these states are not necessarily orthogonal to each other. Thus, orthogonalization of the $|\Psi_I^\#\rangle$ is performed using a step-wise Gram-Schmidt orthogonalization procedure. First, the states of the single excitation class are orthogonalized with respect to the ground state and to each other. Then, the states of each successive excitation class are orthogonalized with respect to the ground state, to each other, and to all states of lower excitation classes. In this way, the orthonormal basis of intermediate states $|\tilde{\Psi}_I\rangle$ is obtained.

The intermediate states are employed to construct a matrix representation of the shifted Hamiltonian $\hat{\mathcal{H}} - E_0$ similar to what is done in the CI scheme (3.32):

$$M_{I,J} = \langle \tilde{\Psi}_I | \hat{\mathcal{H}} - E_0 | \tilde{\Psi}_J \rangle. \quad (3.92)$$

Diagonalization of the matrix \mathbf{M} , in principle, yields the exact excited states and their energies within the given single-particle basis. However, neither the exact ground state nor the exact ground state energy are in general known. Instead approximations to ground state and ground state energy are employed in eq. (3.92). Using n -th order MP theory for these approximations results in the same n -th order ADC equations which have been derived via the Green's function theory above.

From the eigenvectors \mathbf{X}_n of \mathbf{M} the excited states can formally be constructed via

$$|\Psi_n\rangle = \sum_I X_{I,n} |\tilde{\Psi}_I\rangle. \quad (3.93)$$

This expression is used to derive equations for the calculation of transition moments and excited state properties. The definitions of transition moments and excited state properties with respect to some arbitrary operator \hat{D} are normally

given by

$$T_n = \langle \Psi_n | \hat{D} | \Psi_0 \rangle, \quad T_{mn} = \langle \Psi_m | \hat{D} | \Psi_n \rangle, \quad \text{and} \quad \langle D \rangle_n = \langle \Psi_n | \hat{D} | \Psi_n \rangle. \quad (3.94)$$

By insertion of $\sum_I |\tilde{\Psi}_I\rangle \langle \tilde{\Psi}_I|$ into the definition for T_n before \hat{D} , an expression for T_n in terms of the eigenvectors \mathbf{X}_n is obtained

$$T_n = \sum_I \langle \Psi_n | \tilde{\Psi}_I \rangle \langle \tilde{\Psi}_I | \hat{D} | \Psi_0 \rangle = \sum_I X_{I,n}^* F_I. \quad (3.95)$$

$F_I = \langle \tilde{\Psi}_I | \hat{D} | \Psi_0 \rangle$ is identified as the modified transition moments introduced in the previous derivation of the ADC scheme. Similarly, $\sum_I |\tilde{\Psi}_I\rangle \langle \tilde{\Psi}_I|$ is inserted in the definitions of T_{mn} and $\langle D \rangle_n$, thereby introducing the so-called ISR matrix \mathbf{D}

$$D_{I,J} = \langle \tilde{\Psi}_I | \hat{D} | \tilde{\Psi}_J \rangle. \quad (3.96)$$

The resulting equations

$$T_{mn} = \sum_{I,J} X_{I,m}^* D_{I,J} X_{J,n}, \quad \text{and} \quad \langle D \rangle_n = \sum_{I,J} X_{I,n}^* D_{I,J} X_{J,n}, \quad (3.97)$$

allow the calculation of T_{mn} and $\langle D \rangle_n$ from the eigenvectors of the ADC matrix.

3.3.2 Implementation of ADC(2)

For the implementation of the ADC(2)-s and ADC(2)-x schemes we have chosen the development version of the Q-Chem package of programs [77]. Based on the equations which are given in this and the following sections, the ADC program is implemented as set of C++ classes in an already existing C++ programming environment which is part of Q-Chem. An extensive manual is provided along with the code in terms of Doxygen [78] based documentation.

The ADC(2)-s and ADC(2)-x working equations, as they have been published in [71, 74], indicate how to build the ADC matrix for second order of perturbation theory. Yet, building the complete ADC matrix and diagonalizing it afterwards is not advisable, since the size of the ADC matrix scales like $O(M^8)$. The use of the Davidson algorithm [47] provides a way to avoid this problem. As long as

only a few of the smallest eigenvalues have to be calculated, it reduces the scaling significantly. It only requires the calculation of products of the ADC matrix with arbitrary vectors which means the ADC matrix does not need to be stored on disk any longer. It is sufficient to store the data elements of which the ADC matrix is constructed. They only scale like $O(M^4)$. The computation time of the matrix-vector product scales like $O(M^5)$ and $O(M^6)$ for ADC(2)-s and ADC(2)-x, respectively.

As result, implementing the ADC scheme based on the Davidson algorithm means first to rewrite the original ADC equations as matrix-vector products

$$\begin{aligned} r_{ia} &= \sum_{jb} M_{ia,jb} v_{jb} + \sum_{k<c,l<d} M_{ia,kcld} v_{kcld} \\ r_{iajb} &= \sum_{kc} M_{iajb,kc} v_{kc} + \sum_{k<c,l<d} M_{iajb,kcld} v_{kcld}. \end{aligned}$$

Here, no gain in computation time is visible yet. But, when plugging in the expressions for the ADC matrix (3.82)-(3.90) the multitude of Kronecker deltas causes many sums to vanish. The zeroth and first order equations become similar to the CIS working equations (3.36).

$$r_{ia} = (\epsilon_a - \epsilon_i) v_{ia} - \sum_{jb} \langle aj | bi \rangle v_{jb}$$

In second order, special care has to be taken with the block of singly excited configurations. The straightforward treatment of the respective terms would result in computation times of $O(M^6)$. However, utilization of intermediate vectors can reduce the computational scaling by one order. Two intermediate vectors \tilde{v}_{ab} and \tilde{v}_{ij} can be defined for $C^{(2)A}$ and $C^{(2)B}$:

$$\begin{aligned} \tilde{v}_{ab} &= \frac{1}{4} \sum_{ckl} \left[\frac{\langle ac | kl \rangle \langle kl | bc \rangle}{\epsilon_a - \epsilon_k + \epsilon_c - \epsilon_l} + \frac{\langle ac | kl \rangle \langle kl | bc \rangle}{\epsilon_b - \epsilon_k + \epsilon_c - \epsilon_l} \right] \\ \tilde{v}_{ij} &= \frac{1}{4} \sum_{cdk} \left[\frac{\langle cd | ik \rangle \langle jk | cd \rangle}{\epsilon_c - \epsilon_i + \epsilon_d - \epsilon_k} + \frac{\langle cd | ik \rangle \langle jk | cd \rangle}{\epsilon_c - \epsilon_j + \epsilon_d - \epsilon_k} \right]. \end{aligned} \quad (3.98)$$

They need to be computed just once and can be stored for the remainder of the calculation. Part $C^{(2)C}$ of the ADC matrix necessitates the introduction of two

additional intermediates

$$\tilde{v}_{ia}^{(1)} = \sum_{jb} \langle ji | |ba\rangle v_{jb} \quad \text{and} \quad \tilde{v}_{ia}^{(2)} = \sum_{jb} \frac{\langle ji | |ba\rangle}{\epsilon_b - \epsilon_j + \epsilon_a - \epsilon_i} v_{jb} \quad (3.99)$$

which have to be recomputed for every new vector v_{ia} . Altogether, the product of the block of singly excited configurations with the vector v_{ia} using intermediates is given by

$$r_{ia} = \sum_b \tilde{v}_{ab} v_{ib} + \sum_j \tilde{v}_{ij} v_{ja} - \frac{1}{2} \sum_{jb} \left[\frac{\langle ab | |ij\rangle}{\epsilon_a - \epsilon_i + \epsilon_b - \epsilon_j} \tilde{v}_{jb}^{(1)} + \langle ab | |ij\rangle \tilde{v}_{jb}^{(2)} \right]. \quad (3.100)$$

The remaining terms of the matrix-vector product in second order are again straightforward to derive (see Appendix A.2). The same is true for the terms of the second order extension. No special treatment is possible in this case, so that the scaling of these terms becomes $O(M^6)$.

Up to now, spin was always included implicitly in the indices of the equations. However, for the implementation of ADC it is more favorable to treat spin separately. This is especially true in case of restricted calculations, as will become obvious later. Extracting spin from the indices of a vector v_{ia} of singly excited configurations yields four distinct blocks. Only two of them need to be considered, if spin-flip excitations, i.e. excitations with spin-quantum number $\Delta m_z \neq 0$, are excluded from the calculations. The relevant blocks are referred to as v_{ia} and $v_{i\bar{a}}$ where the bar on the indices indicates that they are associated with β -spin. In the same way, vectors of doubly excited configurations divide into three relevant parts: two pure-spin parts v_{iajb} and $v_{i\bar{a}\bar{j}\bar{b}}$, and one opposite-spin part $v_{i\bar{a}j\bar{b}}$. The opposite-spin part is no longer subject to the restrictions of the indices $a < b$ and $i < j$, since they are always fulfilled (α -spin indices being always smaller than β -spin indices). Lift the restrictions for the two pure-spin parts, as well, is advantageous for numerical reasons. Then, the pure-spin blocks acquire the following permutational anti-symmetry

$$v_{iajb} = -v_{ibja} = -v_{jaib} = v_{jbia}.$$

Additionally, some of the ADC expressions need to be modified. Among those is the scalar product of two vectors. There, scaling factors of $\frac{1}{4}$ have to be introduced

in front of products of the pure-spin blocks:

$$\begin{aligned}
v \cdot w = & \sum_{ia} v_{ia} w_{ia} + \sum_{ia} v_{\bar{ia}} w_{\bar{ia}} \\
& + \frac{1}{4} \sum_{iajb} v_{iajb} w_{iajb} + \sum_{ia\bar{j}\bar{b}} v_{ia\bar{j}\bar{b}} w_{ia\bar{j}\bar{b}} + \frac{1}{4} \sum_{\bar{ia}\bar{j}\bar{b}} v_{\bar{ia}\bar{j}\bar{b}} w_{\bar{ia}\bar{j}\bar{b}}. \quad (3.101)
\end{aligned}$$

The expressions involving couplings of singly and doubly excited configurations have to be changed into

$$\begin{aligned}
r_{ia}^\alpha = & \dots + \sum_{kcl} v_{kalc} \langle ic|kl \rangle + \sum_{kcl} v_{kal\bar{c}} \langle i\bar{c}|k\bar{l} \rangle \\
& - \sum_{ckd} \langle ak|cd \rangle v_{ickd} - \sum_{\bar{c}\bar{k}\bar{d}} \langle a\bar{k}|\bar{c}\bar{d} \rangle v_{i\bar{c}\bar{k}\bar{d}}, \quad (3.102)
\end{aligned}$$

while the terms which are only present in ADC(2)-x are adjusted to

$$\begin{aligned}
r_{iajb} = & \dots + \sum_{cd} \langle ab|cd \rangle v_{icjd} + \sum_{kl} \langle ij|kl \rangle v_{kalb} \\
& - \sum_{kc} [\langle ak||ci \rangle v_{jbkc} - \langle ak||cj \rangle v_{ibkc} - \langle bk||ci \rangle v_{jake} + \langle bk||cj \rangle v_{iake}] \\
& + \sum_{\bar{k}\bar{c}} [\langle a\bar{k}|\bar{i}\bar{c} \rangle v_{j\bar{b}\bar{k}\bar{c}} - \langle a\bar{k}|\bar{j}\bar{c} \rangle v_{i\bar{b}\bar{k}\bar{c}} - \langle \bar{b}\bar{k}|\bar{i}\bar{c} \rangle v_{j\bar{a}\bar{k}\bar{c}} + \langle \bar{b}\bar{k}|\bar{j}\bar{c} \rangle v_{i\bar{a}\bar{k}\bar{c}}]. \quad (3.103)
\end{aligned}$$

The full set of transformed equations can be found in Appendix A.3, though in slightly different notation.

The above transformation allows for an optimized treatment of restricted calculations. In such calculations the orbitals obtained by Hartree-Fock are by definition identical for α -spin and β -spin electrons. As result, the orbital energies, as well as the two-electron integrals are the same no matter whether the respective indices are associated with α - or β -spin. The two spin-blocks of singly excited configurations then also become identical, though only up to a sign: $v_{ia} = \pm v_{\bar{j}\bar{b}}$. It is straightforward to show that the positive sign is connected with singlet states while the negative sign indicates triplet states. In a similar way, one can deduce that the pure-spin blocks of the doubly excited configurations differ by no more than their sign. Here, positive sign means either singlet or quintet state, while

the negative sign is associated with a triplet state. The opposite-spin part has no direct relation to the pure-spin parts. However, it is possible to introduce new vectors $V_{iajb}^{S/T/Q}$ for each state type from which the respective pure- and opposite-spin parts can be constructed.

- Singlet states:

$$\begin{aligned} v_{ia} (= v_{\bar{ia}}) &:= V_{ia}^S, \\ v_{iajb} (= v_{\bar{iajb}}) &:= V_{iajb}^S - V_{ibja}^S, & v_{ia\bar{jb}} &:= V_{iajb}^S \end{aligned} \quad (3.104)$$

- Triplet states:

$$\begin{aligned} v_{ia} (= -v_{\bar{ia}}) &:= V_{ia}^T, \\ v_{iajb} (= -v_{\bar{iajb}}) &:= V_{iajb}^T - V_{ibja}^T - V_{jaib}^T + V_{jbia}^T, \\ v_{ia\bar{jb}} &:= V_{iajb}^T - V_{jbia}^T \end{aligned} \quad (3.105)$$

- Quintet states:

$$v_{iajb} (= -v_{\bar{iajb}}) := V_{iajb}^Q, \quad v_{ia\bar{jb}} := -V_{iajb}^Q \quad (3.106)$$

The ADC equations can be reformulated completely in terms of these new vectors V_{ia}^S , V_{iajb}^S , V_{ia}^T , V_{iajb}^T , and V_{iajb}^Q . The modified equations can be found in Appendix A.4. The adoption of the new vectors also necessitates modifications of the scalar product of two excited state vectors:

- Singlet states:

$$\mathbf{v} \cdot \mathbf{w} = 2 \sum_{ia} V_{ia}^S W_{ia}^S + \sum_{iajb} V_{iajb}^S (2W_{iajb}^S - W_{ibja}^S) \quad (3.107)$$

- Triplet states:

$$\mathbf{v} \cdot \mathbf{w} = 2 \sum_{iajb} V_{iajb}^T W_{iajb}^T + 2 \sum_{iajb} V_{iajb}^T (2W_{iajb}^T - W_{ibja}^T - W_{jaib}^T) \quad (3.108)$$

- Quintet states:

$$\mathbf{v} \cdot \mathbf{w} = \frac{3}{2} \sum_{iajb} V_{iajb}^Q W_{iajb}^Q \quad (3.109)$$

Now, only one singly excited and one doubly excited configuration vector is necessary to calculate excited states of certain type.

In our implementation of the ADC scheme, we also employ the so-called Resolution-of-the-Identity (RI) approximation [79, 80] to calculate the two-electron integrals in the basis of the HF orbitals. This reduces the computational effort to form the integrals. However, if the major concern in an ADC calculation is not the computation time, but the memory and disk space requirements, the RI approximation can also be used to reduce the amount of data during a calculation. In this case, the intermediate entities B_{pq}^P which are normally employed to form the two-electron integrals via

$$\langle pq|rs\rangle = (pr|qs) = \sum_P B_{pr}^P B_{qs}^P, \quad \text{with } B_{pq}^P = \sum_Q (pq|Q) (Q|P)^{-\frac{1}{2}} \quad (3.110)$$

are used directly in the ADC equations. Then, every integral in the ADC equations is replaced by (3.110) which introduces an additional sum over the auxiliary basis. For example, the matrix-vector product of the first order terms in the ADC matrix becomes

$$R_{ia}^S = \dots + 2 \sum_P B_{ia}^P \left(\sum_{jb} B_{jb}^P V_{jb}^S \right) - \sum_{jb} \left(\sum_P B_{ib}^P B_{ja}^P \right) V_{jb}^S + \dots \quad (3.111)$$

The first term exhibits an improved scaling behavior of $O(M^3)$ compared to $O(M^4)$ using the standard two-electron integrals. The scaling of the second term, however, becomes worse, since the sum $\sum_P B_{ib}^P B_{ja}^P$ calculates the respective two-electron integral in every multiplication step instead of once in the whole calculation. Thus, the ‘‘direct’’ version of the ADC equations is only useful, if the available memory and disk space is not sufficient to store all two-electron integrals at once.

3.3.3 Local ADC

Though, utilization of the Davidson algorithm provides much shorter computation times for ADC calculations, ADC continues to be too costly for its application to larger systems. One possible route to improve the applicability of ADC is the use of local orbitals. Such local orbital approach is based on the observation that in contrast to the Coulomb interaction the dynamic correlation is a short-range effect with an asymptotic distance dependence $\sim r^{-6}$. As a result, correlation corrections are confined to contributions from neighboring orbitals, while contributions from distant orbitals can be neglected.

In recent years, utilization of local orbitals has become increasingly popular, especially in the ground state methods [81–88]. But also excited state methods have been adapted to benefit from local orbitals [30, 31]. The methods use one of the standard localization algorithms to obtain localized occupied orbitals. Depending on the algorithm the resulting orbitals are called Boys, Edminston-Ruedenberg or Pipek-Mezey orbitals. The algorithms mainly differ in the functional which is minimized during the localization. The Boys orbitals [89, 90] are obtained by minimizing the sum of variance of the orbitals

$$f(\phi_1, \dots, \phi_n) = \sum_i \langle \phi_i | (\mathbf{r} - \langle \phi_i | \mathbf{r} | \phi_i \rangle)^2 | \phi_i \rangle \quad (3.112)$$

while minimization of the self-interaction yields the Edminston-Ruedenberg orbitals [91]

$$f(\phi_1, \dots, \phi_n) = \sum_i \left\langle \phi_i \phi_i \left| \frac{1}{|\mathbf{r}_1 - \mathbf{r}_2|} \right| \phi_i \phi_i \right\rangle \quad (3.113)$$

The Pipek-Mezey algorithm [92] uses the gross Mulliken orbital populations to obtain the localized orbitals. The respective functional for the minimization is given by

$$f(\phi_1, \dots, \phi_n) = \sum_i \sum_A \langle \phi_i | \hat{P}_A | \phi_i \rangle^2 \quad (3.114)$$

where \hat{P}_A represents the projector on the basis functions at atom A :

$$\hat{P}_A = \frac{1}{2} \sum_{\mu \in A} \left[\sum_{\nu} (S_{\nu\mu})^{-1} |\chi_{\nu}\rangle \langle \chi_{\mu}| + \sum_{\nu} |\chi_{\mu}\rangle \langle \chi_{\nu}| (S_{\mu\nu})^{-1} \right].$$

These algorithms perform well for occupied orbitals, since localized orbitals represent deep minima in the occupied space. In contrast, the convergence of the minimization in the virtual space is very slow due to the extensive size of the virtual space and a multitude of local minima of the localization function. Thus, most local methods simply project the virtual space onto the atomic basis, thereby obtaining localized, but not orthonormal orbitals. Lately, also an localization algorithm for virtual orbitals has been devised [93]. It separates the complete orbital space into the occupied space, a valence virtual space and a space of so-called “hard virtuals”. The former two subspaces are created by projecting onto a minimal basis set. They can be localized by one of the standard algorithms above. In the subspace of “hard virtuals” the localized orbitals are obtained by projection on a set of atom-based orthonormal orbitals. These orbitals are specific to atom type and employed basis set, and thus have to be constructed once in advance.

For the implementation of a local variant of the ADC scheme we chose the latter localization procedure in combination with Boys localization to obtain the occupied and valence virtual orbitals.

Modifications to normal ADC

The transformation from HF to localized orthonormal orbitals represents unitary transformations within the occupied and virtual subspaces to which the ADC equations have to be adapted. Since the transformation is unitary and the occupied and virtual orbitals do not mix, there are only a few changes which have to be done. The modifications are all related to the fact that the Fock matrix is no longer diagonal in the basis of localized orbitals:

$$\epsilon_i \delta_{ij} \rightarrow f_{ij} \quad \text{and} \quad \epsilon_a \delta_{ab} \rightarrow f_{ab}$$

Accordingly, the matrix \mathbf{K} becomes

$$\begin{aligned} K_{ia,jb} &= f_{ab} \delta_{ij} - f_{ij} \delta_{ab} \\ K_{iajb,kcld} &= f_{ac} \delta_{bd} \delta_{ik} \delta_{jl} - f_{ik} \delta_{ac} \delta_{bd} \delta_{jl} + f_{bd} \delta_{ac} \delta_{ik} \delta_{jl} - f_{jl} \delta_{ac} \delta_{bd} \delta_{ik}. \end{aligned} \quad (3.115)$$

The second more serious change occurs in parts $\mathbf{C}^{(2)A}$, $\mathbf{C}^{(2)B}$ and $\mathbf{C}^{(2)C}$ of the ADC matrix. The respective terms comprise fractions with orbital energies in the

denominators which cannot be transformed directly. Similar terms also occur in the transition amplitudes. The central problem here is to transform the so-called t-amplitudes

$$t_{iajb} = \frac{\langle ab|ij \rangle}{\epsilon_a - \epsilon_i + \epsilon_b - \epsilon_j} \quad (3.116)$$

into the local basis. This can be done in two ways. On the one hand, the Laplace transform can be employed as in AO-MP2 [94, 95]. On the other hand, eq. (3.116) can be transformed into a system of linear equations for the t-amplitudes. Therefore, the denominator of orbital energy differences in (3.116) is regarded as the multiplication of the inverse of the matrix $K_{iajb,kcld}$ with the integral vector $I_{iajb} = \langle ab|ij \rangle$:

$$\mathbf{t} = \mathbf{K}^{-1}\mathbf{I} \quad (3.117)$$

Multiplying the above equation by \mathbf{K} from the left and transforming into local orbitals yields the system of linear equations

$$\sum_c f_{ac} t_{icjb} - \sum_k f_{ik} t_{kajb} + \sum_c t_{iajc} f_{bc} - \sum_k t_{iakb} f_{jk} = \langle ab|ij \rangle \quad (3.118)$$

This procedure is equivalent to minimizing the Hylleraas functional for MP2 [83]. The linear equations can be solved iteratively which is done in our implementation in advance to the actual local ADC calculation.

For the calculation of transition moments, additional t-amplitudes are necessary. The respective systems of linear equations are given by

$$\sum_c t_{ic}^D f_{ac} - \sum_k f_{ik} t_{ka}^D = \sum_c v_{ic} D_{ca} - \sum_k D_{ik} v_{ka} \quad (3.119)$$

$$\begin{aligned} \sum_c f_{ac} t_{icjb}^D - \sum_k f_{ik} t_{kajb}^D + \sum_c t_{iajc}^D f_{bc} - \sum_k t_{iakb}^D f_{jk} \\ = v_{ia} D_{jb} - v_{ja} D_{ib} - v_{ib} D_{ja} + v_{jb} D_{ia} \end{aligned} \quad (3.120)$$

These have to be solved for each eigenvector v_{ia} of the ADC matrix separately.

Employing Locality

With the above transformation from HF orbitals to local orbitals nothing has been gained yet. Actually, the performance of ADC calculations becomes worse in the

basis of local orbitals due to the localization procedure and the calculation of t-amplitudes. Additionally, the convergence of the Davidson is slower in the local basis, since in this basis the ADC matrix is no longer diagonally dominant. Thus, utilization of local orbitals is only advantageous, if parts of the involved tensors can be neglected. This becomes more easy with growing system-size. Since in larger systems the average distance of the local orbitals increases while the number of nearest neighbors per orbital stays almost identical, more and more terms in the ADC matrix and the ADC vectors become negligibly small. At some point the excess in computational effort can then be overcompensated by excluding negligible contributions from the calculation.

The essential question in local methods is how to select the negligible contributions in advance, so that they never have to be considered during the calculation. Several selection schemes have been devised in the literature [81, 96, 97]. One scheme initially proposed by Pulay [81] defines for every occupied orbital ϕ_i a domain $[i]$ of close-by virtual orbitals. Additionally, pairs of occupied orbitals (ij) are classified into strong, weak, distant and very distant pairs. Based on this partitioning the non-negligible contributions of amplitudes, integrals, etc. are chosen: for every occupied orbital the corresponding domain of virtual orbitals is taken into account, and for important pairs of occupied orbitals the direct product of the respective domains $[ij] = [i] \times [j]$. The scheme has been successfully applied to Møller-Plesset, Coupled-Cluster and other methods [82–88]. However, it has been observed recently [98] that potential energy curves obtained with this local scheme exhibit small artificial discontinuities which due to relatively large changes in the domains and in the classification of orbital pairs with only slight perturbation of the nuclear geometry. They hinder the calculation of gradients and vibrational frequencies.

A second selection scheme [96, 97, 99] which in principle can avoid the problem of discontinuities, utilizes so-called bump functions to select negligible contributions. A bump function is a function which depends on the same orbital indices as the tensors it is applied to. It assumes one if the respective orbitals are near to each other, and zero if they are far apart. In between, it exhibits an arbitrary transition from one to zero. By application of the bump function on a tensor, those parts of the tensor are neglected where the bump function is zero, while the parts where the bump function is one are fully taken into account. The remaining

parts of the tensor are scaled with the value of the bump function. It has been shown [96] that if the bump function exhibits a smooth transition from one to zero the potential energy curves resulting from the calculations will be smooth, too.

In our implementation of local ADC we have employed the latter selection scheme. We first define a one-dimensional function $f(x)$ from which later the actual bump functions can be constructed. At the moment we have chosen the simple step function

$$f(x) = \theta(c_0 - x). \quad (3.121)$$

This function is not continuous, so that the use of the corresponding bump functions can still yield the described discontinuities in the potential energy curves. However, it is much simpler and possesses less adjustable parameters than the smooth bump function proposed in [96] (see also Fig. 3.3)

$$f(x) = \begin{cases} 1, & x < c_0 \\ \frac{1}{1 + \exp\left(\frac{c_1 - c_0}{c_1 - x} - \frac{c_1 - c_0}{x - c_0}\right)}, & c_0 \leq x < c_1 \\ 0, & c_1 \leq x \end{cases} \quad (3.122)$$

In the future, the latter function will replace the step function. Most has already been prepared for this change and the implementation is easily adapted to the more complicated function.

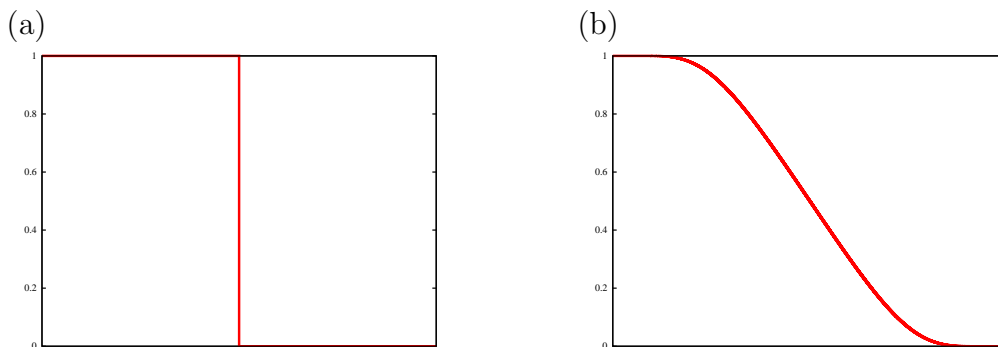


Figure 3.3: The two functions which are used to calculate the bump functions for local ADC. (a) shows the simple θ function, while (b) shows the more complicated, but smooth function proposed by Subotnik et al. [96, 97]

Now, the bump functions have to be constructed from $f(x)$. Most straightforward is the formation of a bump function with two orbital indices b_{pq} by choosing x to be a measure for the distance of the two orbitals

$$b_{pq} = f(x), \quad \text{with } x = |\langle \phi_p | \mathbf{r} | \phi_p \rangle - \langle \phi_q | \mathbf{r} | \phi_q \rangle| - \sigma_p - \sigma_q. \quad (3.123)$$

Bump functions with more indices can be obtained by combining multiple two-index bump functions via multiplication $b_{pq}b_{rs}$ or summation $b_{pq} + b_{rs} - b_{pq}b_{rs}$. Here, the additional negative term in the expression for the summation has been introduced to keep the result of the sum in the interval $[0, 1]$. As distance measure x , the distance of the orbital centers minus the variances of the two orbitals has been chosen. But, other distance measures are also possible. A good alternative would probably be the overlap of absolute orbitals

$$x = \int d\mathbf{r} |\phi_p(\mathbf{r})| |\phi_q(\mathbf{r})|. \quad (3.124)$$

In [96] it has been suggested to utilize the values of two-electron integrals as x . Then, bump functions with four indices would be directly available. However, the same authors argue in [97] that this would be computationally expensive.

The application of bump functions and the use of “bumped” tensors in the ADC calculations require the reorganization of the tensors to yield an efficient implementation. Since grouping of non-zero elements makes tensor contractions most efficient, a block structure is imposed on the tensors. The block structure should be such that only a few blocks of a “bumped” tensor will contain non-zero elements. To achieve this the occupied and virtual orbitals are sorted separately into domains of near-by orbitals. This is done using the two-index bump function 3.123 and a simulated-annealing algorithm [96]. The resulting orbital domains already form the required block structure via the tensor indices. In the next step, the orbital domains are classified pairwise into important, intermediate and negligible domain pairs. Important domain pairs are those where the bump function b_{pq} yields one for every orbital pair, while in case of negligible domain pairs the bump function always yields zero. With these domain pairs the tensor blocks can easily be categorized as negligible or non-negligible. Since negligible blocks do not need to be stored nor processed, this saves computation time and storage space. If the

bump functions can assume other values than zero and one, the non-negligible blocks are furthermore divided into those blocks whose elements would be scaled by one when the bump function is applied and those whose elements would be scaled by a value smaller than one. This also saves computation time, because only the latter blocks have to be scaled by the bump function.

The remaining questions concerning the implementation of local ADC are “Which tensors in the ADC equations should actually be subjected to a bump function?” and “How should the bump functions for the tensors with more than two orbital indices look like?”. Both questions cannot definitely be answered. For the moment, we have chosen the doubly excited configurations part of the ADC vectors v_{iajb} alone to be subjected to a bump function. Other tensors have been excluded from this treatment out of various reasons. The singly excited configurations v_{ia} , for example, cannot be subjected to the bump function without losing charge transfer excitations. For two-electron integrals $(pq|rs)$ and t-amplitudes t_{iajb} a bumping scheme has been suggested in [97]. However, for the moment we have excluded them from the treatment in order to again reduce the number of adjustable parameters.

What remains is to find a suitable bump function which can be applied to the doubly excited configurations. Since it is not clear what the optimal bump function would be, we have decided to implement multiple bump functions in order to test which “bumping model” performs best (see section 4.2.2). In total we have implemented four different bump functions $b_{iajb}^{(1)}, \dots, b_{iajb}^{(4)}$ which have all been constructed from the two-index bump function (3.123). Two of these bump functions are based on *a priori* models, i.e. they do not depend in any way on the excited states that are to be calculated but only on the distances of orbital pairs. The other two bump functions rely on estimates for the singly excited configurations of the excited states which are to be calculated. Graphical representations of the four underlying bumping models are given in Figure 3.4.

In the model yielding the first bump function $b_{iajb}^{(1)}$, the doubly excited configurations are conceived as combination of two single excitations. They are selected as important, if at least one of the contained single excitations is local. Besides, either the other single excitation must be local, too, but can have arbitrary distance to the first, or one of the orbitals of the second single excitation must be

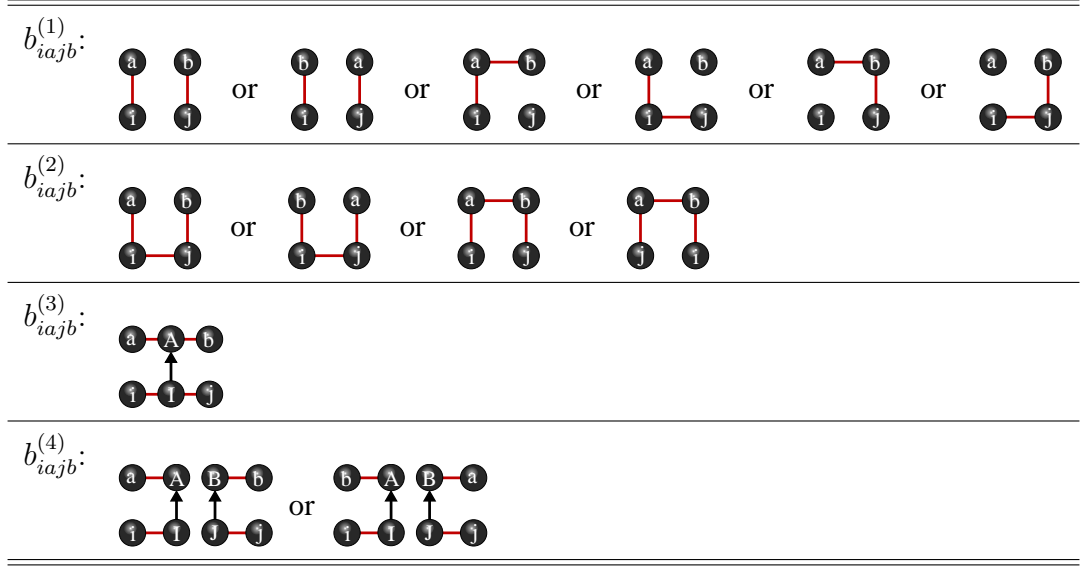


Figure 3.4: Graphical representation of the four implemented bumping models. The black spheres with lower-case letters represent the orbitals or orbital indices the bump function will act on. The red bars between the spheres show which pairs of orbital have to be near each other so that the bump function does not assume zero. In the two latter models, the spheres with upper-case letters and a black arrow in-between represent important single excited configurations of the excited states which are to be calculated.

near to the first. The mathematical expression for the bump function adds up to

$$b_{iajb}^{(1)} = (b_{ia}b_{jb}) \parallel (b_{ib}b_{ja}) \parallel [(b_{ij} \parallel b_{ab}) (b_{ia} \parallel b_{jb} \parallel b_{ib} \parallel b_{ja})] \quad (3.125)$$

where \parallel represents the modified summation $b_{pq} \parallel b_{rs} = b_{pq} + b_{rs} - b_{pq}b_{rs}$ described above. It is straightforward to show that the application of this bump function can reduce the size of the doubly excited configurations from $O(M^4)$ to $O(M^2)$, if the number of near-by orbitals is assumed to be constant.

The second model can reduce the size of the tensors v_{iajb} even to $O(M)$, since it enforces each occupied orbital to be near one of the virtual orbitals, and the occupied or the virtual orbitals to be near to each other. The mathematical expression of the corresponding bump function is given by

$$b_{iajb}^{(2)} = (b_{ij} \parallel b_{ab}) [(b_{ia}b_{jb}) \parallel (b_{ib}b_{ja})] \quad (3.126)$$

In the third and the fourth model, estimates for the single excited configurations of the requested excited states are calculated, first, by diagonalizing only the part $M_{ia,jb}$ of the ADC matrix. From the resulting eigenvectors the most important entries are selected. This is done based on the following scheme. Suppose n excited states shall be calculated, then one obtains from the partial diagonalization n eigenvectors $x_{1;ia}, \dots, x_{n;ia}$. From the n eigenvectors the sum

$$s_{ia} = \frac{1}{n} \sum_{p=1}^n x_{p,ia}^2$$

is computed. The elements s_{ia} are then sorted by size so that $s_0^{\text{sorted}} > s_1^{\text{sorted}} > \dots > s_X^{\text{sorted}}$. Now, the finite series

$$S_m = \sum_{I=0}^m s_I^{\text{sorted}}, m = 0, \dots, X$$

is formed which is monotonic increasing with $0 < S_m \leq 1$. By subjecting every element S_m of the series to the function $f(x)$ which was used in the construction of the bump function, the largest element S_k for which $f(S_k) \neq 0$ can be obtained. Here, the parameter c_0 is set to 0.7 for $f(x)$ being the step function. The element S_k finally yields the important single excited configurations which are all those contributing to S_k .

The important singly excited configurations are utilized by the third model in such way that the occupied orbitals of the doubly excited configurations have to be near the occupied orbital of one of the singly excited configurations. Is this the case then the virtual orbitals also must be close to the virtual orbital of the same singly excited configuration. The expression for the bump function then looks like

$$b_{iajb}^{(3)} = b_{iI} b_{aA} b_{jI} b_{bA} \quad \text{with } (IA) \in \{\text{important singles}\}. \quad (3.127)$$

Assuming that the number of important singly excited configurations scales like $O(M)$ the size of the doubly excited configurations scales likewise after application of this bump function.

In the fourth model the doubly excited configurations are again conceived as consisting of two single excitations. Each single excitation then has to be close to

any of the important singly excited configurations. Accordingly, the bump function is expressed as

$$b_{iajb}^{(4)} = (b_{iI}b_{aA}b_{jJ}b_{bB}) \parallel (b_{iI}b_{bA}b_{jJ}b_{aB}) \quad \text{with } (IA), (JB) \in \{\text{important singles}\}. \quad (3.128)$$

Since there are two important singly excited configurations in the expression, the application of $b_{iajb}^{(4)}$ reduces the size of the doubly excited configurations to $O(M^2)$.

Application of any of the above bump functions to the doubly excited configurations v_{iajb} can also be seen as application of the same bump function to the ADC matrix from both sides. This becomes clear if the matrix-vector product of the ADC matrix with an arbitrary vector $\mathbf{r} = \mathbf{M}\mathbf{v}$ is considered. Applying the bump function to \mathbf{v} as well as to \mathbf{r} results in

$$b_{ia}r_{ia} = \sum_{jb} b_{ia}M_{ia,jb}b_{jb}v_{jb} + \sum_{jbkc} b_{ia}M_{ia,jbkc}b_{jbkc}v_{jbkc} \quad (3.129)$$

$$b_{iajb}r_{iajb} = \sum_{kc} b_{iajb}M_{iajb,kc}b_{kc}v_{kc} + \sum_{kcl d} b_{iajb}M_{iajb,kcl d}b_{kcl d}v_{kcl d} \quad (3.130)$$

where $b_{ia} = 1$. Since the application of the bump function reduces the size of the doubly excited configurations, the dimensionality of the ADC matrix is reduced implicitly at the same time. Thus, some eigenvalues of the ADC matrix are lost after the use of the bump function. They are most likely in the region of large eigenvalues which are in general not the eigenvalues of interest. However, this has to be tested for each of the bump functions.

Chapter 4

Applications

4.1 Energy and Electron Transfer Processes in Photosynthesis

Photosynthesis enables green plants, algae and purple bacteria to utilize sun light as their energy source. During this process incident light is absorbed, and the excitation energy is converted into chemical energy by a sequence of energy and electron transfer steps. The initial step of photosynthesis, the absorption of light, is achieved by antenna proteins, the so-called light-harvesting complexes (LHCs), which are present in every known photo-synthetic organism [100]. They are responsible for efficient absorption and transport of light energy to the reaction center where the conversion into chemical energy takes place. The LHCs differ in structure and pigmentation, as well as in the additional functions, like energy dissipation or structural integrity that they fulfill in the respective organism. In recent years, the molecular structure of several LHCs has been resolved by X-ray crystallography [101–105]. However, this has not yet lead to full understanding of the molecular details of the processes within the LHCs. Present-day research tries to acquire more information about these processes, e.g. by elaborate femtosecond laser experiments [18, 106–110]. But interpretation of the resulting optical spectra is difficult. Quantum chemistry can assist in the interpretation [111–113]. Starting from the molecular structures of LHCs that are available with atomic resolution, model systems for observed processes can be constructed which are then used in quantum chemical calculations. Comparison of the outcome of the calculations

with experimental findings can uncover the details of the processes in LHCs.

4.1.1 Quantum Chemical Approach

Theoretical investigation of excitation energy transfer (EET) and electron transfer (ET) processes in LHCs is a rather difficult task. On the one hand, the absorption of photons as well as the subsequent ultra-fast EET and ET processes are quantum mechanical events that in general require quantum chemical treatment. On the other hand, LHCs are huge proteins containing many pigment molecules which themselves are already quite large to be described quantum chemically. Since quantum chemical methods yielding good accuracy are restricted to system sizes of up to 30 atoms of the second row of the periodic table, the essential problem is the need of quantum mechanical treatment for systems that are too large.

Dipole approximation and excitonic coupling theory provide a way to circumvent this problem. Here, the electronic excited states of individual pigments are calculated or measured, first. Afterwards, the pigment-pigment interactions are dealt with in separate calculations. This way, reasonable estimates of Förster energy transfer rates in e.g. PS1 and LHC-II have been obtained [113–115]. However, this procedure is valid only if the involved pigments are weakly coupled. In the strong-coupling regime, as it is the case for the chlorophyll dimers in LHC-II [101, 102, 116], other quantum mechanical effects than pure electrostatics become important. Then, one has to resort to a different route for the investigation of EET and ET processes.

As approach that facilitates calculations also in the strong coupling regime we employ a so-called super-molecular approach [55, 56, 111, 117–119]. In this approach, the excited states of spatially close pigment pairs are calculated together in one quantum chemical calculation. Afterwards, excited state calculations are performed on each pigment separately. The comparison of the individual spectra with the joint spectrum yields detailed insights into the mutual influence of the pigments. Since all quantum effects are included here, also information about ET and EET mechanisms via conical intersections can be obtained. Yet, the size of chlorophylls (Chls) and carotenoids (Cars) that are the typical pigments in LHCs restricts the applicable excited state methods to only approximate methods like semi-empirical models, configuration interaction singles or time-dependent density

functional theory. Even with these methods an adequate treatment of the protein environment is hardly possible due to computational and technical limitations. Thus, the molecular models for the pigment pairs have to be as small as possible to allow for efficient and most reliable calculation of the excited states. But at the same time they must be as big as necessary to capture the physical properties of interest.

In general, molecular models are constructed from an experimentally known structure of the pigment protein, typically an X-ray structure. The first step is to extract the pigments of interest from the structure to form the model complex. Long side chains like the phytyl chain of Chls are stripped off, if they are not expected to influence the excited states of the pigments. Also, nearby amino acid residues might be added when an strong influence on the excited states can be anticipated. Since hydrogen atoms are normally not resolved by X-ray crystallography, they have to be added as well. This is not always unambiguously possible due to unknown charges of atoms or side groups like in case of a terminal oxygen atom that can correspond to a neutral OH group or to an O⁻ anion. Then, a geometry optimization has to be performed to adjust the geometrical parameters of the pigments. Thereby, the relative position and orientation of the pigments must remain unchanged because it determines the interaction of the pigments. In the end, the validity of the model has to be checked by calculation of the excited states of interest and comparison of the results with experimentally known values. This way, reasonable molecular models with 100 to 200 atoms for pigment pairs in LHCs can be obtained which serve as input for the investigation of the EET and ET processes.

The excited states methods applicable to model complexes of that size are CIS and TD-DFT (see Section 3.2.1 and 3.2.2). However, both methods have severe limitations as described previously. In case of CIS, there are errors in the calculated excited states of up to 1 eV and the wrong ordering of states due to an unbalanced description of electron correlation. TD-DFT, in contrast, yields excitation energies of valence excited states with remarkable accuracy of only 0.1–0.5 eV. Especially, the excitation energies of the lowest excited state $2A_g^-$ of linear polyenes and carotenoids become reasonably good with TD-DFT using a generalized-gradient corrected (GGA) xc-functional like BLYP [54–56, 120]. However, it can be shown that these results rely on fortuitous cancellation of errors [61]. If geometries and

other excited state properties also benefit from the error cancellation remains unclear. Still, the vertical excitation energies at ground state geometries obtained with TD-DFT are good estimates for the lowest excited states of Chls and Cars. The more serious problem of TD-DFT is its failure in calculating CT states correctly (see Section 3.2.3). To overcome this problem both TD-DFT and CIS can be combined via the Δ DFT method as described in Section 3.2.3. The resulting CT energies together with the excitation energies of the valence excited states obtained from TD-DFT calculations yield all relevant excited states of the model complexes. Thus, meaningful investigation of ET and EET processes in pigment pairs is possible using reasonable molecular models for the pigment interactions in LHCs in combination with TD-DFT and CIS.

4.1.2 Light-Harvesting Complex 2 in Purple Bacteria

In recent years, light-harvesting complexes LH2 of purple bacteria have been subject of intense research [15, 17, 104, 105, 107, 109, 111, 121–138]. The structures of LH2 of *Rhodopseudomonas (Rps.) acidophila* [104, 121] and of *Rhodospirillum (Rs.) molischianum* [105] have been determined by X-ray crystallography. Additionally, the LH2 of *Rhodobacter (Rb.) sphaeroides* has been found to have a similar structure as the LH2 from *Rps. acidophila* [122]. All three antenna proteins possess a ring-like structure consisting of several similar subunits. In *Rs. molischianum* there are 8 such subunits, while the other two LH2 are composed of 9 subunits. Each subunit comprises three bacteriochlorophyll *a* (BChl) molecules and one carotenoid (Car) that are embedded in two polypeptide chains. The BChl molecules are arranged in two rings along the circular structure of the LH2. The ring of strongly coupled BChl molecules is formed by the two BChls (B850) of each subunit whose porphyrin rings are oriented perpendicular to the ring plane. The other BChls (B800), one per subunit, form the second weakly coupled ring that resides at mid-height of the LH2 complexes. The orientation of the B800 BChls is parallel to the ring plane in *Rps. acidophila*, while it is 38° tilted out of plane in *Rs. molischianum*. The carotenoid molecules span the height of the LH2 complexes, thereby interacting with both rings of BChl molecules. Depending on the species different Car molecules are present in the LH2s. The LH2 of *Rps. acidophila* contains rhodopin glucoside which has a conjugation length of eleven C=C bonds ($n = 11$). Lycopene being the Car present in LH2 of *Rs. molischianum* possesses the same conjugation length. In *Rb. sphaeroides* spheroidene is found that has conjugation length of only $n = 10$.

In LH2 complexes incident light is absorbed by all pigment molecules, BChls and Cars, which together cover a large part of the visible spectrum. The excitation energy is transferred from Cars and B800 BChls to the low-lying Q_x and Q_y states of the B850 BChls [139–141]. From there, the EET proceeds via adjacent protein complexes to the reaction center. The efficiencies of the initial EET processes inside LH2 strongly depend on the distance and orientation of donor and acceptor molecules, as well as on the properties of the involved electronic states [141]. For the Car→BChl EET, either the optically allowed S_2 state ($1B_u^+$ in C_{2h} symmetry) or the optically forbidden S_1 state ($2A_g^-$) can serve as donor states. But, also other

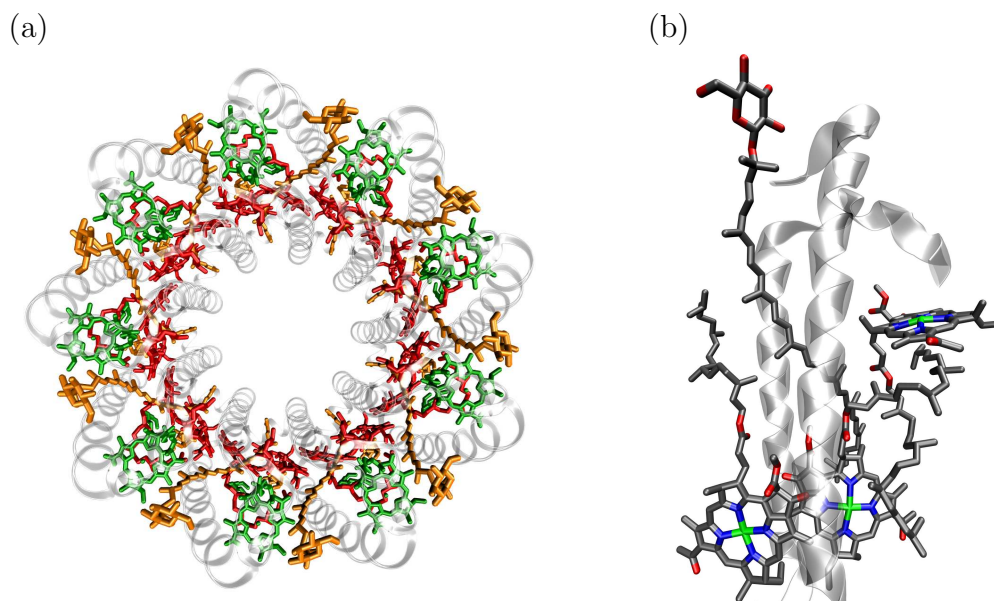


Figure 4.1: Structure of light-harvesting complex LH2 of *Rhodospseudomonas (Rps.) acidophila*: (a) Complete circular arrangement with 9 subunits, top view. (b) Structure of one subunit, side view

dark states, like S^* [18, 106] and S^\ddagger [108], which are supposed to be located between S_1 and S_2 , might be involved in the Car–BChl energy transfer. The properties of all these states are influenced by the conjugation length of the π -electrons in the carotenoid backbone and the functional groups attached to it.

The efficiency of the EET via the S_2 route has been found to be 40%–60%. But, no significant changes with conjugation length of the carotenoid have been observed [15, 125, 142]. In contrast, the pathway via the S_1 state exhibits large changes in efficiency with conjugation length N [126, 129] (N : number of conjugated double bonds). In a sophisticated transient absorption experiment on a series of reconstituted LH2 complexes from *Rb. sphaeroides* containing different carotenoids, Polívka *et al.* [109] have recently shown that the efficiencies of the $S_1 \rightarrow Q_y$ EET drop with increasing conjugation length of the carotenoid. Starting at 94% for neurosporene (Neuro, $N=9$), the efficiency decreases to 80% for spheroidene (Spher, $N=10$) and becomes as low as 76% for spheroidenone (Spherone, $N=11$).

Besides the Car \rightarrow BChl EET pathways, electron transfer from Car to BChl has also been observed in recent experiments [107, 109]. After excitation of the S_2

state the spectral signature of the spheroidene radical cation was found in experiments on *Rb. sphaeroides*. In *Rps. acidophila* and *Rs. molischianum*, however, no Car radical cation formation could be observed. With the previously mentioned experiment on reconstituted LH2 [109] it could be established that like in case of the S_1 -mediated EET also the efficiencies of Car radical cation formation in LH2 become smaller with increasing conjugation lengths. The efficiencies of Car radical cation formation range from 10%–15% in case of Neuro via 5%–8% in case of Spher to no Car radical cation signal in case of Spherone. Yet, the detailed molecular mechanism for Car radical cation formation in LH2 complexes remains to be established.

To get deeper insight in the process of carotenoid radical cation formation in LH2 complexes we have investigated the possibility of Car→BChl electron transfer in LH2 subunits employing the theoretical methodology described in Section 4.1.1.

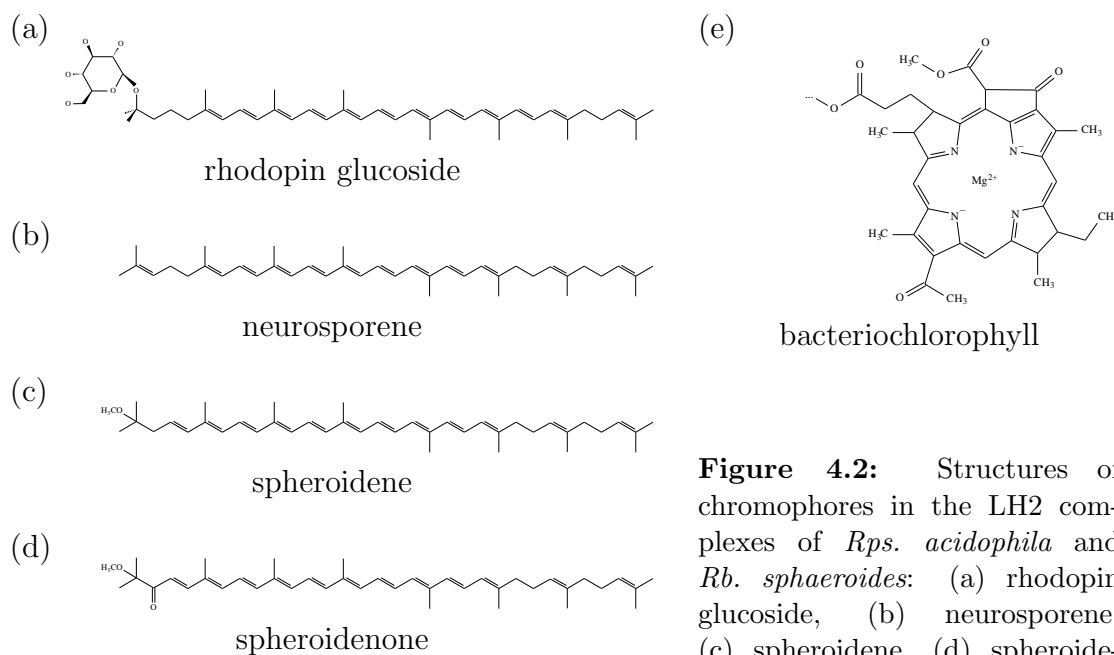


Figure 4.2: Structures of chromophores in the LH2 complexes of *Rps. acidophila* and *Rb. sphaeroides*: (a) rhodopin glucoside, (b) neurosporene, (c) spheroidene, (d) spheroidenone, and (e) bacteriochlorophyll.

Construction of model complexes

The first step in the investigation of Car–BChl ET processes in LH2 of *Rb. sphaeroides* is the construction of suitable model complexes. As starting point for the

construction serves the crystal structure of the LH2 complex of *Rps. acidophila*, since it is known to be similar to the structure of the LH2 complex of *Rb. sphaeroides*, which is not available at present. From the crystal structure, one rhodopin glucoside molecule, the native carotenoid in LH2 of *Rps. acidophila*, and the spatially closest B800 BChl molecule are extracted. The choice of the BChl molecule is due to experimental evidence that B800 BChl is most likely the electron acceptor in the ET processes [107, 109]. The rhodopin glucoside molecule is replaced by either neurosporene, spheroidene or spheroidenone, respectively, resulting in three Car–B800 BChl model complexes. After adding the non-resolved hydrogen atoms, the model complexes are optimized using DFT with the BLYP functional and the 3-21G* basis set to account for inaccuracies in the crystal structure and variations in the 3D structures of LH2 in *Rps. acidophila* compared to *Rb. sphaeroides*. Constraints are applied during the optimizations to incorporate spatial restrictions due to the protein environment. Since the spatial restrictions are indefinite, three different sets of constraints are tested, successively. First, only the end groups of the Car molecules are optimized. The resulting geometries are used as starting structure to the second optimizations, in which the positions of the Car end groups are kept fixed while the rest of the Car molecules is optimized. The last optimizations allow for the model complexes to relax freely keeping only distance and orientation of the Car and BChl molecules fixed.

Table 4.1: Excitation energies and oscillator strengths (in brackets) of the lowest excited states of the Spher–BChl complex calculated with TDA/BLYP/3-21G at the geometries obtained from the three optimizations. Experimental excitation energies are given for comparison. All excitation energies are specified in eV.

Ex. State	Q_y	S_1	Q_x	S_2
Opt. 1	2.03 (0.657)	2.09 (0.011)	2.16 (0.037)	–
Opt. 2	2.02 (0.688)	1.96 (0.011)	2.17 (0.035)	2.28 (5.819)
Opt. 3	2.15 (1.053)	1.95 (0.003)	2.26 (0.511)	2.28 (5.370)
Exp.	1.56	1.6–2.0	2.10	2.42

The geometries of the model complexes resulting from any of the optimizations are evaluated by comparison of calculated electronic excited states with experimental data (Table 4.1). The excited states calculation are performed using the

Tamm-Dancoff approximation to TD-DFT with the BLYP xc-functional and the 3-21G basis set. The experimental values for the S_2 , Q_x , and Q_y states are taken from Polívka *et al.* [109]. The vertical excitation energy of the optically forbidden S_1 state is not accessible experimentally, and thus it can only be estimated. For all optimized geometries the calculated excitation energies of the S_1 , S_2 and Q_x states are in acceptable agreement with experimental values, since they deviate by less than 0.2 eV. The calculated BChl Q_y energies exhibit larger deviations from the experimental value. For the first two sets of optimized geometries the deviation is 0.5 eV and for the third set it is 0.6 eV. The worse agreement of the calculated BChl states with experimental values for the third set of optimized geometries, as well as the missing natively bent structure of the Cars which was lost during the respective optimizations lead to the discard of these geometries. The accuracy of the calculated excitation energies for other two sets of optimized geometries is quite similar. However, for the first set of optimized geometries the plethora of artificial CT states that is present in all TD-DFT calculations of the model complexes and additional convergence problems prevent the calculation of the Car S_2 state. Thus, the geometries obtained from the second optimizations are chosen to be employed in all subsequent investigations.

Influence of the protein environment

The construction of Car–BChl model complexes involved removal of the polypeptide chains and other surrounding molecules from the crystal structure of the LH2 complex. Their influence on the spatial arrangement of the Car and BChl molecules has been accounted for by the constraints applied during the optimizations of the complexes. Yet, other effects of the environment on the model complexes due to e.g. electrostatic interaction have not been considered. The incorporation of such effects into the model calculations is difficult. Several approaches have been tested where interactions of the models with the surrounding can be included.

One possibility to include the effects of the protein environment in the model calculations is to add selected amino acid residues to the molecular models which have strong influence on the excited states of interest. In case of the LH2 complex one such amino acid residue is the arginine residue βArg_{20} close to one of the

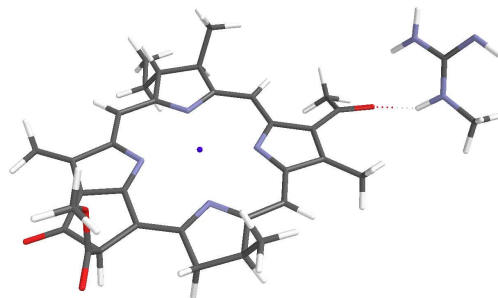


Figure 4.3: β Arg₂₀-BChl model complex.

carbonyl groups of BChl (Figure 4.3). It has been shown that TDA/BLYP calculations of BChl including this residue result in shifted BChl excitation energies which are closer to the experimental values [19]. Since in our model calculations the BChl excitation energies exhibit the largest deviation from the experimental values, modified model complexes comprising Car, BChl and β Arg₂₀ could in principle be used as improved molecular models for LH2 ET processes. However, excited state calculations on such model complexes show a multitude of additional CT states from Car or BChl to arginine which all suffer from the CT problem of TD-DFT. These CT states are found at much too low energies and thus, are not relevant in the Car radical cation formation. The calculation and interpretation of other states is greatly complicated by the extra CT states due to mixing of CT and non-CT states and the increased amount of excited states which have to be calculated. Consequently, the use of Car-BChl- β Arg₂₀ model complexes is not advisable. Additionally, the focus of the model calculations is on the Car excited states and the lowest ET states what suffices the use of the more simple Car-BChl model complexes.

Other possibilities how the influence of the protein environment can be accounted for are solvent models or the approximation of the surrounding molecules by point charges. These methods cover predominantly electrostatic effects of the environment on the model complexes. In case of continuum solvent models the environment is described by means of one dielectric constant whose value has to be determined beforehand. Yet, a meaningful dielectric constant may be different at different points along the model complexes. This makes definite assignment of the dielectric constant problematic. Additionally, all implementations of contin-

uum solvent models available today are intended for the use with ground state methods, and not for the calculation of excited states. The use of point charges as description for the protein environment is more straightforward. Point charges which model the environment sufficiently well can easily be retrieved from the crystal structure via partial charges assigned to atoms by some molecular dynamics parameter set. The resulting field of point charges can be included directly in any quantum chemical calculation. However, in case of LH2 model complexes no calculations including point charges are possible, since the SCF fails to converge due to over-polarization. Thus, no effects of the protein environment other than spatial restrictions are incorporated in our model calculations.

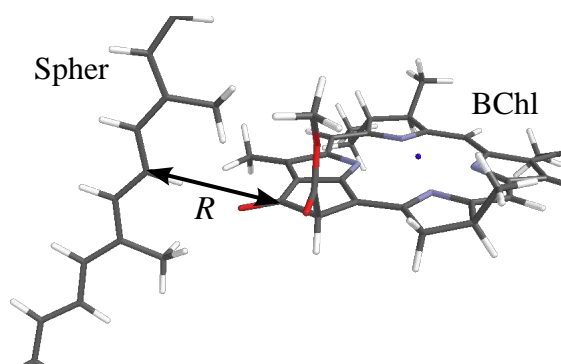


Figure 4.4: Intermolecular distance coordinate R between Car and BChl along which the potential energy curves of the Car–BChl model complexes have been calculated.

Potential energy curves

The model construction described above has yielded three model complexes: Neuro–BChl, Spher–BChl and Spherone–BChl. For each model complex potential energy curves are calculated along an intermolecular distance coordinate R . The distance coordinate R is defined as the distance between the ring carbonyl group of BChl and the spatially closest carbon atom of the Car molecule (Figure 4.4). At different values of R ranging from 3 Å to 9 Å the BChl Q_x and Q_y states, and the Car S_1 and S_2 states are calculated using TDA/BLYP/3-21G. For the calculation of the two lowest CT states the TD-DFT/CIS hybrid approach is employed as described

in Section 4.1.1. Both CT states correspond to excited states in which an electron has been transferred from the Car to the BChl. This can be deduced from the respective detachment and attachment densities (Figure 4.5), since in both cases the detachment density is located completely on the Car, while the attachment density is found solely on the BChl. Such $\text{Car}^+ - \text{BChl}^-$ states are responsible for the experimentally observed carotenoid radical cation signal.

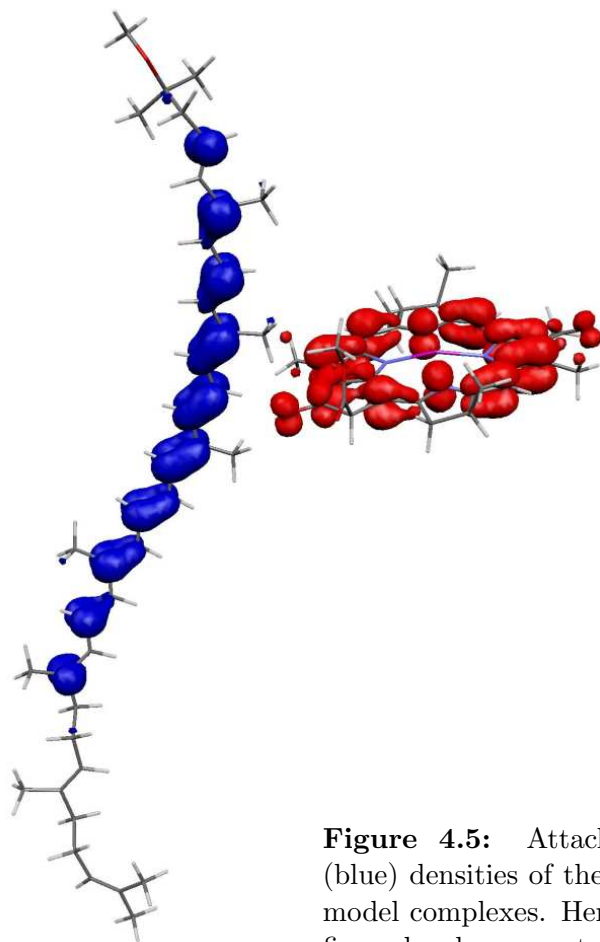


Figure 4.5: Attachment (red) and detachment (blue) densities of the lowest CT state of Car-BChl model complexes. Here: Spher-BChl complex. This figure has been created using MOLEKEL [143].

The computed potential energy curves for the three model complexes are displayed in Figure 4.6. In all graphs the ground states (black lines) and the valence excited states have rather flat curves with a minimum around 3.3 Å. The curves of the CT states (red lines) show the expected $1/R$ dependence due to the electrostatic attraction of oppositely charged Car and BChl molecules. Their rather

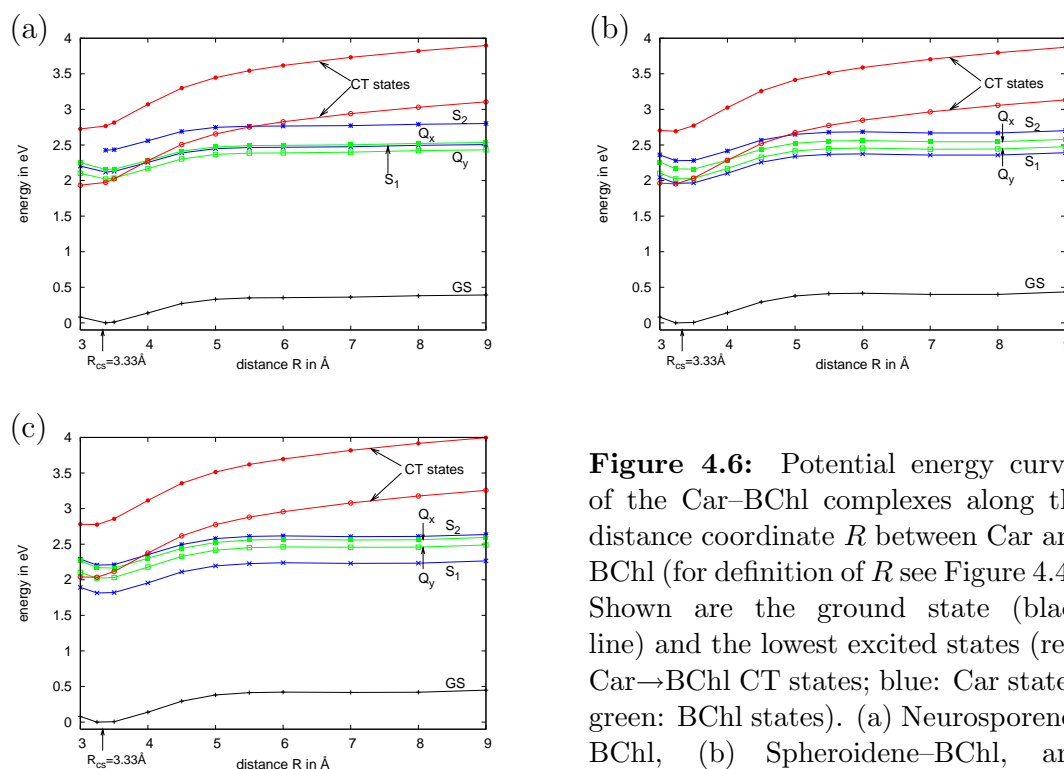


Figure 4.6: Potential energy curves of the Car–BChl complexes along the distance coordinate R between Car and BChl (for definition of R see Figure 4.4). Shown are the ground state (black line) and the lowest excited states (red: Car \rightarrow BChl CT states; blue: Car states; green: BChl states). (a) Neurosporene–BChl, (b) Spheroidene–BChl, and (c) Spheridenone–BChl.

steep slopes and their relatively high energies at large distances R result in several crossings of charge transfer and valence excited states for all model complexes. Such crossings are necessary prerequisites to make efficient ET possible. Thus, the chosen intermolecular separation coordinate is most likely the relevant one mediating the Car \rightarrow BChl ET process [144]. The major differences between graphs of different model complexes are the energetic positions of the excited states. While the BChl Q_x and Q_y states (green lines) have almost identical excitation energies for all Car–BChl complexes, the excitation energies of the Car S_1 and S_2 states (blue lines) change depending on the Car molecule in the complex. They show the experimentally observed decrease in excitation energy with increasing conjugation length N of the Car. At equilibrium distance, this results in S_2 energies of 2.43 eV for Neuro ($N=9$), 2.28 eV for Spher ($N=10$) and 2.21 eV for Spherone ($N=11$). The energetic positions of the CT states also vary depending on the model complex. The lowest CT state is found at similar excitation energies in case

of Neuro-BChl and Spher-BChl, but for Spherone-BChl its excitation energy is increased by about 0.15 eV. The second CT state is higher in energy than the first by about 0.75 eV for all three model complexes, and thus exhibits the same behavior.

The variations in the energetic positions of the excited states for different model complexes also cause changes in the distances R at which crossings of CT and valence excited states occur. For instance, the lowest CT state crosses the S_2 state at 5.5 Å for Neuro-BChl, 4.8 Å for Spher-BChl, and 3.6 Å for Spherone-BChl. Similarly, the crossing with the S_1 state is shifted to smaller distances with increasing conjugation length N of the Car molecule. These crossings are located at 3.9 Å for Neuro-BChl and at 3.3 Å for Spher-BChl, while for Spherone-BChl no such crossing can be observed. The BChl Q_x and Q_y states are also crossed by the lowest CT state. In Neuro-BChl and Spher-BChl the crossings occur at 4 Å and 3.5 Å, respectively. In Spherone-BChl they are shifted to smaller distances by about 0.3 Å due to the increased energy of the CT state. However, as stated before, the calculated energies of BChl excited states are too high compared to the experimental values. Thus, the positions of crossings of the lowest CT state and BChl excited states are erroneous. Especially, the experimental value of the Q_y energy is so low that no crossing of Q_y and the lowest CT state is expected in any of the three complexes. Regarding the second CT state, its energetic position is that high in all model complexes that no crossings with any of the valence excited states can be observed.

Electron Transfer Pathways

In the transient absorption experiment by Polívka *et al.* [109] the EET and ET dynamics in LH2 complexes have been studied upon excitation of the Car S_2 states of Neuro, Spher and Spherone, respectively. To explain the experimental observations by means of our calculations it is necessary to analyze the computed potential energy curves with respect to possible energy transfer pathways from the S_2 state to a CT state.

The potential energy curves in Figure 4.6 show that for Neuro-BChl and Spher-BChl the curve of the lowest CT state crosses the curves of the S_1 , S_2 , and Q_x states and drops with decreasing intermolecular separation at some point below

them. For the Spherone–BChl complex, however, this CT state crosses only the curves of the S_2 and Q_x states and has a higher energy than S_1 over the complete distance range. Population of a CT state can in principle proceed via all the excited states for which a crossing with the CT state can be found, so that at equilibrium distance these states are higher in energy than the CT state. Thus, based on energetic arguments alone the lowest CT state can be reached from S_1 , S_2 and Q_x states in Neuro–BChl and Spher–BChl. In Spherone–BChl only S_2 and Q_x states, and not the S_1 state, can decay into the lowest CT state and lead to Car radical cation formation. Similarly, the second CT state cannot be populated from any of the mentioned valence excited states in any of the model complexes, since it exhibits no crossings with any of these states. Hence, this state can be excluded from the subsequent discussion.

Experimentally, the formation of Car radical cations has been observed for the LH2 complexes with Neuro and Spher, but no signal of a Spherone radical cation has been found [109]. Since our calculations show that the population of the CT states, i.e. radical cation formation, in the Spherone containing LH2 is in fact energetically possible via $S_2 \rightarrow \text{CT}$ and $Q_x \rightarrow \text{CT}$, but no signal is experimentally observed, these pathways can be excluded as relevant ones. As described below, the transfer from S_2 and Q_x states to the CT state competes with other, ultra-fast decay channels which make the pathway to the CT state unfavorable. Furthermore, the $S_1 \rightarrow \text{CT}$ pathway is energetically only possible for the Neuro and Spher complexes, and indeed a Car radical cation is observed. Thus, it is very probable that the population of the CT state proceeds only via $S_1 \rightarrow \text{CT}$. Though, experimentally, this electron transfer pathway has been excluded by Polívka *et al.* [109] due to lifetime arguments, they have pointed out that the population of the CT state is still possible via a vibrationally excited S_1 state. Equally well, the CT state might be populated via the S^* state which is not present in our calculations, but experimental arguments are given that it may be located in the relevant energy regime between S_1 and S_2 . With the same reasoning as in the case of the S_1 state, the experiments suggest that the population of the ET state would have to occur via a vibrationally excited S^* state.

From our calculations on the different Car–BChl complexes the schematic energy level diagram in Figure 4.7 can be deduced which provides a more general look at the possible EETs and ETs in the LH2 complex. Upon photo-excitation, the

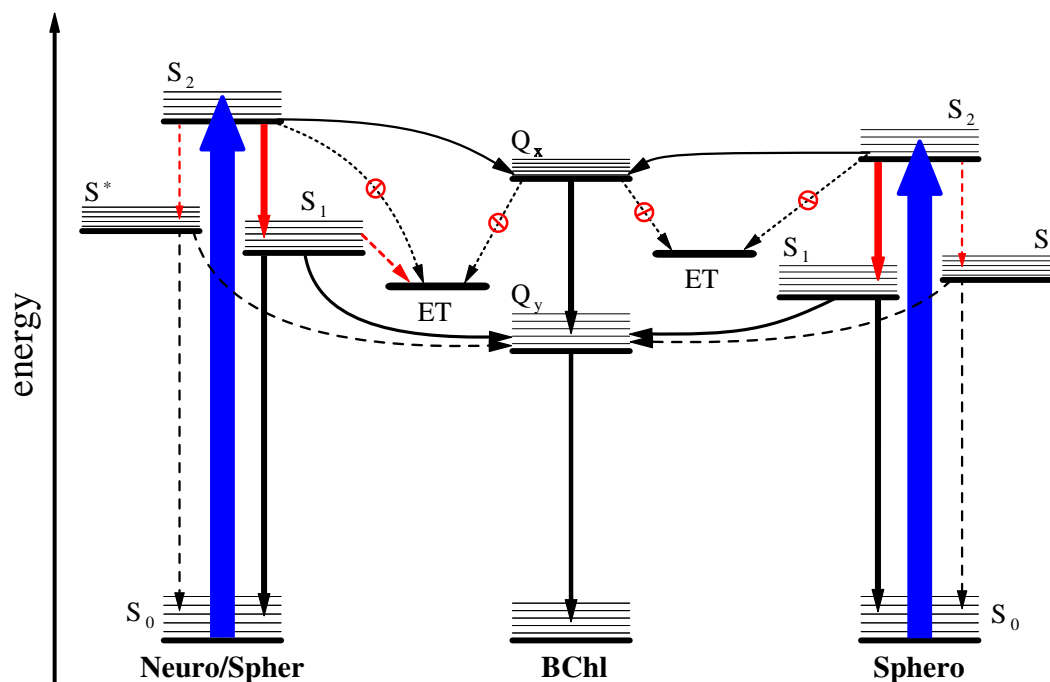


Figure 4.7: Schematic energy level diagram for the EET and ET processes in Car–BChl complexes.

S_2 state can in principle decay into five different states which are either via EET to the BChl excited states, Q_x and Q_y , or via internal conversion to the Car S_1 and S^* states, or via electron transfer to the CT state. Experimentally, EET into the BChl excited states has a high efficiency, and 40%–60% of the S_2 excitation energy is usually transferred to the BChls within 200 fs. The rest of the S_2 population decays either into S_1 , S^* , or the CT state. However, the internal conversion to the S_1 state has been found experimentally to be also an ultra-fast process with a decay time of less than 200 fs. Since the ET process occurs within 300–400 fs and the S_2 state does not exhibit such a decay component, it is very likely that the CT state is hardly populated from the S_2 state directly. The population of the CT state from the Q_x state is also not very likely, since the BChl excited states are part of the very efficient EET mechanism away from the LH2 complex. Thus, the internal conversion to the Q_y state and the EET to other BChl molecules are expected to be much faster than the decay into the CT state [109]. The only remaining excited states which can significantly populate the CT state, are the S_1 and S^*

states of the Cars. However, both of these states exhibit two non-negligible decay channels with experimental time constants in the several picosecond range. One is the decay into the Car ground state S_0 and the other occurs via EET to the BChl Q_y state. Thus, the ET process cannot be a direct competitor of the two processes, otherwise most of the S_1 or S^* population would decay into the CT state. Yet, vibrationally excited S_1 or S^* states which exhibit vibrational relaxation times of less than 400 fs can populate the CT state to a small fraction (5%–15%), while the rest of the population decays into the vibrational ground state of S_1 or S^* and further on into Car ground state and BChl Q_y state. If the relevant vibrationally excited states of Spherone are lower in energy than the CT state, no formation of a Spherone radical cation would be observed. Our calculations show that the S_1 state of Spherone is 0.2 eV below the CT state at the ground state optimized geometry. The energy gap will be larger at the relaxed geometry of the Spherone S_1 state in which the system will be prior to electron transfer. Thus, it can be expected that few vibrational levels of the S_1 state are indeed below the ET state.

All theoretical considerations have been done based on comparison of approximate quantum chemical calculations using simplified models of LH2 complexes with experimental findings. The employed TDA/TD-DFT method yields excitation energies of the relevant states which are in acceptable agreement with experimental values, though the obtained transition amplitudes are quite unreliable. The models lack most of the influence of the protein and other surrounding molecules, since all our attempts to include this influence failed. However, based on our computations [111] a pump-deplete probe experiment can be suggested to further study the mechanism of Car radical cation formation in LH2 of purple bacteria. After pumping of the Car S_2 state and a certain delay time, the S_1 state should be depleted by a second laser pulse at the excited state absorption of the Car. Then the radical cation signature should be probed. If our mechanism is correct, the radical cation signal will be diminished when the S_1 state is depleted.

A similar experiment has already been performed previously to study excitation energy transfer pathways in LH2 [142]. Results from such experiments, together with calculations on more advanced model systems incorporating influence of the protein environment and more accurate and reliable theoretical methods for excited states calculations may lead to a deeper understanding of the processes triggering Car radical cation formation.

4.1.3 Light-Harvesting Complex 2 in Green Plants

The membrane protein LHC-II (Figure 4.8) is the major light harvesting complex in green plants. Representing about 30% of the total protein in the chloroplast membranes, it is the most abundant membrane protein on Earth [145]. The main function of LHC-II is the efficient absorption of light and the transport of the excitation energy to the reaction centers of photosystems I and II [146]. But, it also takes part in protection mechanisms in the photosynthetic system by quenching reactive intermediates like triplet states and singlet oxygen. Its participation in excess energy quenching under high-light conditions, the so-called non-photochemical quenching, is strongly debated [147–151].

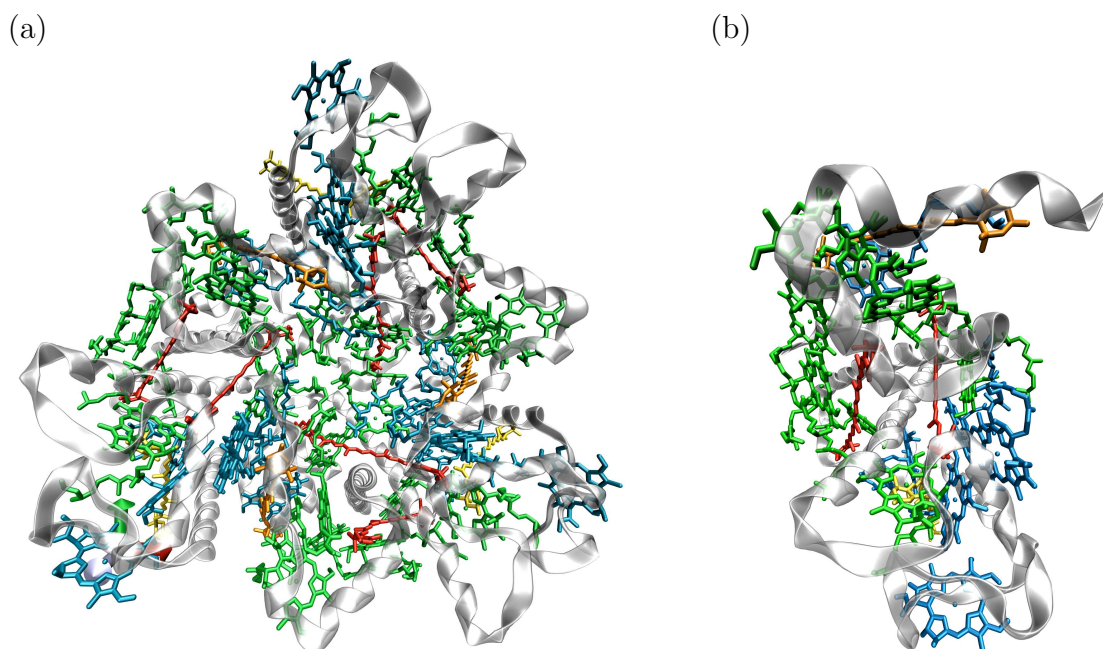


Figure 4.8: Structure of the light-harvesting complex LHC-II of green plants: (a) complete trimeric protein, (b) one monomer. Luteins are displayed in red, Violaxanthins in orange, Neoxanthins in yellow, Chl *a* in green, and Chl *b* in blue.

The structure of LHC-II has recently been determined by X-ray crystallography with an atomic resolution of 2.72 Å from spinach thylakoids [101], as well as with 2.5 Å resolution from pea leaves [102]. Both structures are very similar exhibiting a small root-mean-square deviation of the α -carbons in the polypeptide chain of

only 0.35 Å. One LHC-II complex consists of three identical subunits. Each of these monomers contains eight Chl *a*, six Chl *b* and four carotenoids being two luteins (Lut), one violaxanthin (Vio) and one neoxanthin (Neo). The knowledge about the orientation of the pigments and their direct protein environment allows for a tentative spectral assignment [152, 153] and development of kinetic models for excitation energy transfer [114, 115]. However, the role of LHC-II in NPQ could not yet be unequivocally clarified.

The only component of NPQ involved in high-energy state quenching within minutes to seconds after high-light exposure is the feedback deexcitation quenching mechanism (qE). This mechanism is regulated by the magnitude of the transmembrane pH gradient across the thylakoid membrane [149, 150]. An increase in the pH gradient activates the Vio deepoxidase which reversibly converts Vio into zeaxanthin (Zea) via the xanthophyll cycle [154]. The change in the pH gradient also protonates PsbS, a subunit of photosystem II which is necessary for qE in vivo [155], but whose exact role is still not known. The effects of the conversion from Vio to Zea during qE are highly controversial. At the moment, two different mechanisms are discussed which could explain the observed processes during qE.

The first mechanism assumes that Zea acts as direct quencher of Chl fluorescence. This scenario is supported by the so-called “molecular gear-shift” model: the lower S_1 excitation energy of Zea is supposed to allow for excitation energy transfer quenching of chlorophyll fluorescence while the higher S_1 energy of Vio allows only for light harvesting. In addition, Chl excitation energy can also be dissipated via electron transfer quenching from Chl to Zea, since the formation of carotenoid radical cations has been observed experimentally during qE [156], as theoretically predicted previously [55, 56]. Whether excitation energy transfer from Chl to Zea and dissipation into heat, or electron transfer quenching and carotenoid radical cation formation, or both at the same time, are the molecular mechanisms of qE, is still debated and topic of ongoing research. The solved structure of LHC-II [101, 102] revealed a possibility for an appealingly simple mechanism of qE. It became clear that the binding pocket of Vio lies on the surface of LHC-II and is easily accessible. This led to the hypothesis that a replacement of Vio by Zea in the LHC-II binding pocket might be possible during the induction time of qE, which could already be sufficient to invoke quenching of chlorophyll fluorescence with Zea being the direct quencher.

In the second mechanism, the conversion of the xanthophyll carotenoids has only an indirect influence leading to structural changes of the photosynthetic apparatus [157]. This has recently been substantiated by the observation that purified crystals of LHC-II are quenched and exhibit spectral signatures similar to those of the quenched state in vivo [116]. Today, this model is generally referred to as aggregation quenching. The quenching of the excess excitation energy is thought to be brought about by closely coupled chlorophyll pairs located within quenched LHC-II complexes [116, 158], or by one central lutein carotenoid in LHC-II [159]. However, a definite proof that the observed aggregation quenching in the crystals is related to in-vivo quenching is still missing.

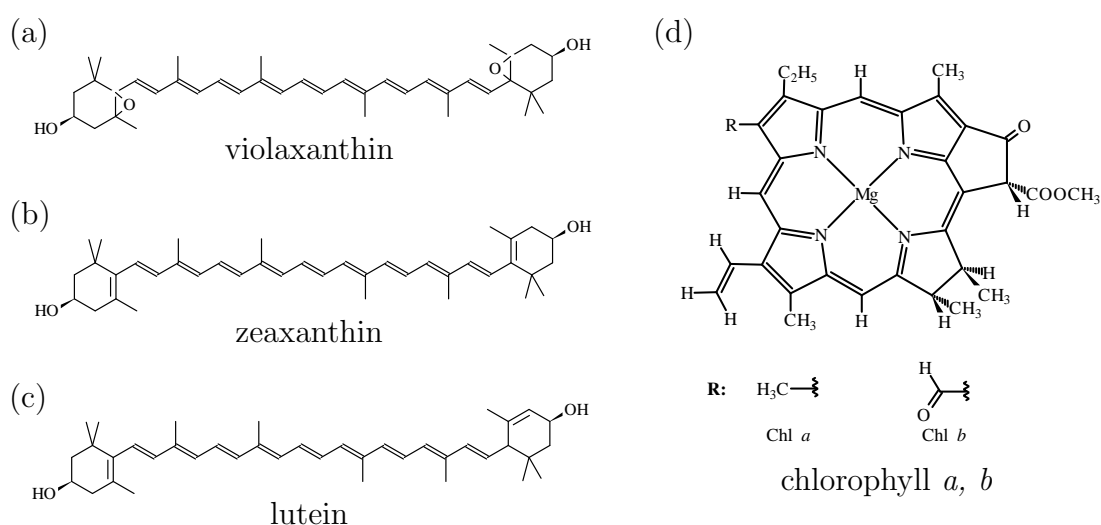


Figure 4.9: Structures of chromophores in LHC-II which may be involved in the excess energy quenching during NPQ: (a) violaxanthin, (b) zeaxanthin, (c) lutein, and (d) chlorophyll *a, b*.

Zea-Chl Quenching Complex in LHC-II

With regard to the first mechanism, it has been proposed that during qE Zea can dissipate excess energy by replacing Vio in its binding pocket in LHC-II and formation of a Zea-Chl quenching complex. In order to test this hypothesis, we have performed high-level quantum chemical calculations on model complexes for the binding pocket of violaxanthin employing the methodology described in Section 4.1.1.

Model Construction. As a first step, suitable molecular models for the quenching site have been constructed based on the crystal structure of LHC-II. For this purpose, violaxanthin, the spatially closest chlorophyll molecule Chl 9 (according to the nomenclature of Ref.[102]), and the amino acid residue Tyr24 which is coordinated to the magnesium atom of Chl 9 have been extracted from the crystal structure. Chl 9 is assigned to be a Chl *b* molecule in the crystal structure, however, the density of the identifying formyl group is not resolved and the assignment has been performed based on stoichiometric arguments only. Hence, we have performed our calculations for both possibilities that Chl 9 is either Chl *a* or *b*. Based on the Vio–Chl 9–Tyr24 model complexes, Zea–Chl 9–Tyr24 model complexes have been constructed to mimic the situation when Vio has been replaced by Zea in its binding pocket. Therefore, the epoxy oxygens in the β -ionone rings of Vio have simply been deleted. This certainly implies that the binding pocket does not largely change upon replacement of Vio by Zea, and that the same geometrical restraints are imposed on Zea as on Vio. From the construction procedure a total of four model complexes has been obtained, which all look similar to the Vio–Chl 9 *a*–Tyr24 complex depicted in Figure 4.10. All model complexes have been subjected to unconstrained geometry optimizations using DFT with the B3LYP xc-functional and the 3-21G basis set. By the optimizations, the intermolecular geometrical parameters adjusted slightly. The relative arrangement of the pigments, however, remained essentially unchanged compared to the one in the crystal structure. The optimized model complexes serve as input for the theoretical investigation of possible excitation energy quenching pathways.

Potential Energy Curves. Using the methodology outlined in Section 4.1.1 to obtain excited states of such large complexes, the lowest excited states of the model complexes have been calculated along the intermolecular distance coordinate R between Chl and Car as depicted in Figure 4.10. For the calculation of the Car and Chl excited states the Tamm-Dancoff approximation (TDA) with the BLYP xc-functional and the 3-21G basis set has been employed. The same combination of functional and basis set has been used within the TDA/CIS hybrid approach to calculate the lowest electron transfer (ET) state. While the relevant excited states of the Cars (S_1 and S_2) and of Chl 9 (Q_y and Q_x) correspond to typical $\pi - \pi^*$ excited local states, in the CT state an electron is transferred from the highest

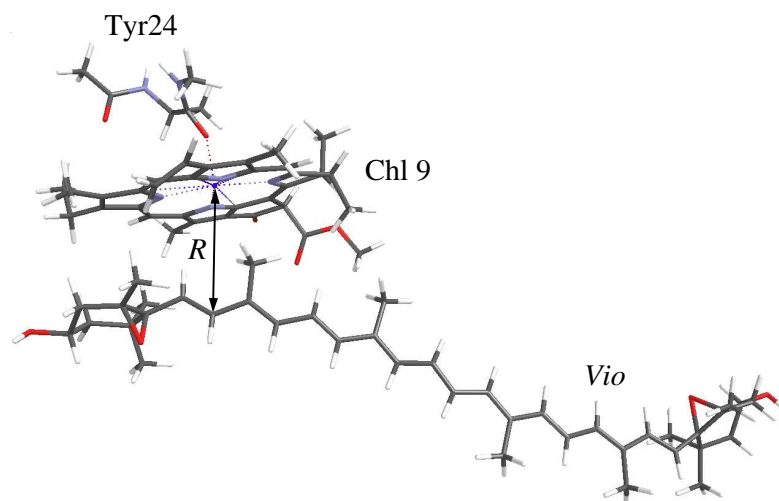


Figure 4.10: Structure of the Vio–Chl 9 *a*-Tyr24 model complex after unconstrained geometry optimization. *R* corresponds to the intermolecular distance coordinate along which the potential energy curves have been calculated.

occupied π orbital of the Car to the lowest unoccupied π orbital of Chl 9.

The computed potential energy curves of all four complexes are displayed in Figure 4.11. For the Vio–Chl 9 *a*-Tyr24 complex (a), the S_1 state of Vio is at all distances higher in energy than the Chl Q_x and Q_y states which prevents the excitation energy transfer quenching from Chl 9 to Vio. In case of the Zea–Chl 9 *a*-Tyr24 complex (b), the electronic excited states of Zea are slightly lower in energy which causes the Zea S_1 state to be located between Q_x and Q_y . However, excitation energy transfer quenching is still not possible. The CT states are in both complexes energetically far above the S_1 and Q_y states at large intermolecular distances, however they become practically degenerate with the S_1 and Q_y states at 5.0–5.2 Å in both complexes. Electron transfer quenching and the formation of a carotenoid radical cation might thus be possible in both complexes, though this can not be unambiguously decided. Taking into account the small differences in the excitation energies of the Q_x , Q_y , and S_1 states, which are below the accuracy of the applied quantum chemical methods both complexes look essentially the same in our calculations. Thus, one should not expect a different quenching behavior of Vio and Zea in the binding pocket of LHC-II. In other words, if Vio does not quench chlorophyll fluorescence, Zea should not quench either.

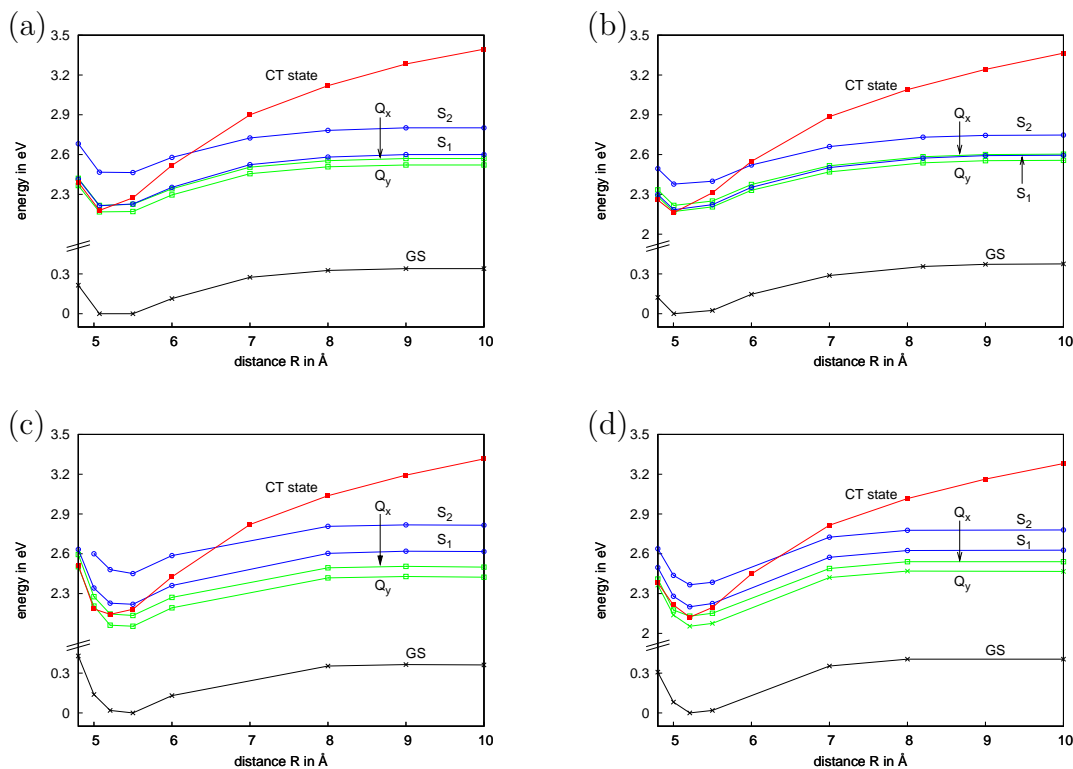


Figure 4.11: Potential energy curves of (a) Vio-Chl *a*-Tyr24, (b) Zea-Chl *a*-Tyr24, (c) Vio-Chl *b*-Tyr24, and (d) Zea-Chl *b*-Tyr24 model complexes in the binding pocket of violaxanthin in LHC-II along the intermolecular distance coordinate R (Fig. 4.10). Shown are the ground state (black line), the Chl Q_x and Q_y states (green lines), the Car S_1 and S_2 states (blue lines) and the Car \rightarrow Chl CT state.

In previous analogous calculations performed on similar model complexes [55, 56], distinct differences between Vio-Chl *a* and Zea-Chl *a* complexes have been observed. It was found that formation of such complexes can lead to efficient excitation energy quenching in the Zea-Chl *a* case, and to electron transfer quenching, i.e. carotenoid radical cation formation, in both complexes. However, these calculations were performed on model complexes obtained from free geometry optimization of the individual pigment molecules and guessing of relative orientations, since at that time no crystal structure was available. The relative orientations of Zea and Chl *a* in the previously investigated model structures are substantially different from those of the orientation in the Vio binding pocket of LHC-II. However, the previous calculations correctly predicted the occurrence of electron

transfer quenching, which was observed later by the detection of zeaxanthin radical cations during qE [156]. In contrast, the new calculations presented above demonstrate that under the constraints of the binding pocket Vio and Zea do not behave differently. The reason for this is that in the binding pocket Chl 9 is spatially very close to the β -ionone rings of the Cars. This results in a slight twist of one β -ionone ring of the Car with respect to its conjugated chain. For Vio the twist of the β -ionone ring has only a negligible influence on the electronic excited states, since the π - π^* transitions are located exclusively along the conjugated chain. For Zea, on the other hand, the double bonds in the β -ionone rings also contribute to the π -system of the conjugated chain. The twist of the ring of Zea induced by the presence of Chl 9 reduces the overlap between the ring double bond and the conjugated chain and thus reduces the effective conjugation length of Zea. Accordingly, the excitation energies of the π - π^* transitions of Zea in the twisted conformation are only slightly different from those of Vio.

Up to now, only complexes containing Chl *a* have been considered. Yet, according to the assignment in the crystal structure Chl 9 is most probably a Chl *b* molecule. Thus, let us now examine the differences arising on replacement of Chl *a* by Chl *b* in the Car–Chl 9–Tyr24 complexes. As already mentioned above there are only minor structural differences between the various complexes after unconstrained geometry optimization at DFT/B3LYP/3-21G level of theory. The calculation of the electronic excited states of the Vio–Chl 9 *b*–Tyr24 (c) and Zea–Chl 9 *b*–Tyr24 (d) complexes using TD-DFT introduces additional difficulties, which are due to the additional carbonyl group of Chl *b*. The carbonyl group leads to artificially low-lying intramolecular CT states that mix with the Q_x and Q_y states in the TD-DFT calculations. These admixtures lead to lower excitation energies of the Chl *b* excited states compared to those of Chl *a* which is in contradiction to the experimental findings.

Figures 4.11 (b) and (d) show the potential energy curves of the Zea–Chl *a*–Tyr24 and Zea–Chl *b*–Tyr24 model complexes. The energetically lower Chl excited states of Zea–Chl *b* are obvious from both figures. We also observe a slight decrease in the energy of the CT state in Fig. 4.11 (c) of about 0.1 eV which is caused by the larger electron affinity of Chl *b* compared to Chl *a*. The lower excitation energy of the CT state in the Zea–Chl *b*–Tyr24 complex leads to an increase of the intermolecular distance by approx. 0.5 Å at which the crossings between

the CT state and the other states occur. The differences between the potential energy curves of the corresponding model complexes containing Vio are practically identical to the ones shown for the different Zea complexes. As a consequence, the model complexes Vio–Chl *b*–Tyr24 and Zea–Chl *b*–Tyr24 exhibit the same similarity as the Chl *a* containing complexes.

Interpreting these theoretical findings one can conclude that conversion of Vio to Zea in the Vio binding pocket of LHC-II does not change the excitation energy and electron transfer processes between Car and Chl significantly, no matter whether Chl 9 is a Chl *a* or Chl *b* molecule. In other words, since Vio does not quench chlorophyll fluorescence, the replacement of Vio by Zea at its binding site does not induce excitation energy quenching. However, due to the underlying approximations and the limited accuracy of the employed quantum chemical methodology, as well as due to the employed approximate molecular model, we can not unambiguously draw this conclusion based on our calculations alone. However, recently, elaborate femtosecond pump-probe experiments have been performed on purified LHC-II complexes containing Vio or Zea in the Vio binding pocket [110]. It was shown that upon optical excitation of the Q_y state of Chl *a*, no difference in the chlorophyll fluorescence lifetime could be observed for these two samples, indicating that it is not quenched by Zea in the binding pocket of LHC-II. Moreover, also a carotenoid radical cation signal could not be observed as trace of electron transfer quenching. This is in agreement with our calculations and excludes the Vio binding pocket of LHC-II as quenching site of the high-energy state quenching component of NPQ.

Lutein as Site for Aggregation Quenching

Concerning the aggregation quenching mechanism, it has recently been suggested based on elaborate resonance Raman and transient absorption spectroscopy that one of the central lutein (Lut) molecules might act as terminal quencher [159]. The excess energy is then transferred from a nearby Chl molecule to Lut which eventually dissipates it as heat. It is assumed that LHC-II complexes can switch from an unquenched state under normal light conditions into a quenched state triggered by intense light. Both states are supposed to differ by subtle conformational changes only. Furthermore, the known crystal structures presumably display the

latter quenched state of LHC-II. The molecular structure of LHC-II monomers exhibits pseudo- C_2 symmetry (Figure 4.8 (b)). The two central lutein molecules Lut 1 and Lut 2 are in close contact with Chl 2 and Chl 5, respectively. Both Chl *a* molecules form strongly coupled Chl dimers with spatially very close lying Chls. Chl 7 is the Chl *a* molecule which is close to Chl 2, while the Chl *b* molecule Chl 12 is the one close to Chl 5. Due to the different coupling partners and the distinct protein environment, the structures of Lut 1 and Lut 2 deviate slightly, as well as the relative spatial arrangement between Lut 1 and Chl 2 differs slightly from the one between Lut 2 and Chl 5 (Figure 4.12).

From this, the questions arise whether the luteins can act as quencher in LHC-II and whether the different structures and relative orientations of the luteins have a significant influence on the excited states of the pigments and thus on the electron and excitation energy transfer capabilities. We have addressed these questions by means of quantum chemical calculations of the excited states of molecular model complexes following the same methodology as in case of the Zea-Chl quenching complex (see also Section 4.1.1).

Model Construction. For the construction of suitable model complexes, the Lut molecules have been extracted from the LHC-II crystal structure, together with the corresponding neighboring Chl molecules, and the amino acid to which the Mg atom of the respective Chl is coordinated. Unfortunately, it is not possible to also include Chl 7 and Chl 12 into the calculations due to the enormous size of those complexes. This gives rise to the two model complexes shown in (Figure 4.12): Lut 1–Chl 2–Asn 183 and Lut 2–Chl 5–His 68. Constrained geometry optimizations have been performed on both complexes which kept the relative orientations of the pigments fixed, while the intermolecular geometrical parameters were left to relax. The optimized model complexes are subjected to excited state calculations as described in the previous section.

Potential Energy Curves. The calculation of the excited states of the Lut 1–Chl 2 complex along the distance coordinate defined in Figure 4.12 revealed that in the geometrical arrangement of the Lut binding site, Lut 1 has a slightly lower S_1 excitation energy than the Q_y state of Chl 2. Thus, excitation energy transfer from Chl 2 to Lut 1 is possible, in principle. However, these states are practi-

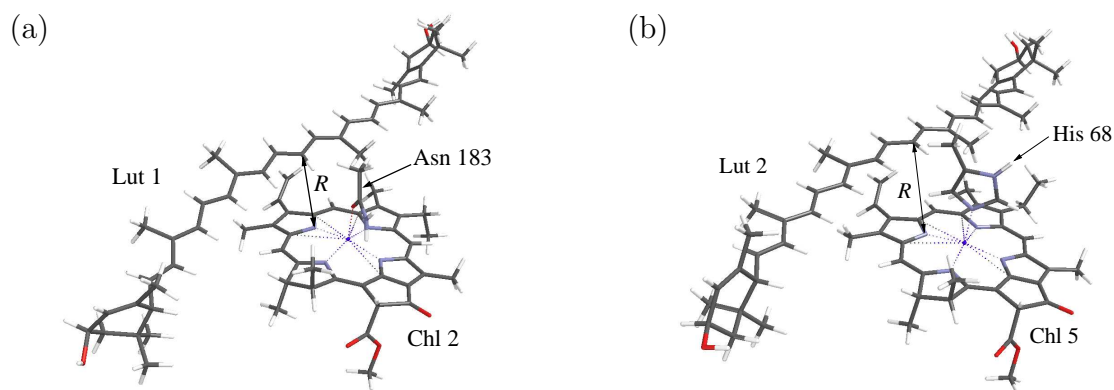


Figure 4.12: Structures of the (a) Lut 1–Chl 2 *a*-Asn 183 and (b) Lut 2–Chl 5 *a*-His 68 model complexes resembling the relative orientations of the pigments in the Lut 1 and Lut 2 binding sites of LHC-II. R defines the distance coordinate for our computations.

cally degenerate and a definite conclusion about the relative energetic position of these states and a clear-cut statement about EET processes are certainly beyond the accuracy of our theoretical methodology. In particular, when the effect of the missing, strongly coupled Chl 7 is taken into account, one can expect that the excitation energy of the Chl 2 states further decreases due to excitonic coupling. Thus, it is very likely that the Q_y state actually lies below the S_1 state of Lut 1. The same holds for the charge-transfer excited state. As is visible in Figure 4.13 (a), the CT state drops slightly below the S_1 and Q_y states at an intermolecular separation of 4 Å, which is approximately the Lut 1–Chl 2 distance in the crystal structure. This suggests that electron transfer quenching may be possible for Lut 1 by transferring an electron to Chl 2. However, for the reasons above, a final definite conclusion is not possible based on our results alone.

Regarding Lut 2, Figure 4.13 (b) clearly shows that electron transfer quenching is not possible in the Lut 2–Chl 5 complex, since the CT state stays above all valence excited states over the whole distance range. This certainly results from the slightly worse overlap of the π -systems of Lut 2 and Chl 5 compared to the Lut 1–Chl 2 complex. The S_1 state of Lut 2 is energetically slightly above the Q_y state of Chl 5. Thus, the excitation energy transfer quenching probably will not occur within this pigment pair. However, the energy difference of the two states is tiny at the theoretical level employed, which makes a conclusive statement impossible.

Again, one may speculate that the inclusion of Chl 12 in the calculation would result in a decreased excitation energy of the Q_y state making EET quenching even more unlikely.

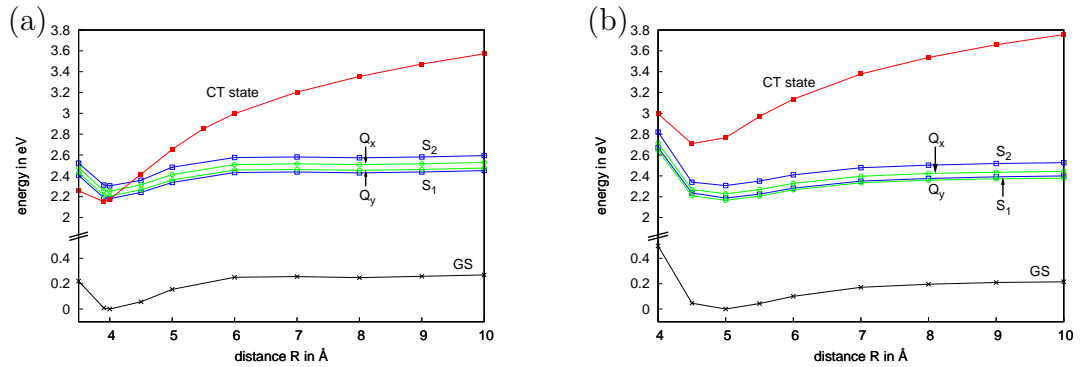


Figure 4.13: Potential energy curves of (a) Lut 1–Chl 2–Asn 183, and (b) Lut 2–Chl 5–His 68 model complexes in the orientation of the lutein binding sites of LHC-II along the intermolecular separation coordinates R (see Fig. 4.12). Shown are the ground state (black line), the Chl Q_x and Q_y states (green lines), the Car S_1 and S_2 states (blue lines) and the Car→Chl CT state.

The almost identical vertical excitation energies of the valence excited states in the Lut 1–Chl 2 and Lut 2–Chl 5 are certainly not surprising, since there are only subtle structural differences between the two complexes. On the contrary, it is striking that the CT state responsible for ET quenching is strongly affected, and that only Lut 1 can probably quench via ET quenching. The accuracy of the theoretical methodology is not sufficient to draw definite conclusions whether the lutein molecules in LHC-II can quench excess excitation energy or not, or in other words, whether the lutein molecules can be the terminal quencher during qE. Yet, we can conclude that if at all then Lut 1 is the quencher.

4.2 Calculations on Model Systems using ADC

In the previous sections, studies of excitation energy and electron transfer processes in light-harvesting complexes have been described, in which TD-DFT and CIS have been combined to calculate the relevant excited states of model complexes. Though certain conclusions could be drawn from the calculations by comparison with experimental data, the interpretation of the computational results is limited by the restrictions in the size of the molecular models and the accuracy of the employed quantum chemical methods. As already described previously (see e.g. Section 4.1.1), the excitation energies of the lowest excited states obtained with TD-DFT are in acceptable agreement with experiments. However, TD-DFT does not account for double excitations. This renders the description of the lowest excited state of carotenoids questionable, since this state is known to have strong doubly excited character. Whether the agreement of the excitation energies with experimental data also extends to other properties of the excited states, like equilibrium geometries and transition amplitudes, remains unclear. Additionally, the application of TD-DFT suffers from its rather unreliable transition amplitudes, and the charge-transfer problem. The latter has indeed been circumvented by means of the Δ DFT approach described in Section 3.2.3, but it still hampers the calculation and assignment of valence excited states (see Section 4.1.2 and 4.1.3). To obtain improved computational results more sophisticated quantum chemical methods could in principle be employed. Yet, such methods are, in general, not applicable to the model systems described above.

To work towards the improved theoretical description of the model systems, we have turned to the algebraic diagrammatic construction scheme (see Section 3.3). Its second order variants [71], ADC(2)-s and ADC(2)-x, are among the cheapest higher-order excited states methods [74], and can correctly describe Rydberg and charge-transfer states. Double excitations are also included by both methods though to different order in perturbation theory. Hence, comparison of ADC(2)-s and ADC(2)-x results can yield information on the importance of double excitations for the excited states in consideration. As a first step, we have evaluated the performance of ADC(2)-s and ADC(2)-x compared to TD-DFT and experimental data on linear all-*trans* polyenes [61].

4.2.1 Linear Polyenes

Linear all-*trans* polyenes play important roles in biological photoprocesses and technical applications. They also serve as model systems for carotenoids whose lowest excited states are of utmost importance in EET and ET processes in LHCs. Thus, many theoretical and experimental studies of the lowest excited states of linear polyenes have been performed since the early 1970's [54, 160–170].

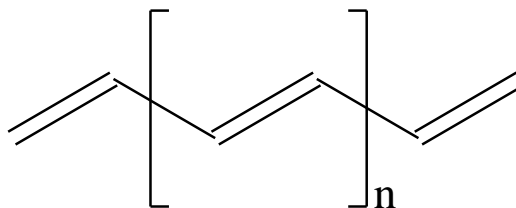


Figure 4.14: Structure of polyenes.

The excited states of all-*trans* polyenes are usually characterized by the irreducible representations of their molecular C_{2h} symmetry, i.e. A_g , B_g , A_u , and B_u . An additional index, “-” or “+” [171], specifies the anti-symmetric or symmetric linear combination of degenerate configurations, respectively. The ground state is classified as $1^1A_g^-$. The lowest excited state (S_1) has been found to be the $2^1A_g^-$ state which is optically forbidden, since it exhibits the same spatial symmetry as the ground state. Though the state cannot be measured by conventional optical spectroscopy directly, it was still observed first by high-resolution fluorescence spectroscopy experiments [160]. As the second lowest excited state (S_2) the optically allowed $1^1B_u^+$ state has been identified. Theoretically, the proper description of the low-lying excited states of linear polyenes is challenging, since in general at least doubly excited configurations have to be included in the calculations to obtain the right ordering of states. The computational effort of the respective methods is already quite large, so that the calculations of longer polyenes or carotenoids are hardly feasible. Still, several theoretical studies using semi-empirical multi-reference CI [162, 163, 172], multi-reference MP [173, 174], complete active space perturbation theory of second order [168, 169], and TD-DFT/TDA [54] have found the lowest excited state of linear polyenes to be the $2^1A_g^-$ state. It is particularly surprising that TDA using the BLYP functional is among these methods, since it

does not account for any doubly excited configurations which have been found to be important for the description of the $2^1A_g^-$ state by the other methods. Yet, the $2^1A_g^-$ state and the $1^1B_u^+$ state obtained with TDA are in reasonable agreement with experiments, the $2^1A_g^-$ state being described by a linear combination of HOMO \rightarrow LUMO+1 and HOMO-1 \rightarrow LUMO transitions. The question arises why TD-DFT yields reasonable excitation energies of the dark $2^1A_g^-$ state without considering double excitations.

In the study [61] we have investigated the three lowest excited states $2^1A_g^-$, $1^1B_u^+$, and $1^1B_u^-$ of linear polyenes from butadiene (C_4H_6) to tetradecaheptaene ($C_{14}H_{16}$). Excitation energies of each polyene have been calculated using ADC(2)-s, ADC(2)-x, TDA/BLYP, and TD-DFT/BLYP. The ADC calculations have been performed using the 6-31G basis set, whereas the TD-DFT and TDA results have been obtained with the 6-31G* basis set. Still, the calculation of $C_{14}H_{16}$ has not been feasible with ADC(2)-x and the 6-31G basis set. All excited states calculations have been performed at the ground state equilibrium geometries resulting from MP2 ground state optimizations with 6-31G* basis set. For the calculations a development version of Q-Chem 3.0 [77] and the original ADC program [175] of the theoretical chemistry group in Heidelberg have been employed.

Curves of the calculated excitation energies of the three lowest states are displayed in Figure 4.15 as function on the number of C=C double bonds. For comparison also experimental values from [176–180] are shown (black curves). All curves exhibit the expected decrease in excitation energy towards longer polyenes. For the dipole (one-photon) allowed $1^1B_u^+$ state, the ADC(2)-s and ADC(2)-x results differ only slightly, the ADC(2)-x curve being less than 0.5 eV lower in energy. The ADC(2)-s excitation energies are already in relatively good agreement with experimental values. The error is 1 eV in case of butadiene and as small as 0.4 eV for tetradecaheptaene, with the basis set error being approximately 0.5 eV. The ADC(2)-x excitation energies deviate even less. The TD-DFT and TDA values also exhibit only small deviations of less than 0.7 eV from the experimental data. However, the errors of the TD-DFT excitation energies increase with increasing chain length of the polyenes, as do the TDA values starting from decapentaene. This is in contrast to the ADC data where the errors in the excitation energies decrease for longer polyenes. Still, all four methods describe the $1^1B_u^+$ state as consisting mainly of the HOMO \rightarrow LUMO transition.

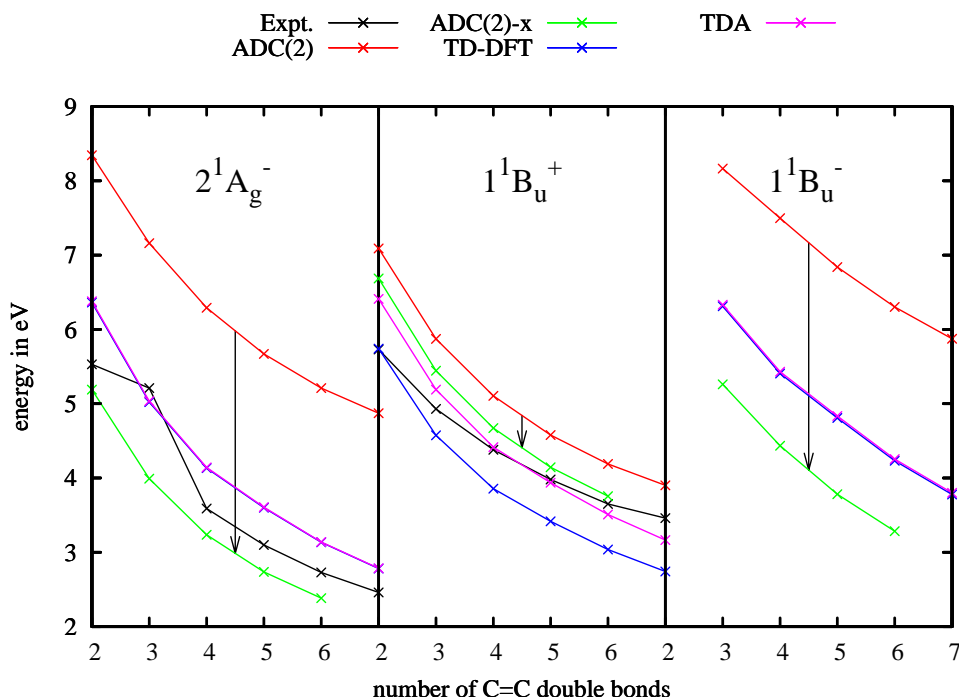


Figure 4.15: Excitation energies of the three lowest excited states of linear all-*trans* polyenes depending on the number of C=C double bonds. Shown are three graphs, one for each excited state (left: $2^1A_g^-$; middle: $1^1B_u^-$; right: $1^1B_u^+$). In each graph experimental values (black lines), and values calculated with ADC(2)-s (red lines), ADC(2)-x (green lines), TD-DFT (blue lines), and TDA (pink lines) are given.

The situation is totally different in case of the $2^1A_g^-$ and $1^1B_u^-$ states. As indicated by the black arrows, the vertical excitation energies of both states drop drastically when going from ADC(2)-s to ADC(2)-x. On the other hand, the TD-DFT values of both states are almost identical to the respective TDA values. Compared to experimental data, the errors of the calculated excitation energies of the $2^1A_g^-$ state decrease with increasing length of the polyenes for all methods. The ADC(2)-s energies exhibit errors of up to 3 eV, while ADC(2)-x underestimates the excitation energies by less than 0.4 eV. The values obtained with the two TD-DFT methods are larger in energy than the experimental data, showing errors of 0.8 eV and 0.3 eV for butadiene and tetradecaheptaene, respectively. Interestingly, ADC(2)-s, as well as TD-DFT and TDA describe the $2^1A_g^-$ state essentially as combination of the HOMO \rightarrow LUMO-1 and HOMO-1 \rightarrow LUMO single excitations.

At ADC(2)-x level the state possesses mainly doubly excited HOMO²→LUMO² character which is in accordance to previous high-level calculations [163]. Similarly, the $1^1B_u^-$ state consists to a large extent of the HOMO-2→LUMO single excitation in case of ADC(2)-s, TD-DFT, and TDA, while at ADC(2)-x level its strongest contribution arises from a HOMO,HOMO-1→LUMO² double excitation.

Considering the ordering of the excited states as they are obtained with the four methods, ADC(2)-s and TD-DFT/BLYP see the optically allowed $1^1B_u^+$ state as lowest excited state, while at the ADC(2)-x and TDA/BLYP level the $2^1A_g^-$ state is lower in energy. Compared to experiments the ADC(2)-s and TD-DFT calculations yield the wrong ordering of states, since experimentally the lowest excited state of linear polyenes is optically forbidden. The orderings obtained by ADC(2)-x and TDA are $2^1A_g^-$, $1^1B_u^-$, $1^1B_u^+$ and $2^1A_g^-$, $1^1B_u^+$, $1^1B_u^-$, respectively. Both orderings agree with experimental data, since it could not yet be unequivocally determined whether the $1^1B_u^+$ state or the $1^1B_u^-$ state is lower in energy. Still, the fact that the wave function of the $2^1A_g^-$ state at TDA level resembles more closely the one at ADC(2)-s and TD-DFT level than the one obtained by ADC(2)-x suggests that this state is not correctly described by TDA/BLYP.

A possible reason for the well reproduced excitation energies of the lowest excited states of longer polyenes, and for the decreasing error with increasing chain length at TD-DFT and TDA level can be found by analysis of the importance of doubly excited configurations in ground and excited states. As described in [61] the electronic ground states of larger linear polyenes become strongly correlated, so that doubly excited configurations become more and more important for their description. Ground state DFT accounts for the electron correlation to some extend by means of the xc functional. However, for strongly correlated systems it is known that this is not sufficient. As result, the errors in the ground states obtained by DFT calculations become larger for longer polyenes due to the neglect of doubly excited configurations. Similar to the ground states also the $2^1A_g^-$ and $1^1B_u^-$ states gather more double excitation character when going to longer polyenes, while the amount of doubly excited configurations contributing to the $1^1B_u^+$ states stays almost constant at 10%. The description of the $2^1A_g^-$ and $1^1B_u^-$ states by TD-DFT can thus be expected to show a similar increase in error as the ground state description by DFT. Since the importance of doubly excited configurations grows faster for the ground state than for the excited states, the errors in ground

states and excited states will most likely match at some point. This can explain why the error in the $2^1A_g^-$ excitation energies at the TDA level decreases with increasing chain length. In contrast, the quality of the description of the $1^1B_u^+$ state is almost independent of the number of double bonds. The excitation energies then suffer from the increasing errors in the ground state description, so that the errors of the $1^1B_u^+$ states increase with increasing size of the polyene.

In summary, the calculations show that treatment of linear polyenes with ADC(2)-s is only sufficient for the calculation of the optically allowed $1^1B_u^+$ state. For the description of the $2^1A_g^-$ and $1^1B_u^-$ states ADC(2)-x or even higher methods have to be employed. The respective vertical excitation energies resulting from ADC(2)-x calculations are underestimates by less than 0.4 eV. The good performance of the TD-DFT methods with respect to the $2^1A_g^-$ and $1^1B_u^-$ states is due to fortuitous cancellation of errors in the ground state description compared to the description of the excited states. Thus, it is questionable whether the properties of these states calculated with TD-DFT/TDA will also benefit from this error cancellation.

4.2.2 Model Systems for Local ADC

The evaluation of the second order ADC schemes showed that especially ADC(2)-x is well suited to correctly describe the lowest excited states of linear polyenes, and most likely also of carotenoids. Yet, the application of conventional ADC(2)-s and ADC(2)-x algorithms to carotenoids, let alone to model systems for light-harvesting complexes is not feasible with present-day computers due to the computational requirements of ADC being much larger than those of TD-DFT and CIS. Thus, we have started implementing a more efficient version of ADC(2)-s and ADC(2)-x. The Davidson algorithm has been employed for the diagonalization of the ADC matrix (Section 3.3.2). Furthermore, the ADC equations have been transformed into a local orbital basis (Section 3.3.3). By exploiting the locality of the orbitals, the size of integrals and excited state vectors, as well as the computation time of matrix-vector products can be reduced. For this objective, a bumping scheme has to be employed as described in Section 3.3.3. The bumping scheme introduces several adjustable parameters in the calculation which influence the quality of the results and the reduction in computation time and disk space requirements. These parameters have to be evaluated to find the best compromise between the accuracy of results and the acceleration of computations. Since reasonable evaluation is only possible with few parameters at a time, we have started with a minimal bumping scheme having only a small number of parameters. This bumping scheme has been restricted to the bumping of doubly excited configurations in the ADC vectors, since they are among the largest data objects in an ADC calculation. It comprises a total of three adjustable parameters. The first parameter is given by the choice of the actual bumping model which is applied to the doubly excited configurations. Four different bumping models have been implemented (see Section 3.3.3). For each bumping model a bump function is necessary which has been chosen as a simple step function. The single distance parameter inherent in the step function represents the second parameter of the bumping scheme. A third parameter is required due to details in the implementation. This parameter determines the block sizes in the tensor block structure to efficiently apply the bumping models. It is given as the number of blocks in which occupied orbitals are split. Virtual orbitals are separated into twice this number of blocks. This means the parameter is molecule dependent, and its evaluation

on a test system will not result in an optimal parameter value for all possible molecules. Thus, we have only fixed the value of the parameter for each molecule, so that a block of occupied orbitals consists of four to ten orbitals. In the future, the minimal bumping scheme will be extended by successively including more and more parameters.

The evaluation of the parameters for the minimal bumping scheme is first performed on a single test molecule. Afterwards, the resulting set of optimal parameter values is applied to a larger set of test molecules.

Evaluation of Bumping Parameters

For the evaluation of the parameters in the minimal bumping scheme, ADC(2)-s and ADC(2)-x calculations have been performed on octatetraene (C_8H_{10}) using the 6-31G(d) basis set. Octatetraene has been chosen as test molecule, since being a linear polyene the calculation of its excited states is most challenging for theoretical methods (see e.g. the previous section). Additionally, it is small enough to allow for the calculation of excited states using both, conventional and local ADC without requiring too much computation time. The employed geometrical parameters of C_8H_{10} are compiled in Appendix B. The number of blocks in which occupied and virtual orbitals are separated has been set to six, so that on average five occupied orbitals and nine virtual orbitals comprise one block, respectively.

To determine the optimal bumping model for the doubly excited configurations we have performed calculations for each bumping model at ADC(2)-s and ADC(2)-x level using bumping distances of $x = 1.0 \text{ \AA}$, $x = 2.0 \text{ \AA}$, $x = 3.0 \text{ \AA}$, and $x = 4.0 \text{ \AA}$. The results of the ADC(2)-s calculations are compiled in Table 4.2. From the data it is obvious that the four bumping models largely differ in the amount of doubly excited configurations which are neglected using the given bumping distances. With bumping model 1 the amount of neglected doubly excited configurations varies between 1.86% at $x = 4.0 \text{ \AA}$ and 11.08% at $x = 1.0 \text{ \AA}$. Bumping model 2 already neglects 14.27% of the doubly excited configurations at $x = 4.0 \text{ \AA}$, and as much as 65.65% at $x = 1.0 \text{ \AA}$. No doubly excited configurations are neglected when using the bumping models 3 and 4 with bumping distances larger than or equal to 3.0 \AA . At smaller bumping distances the amount of neglected doubly excited configurations becomes 10.04% and 40.56% for bumping model 3 and 0.12%

Table 4.2: Excitation energies and oscillator strength (in brackets) of the four lowest excited states of octatetraene calculated with ADC(2) employing the 6-31G(d) basis set and local orbitals. As reference the results of standard ADC(2)-s calculations are given. For each bumping model the calculations have been performed using the values 1.0 Å, 2.0 Å, 3.0 Å, and 4.0 Å as bumping distance x . The amount of neglected doubly excited configurations is given in the last column. All excitation energies are specified in eV.

	Ex. State 1	Ex. State 2	Ex. State 3	Ex. State 4	Neglected Doubles
reference	5.05 (1.9131)	6.40 (0.0000)	7.16 (0.0000)	7.55 (0.0014)	
Bumping Model 1					
$x = 1.0$ Å	5.08 (1.9244)	6.48 (0.0000)	7.18 (0.0000)	7.59 (0.0019)	11.08%
$x = 2.0$ Å	5.08 (1.9221)	6.46 (0.0000)	7.17 (0.0000)	7.58 (0.0018)	6.66%
$x = 3.0$ Å	5.05 (1.9134)	6.41 (0.0000)	7.16 (0.0000)	– (–)	4.86%
$x = 4.0$ Å	5.05 (1.9133)	6.41 (0.0000)	7.16 (0.0000)	7.55 (0.0015)	1.86%
Bumping Model 2					
$x = 1.0$ Å	5.80 (2.1527)	7.45 (0.0015)	8.11 (0.0019)	8.20 (0.0002)	65.65%
$x = 2.0$ Å	5.65 (2.1066)	7.34 (0.0000)	7.90 (0.0000)	7.95 (0.0001)	49.50%
$x = 3.0$ Å	5.20 (1.9704)	6.77 (0.0000)	7.20 (0.0000)	7.82 (0.0001)	24.87%
$x = 4.0$ Å	5.17 (1.9600)	6.71 (0.0000)	7.19 (0.0000)	7.60 (0.0053)	14.27%
Bumping Model 3					
$x = 1.0$ Å	5.28 (1.9989)	6.96 (0.0053)	7.31 (0.0000)	– (–)	40.56%
$x = 2.0$ Å	5.12 (1.9463)	6.59 (0.0000)	7.22 (0.0000)	7.60 (0.0013)	10.04%
$x = 3.0$ Å	5.05 (1.9129)	6.40 (0.0000)	7.16 (0.0000)	– (–)	0.00%
$x = 4.0$ Å	5.05 (1.9129)	6.40 (0.0000)	7.16 (0.0000)	7.55 (0.0015)	0.00%
Bumping Model 4					
$x = 1.0$ Å	5.11 (1.9279)	6.57 (0.0133)	7.18 (0.0001)	7.59 (0.0051)	5.94%
$x = 2.0$ Å	5.05 (1.9129)	6.40 (0.0000)	7.16 (0.0000)	7.55 (0.0014)	0.12%
$x = 3.0$ Å	5.05 (1.9129)	6.40 (0.0000)	7.16 (0.0000)	– (–)	0.00%
$x = 4.0$ Å	5.05 (1.9128)	6.40 (0.0000)	7.16 (0.0000)	7.55 (0.0014)	0.00%

and 5.94% for bumping model 4. Despite the large differences in the bumping models it is still possible to evaluate them by considering the deviation of the vertical excitation energy from the reference values with respect to the amount of neglected doubly excited configurations. Bumping model 1 exhibits a maximum deviation of 0.07 eV with 11.08% of doubly excited configurations neglected ($x = 1.0$ Å). The maximum deviations of the other bumping models obtained with similar amounts of neglected doubly excited configurations are 0.31 eV for bumping model 2 (14.27%, $x = 4.0$ Å), 0.18 eV for bumping model 3 (10.04%, $x = 1.0$ Å) and 0.17 eV for bumping model 4 (5.94%, $x = 1.0$ Å). Since bumping models 2, 3 and 4 show much larger maximum deviations with similar amounts of neglected double excitations, these bumping models can be abandoned, and bumping model 1

will be used in all subsequent calculations.

The decision to use bumping model 1 has been done based on the results of the ADC(2)-s calculations alone. Examining the ADC(2)-x calculations (data not shown) a similar picture is found. Here, the maximum deviations of the vertical excitation energies are by about 0.05 eV lower for bumping models 1 and 2 compared to the respective ADC(2)-s results, while the maximum deviations increase for bumping model 3 and 4 when using ADC(2)-x. This suggests that the doubly excited configurations neglected by bumping model 3 and 4 are quite important for excited states with double excitation character, while those neglected by bumping model 1 do not play a major role. Bumping model 2 probably neglects too much of the doubly excited configurations which are already important at ADC(2)-s level.

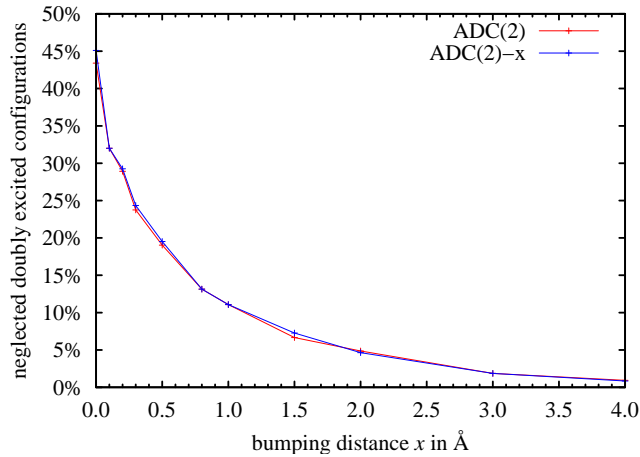


Figure 4.16: The amount of neglected doubly excited configuration as function of the bumping distance x . The ADC(2) results are given in red, the ADC(2)-x results in blue.

After choosing the bumping model, the optimal bumping distance for this model has to be determined. Therefore, the requirements on the accuracy of the calculated excited states have to be specified. In order to obtain valuable results from local ADC calculations, the deviation of the calculated excitation energies from experimental data should not be dominated by the error introduced by the local approximation. Thus, we require the maximum deviation of the excitation energies obtained with local ADC using bumping model 1 from those obtained

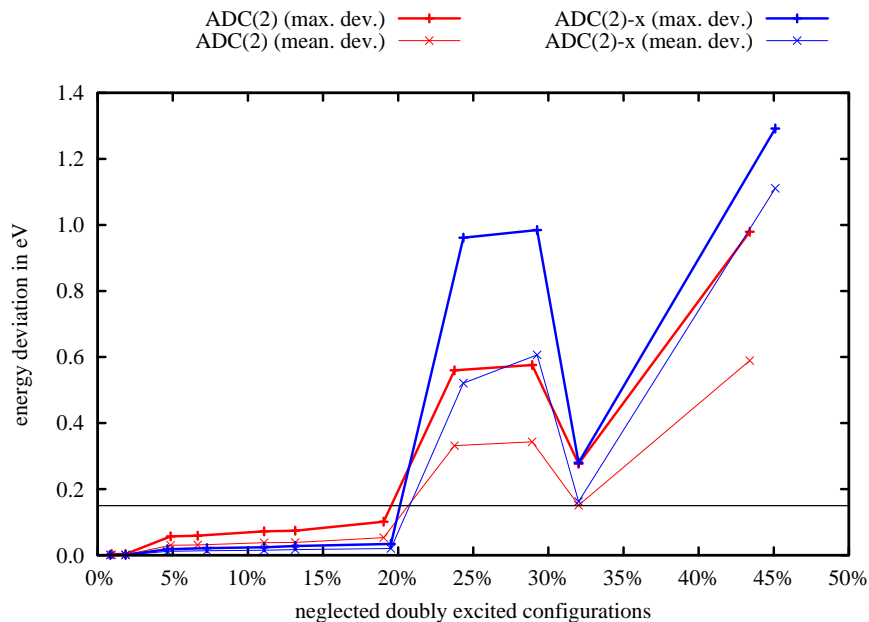


Figure 4.17: Maximum deviation (thick lines) and mean deviation (thin lines) of the excitation energies of the four lowest excited states obtained with local ADC using bumping model 1 from the results of standard ADC as function of the amount of neglected doubly excited configurations. The ADC(2)-s values are given in red, those from ADC(2)-x in blue. The black horizontal line at 0.15 eV indicates the required accuracy of the local ADC method.

with conventional ADC to be no more than 0.10 eV to 0.15 eV. On the basis of this condition ADC(2)-s and ADC(2)-x calculations can be performed using bumping model 1 and various bumping distances x to find the bumping distance with the largest amount of neglected doubly excited configurations which yields maximum deviations for the four lowest vertical excitation energies of less than 0.15 eV. The maximum deviations of the excitation energies with respect to the amount of neglected doubly excited configurations are displayed in Figure 4.17. The graphs show clearly that up to 20% of doubly excited configurations can be neglected without that the maximum deviations of the excitation energies exceed the value 0.15 eV, which is indicated by the thin black line. In this regime the deviations resulting from ADC(2)-x calculations are smaller than those resulting from ADC(2)-s. If more than 20% of doubly excited configurations are neglected, the maximum deviations of the excitation energies become larger than 0.5 eV

and 0.9 eV in case of ADC(2)-s and ADC(2)-x, respectively. The only exception is the bumping distance x at which 32% of the doubly excited configurations are neglected. At this point the curves in Figure 4.17 exhibit a kink, assuming maximum deviations in the excitation energies of about 0.3 eV. The exact reason for this kink could not yet be determined, though it is most likely due to error cancellation caused by the neglect of additional doubly excited configurations. From the analysis of Figure 4.17 it becomes evident that the best choice of the bumping distance x is the bumping distance by which $\sim 20\%$ of doubly excited configurations are neglected. The corresponding bumping distance can easily be read off Figure 4.16. There, the amount of neglected doubly excited configurations is displayed as function of the bumping distance x . The sought-after bumping distance is $x = 0.5 \text{ \AA}$, while the kink in the curves of Figure 4.17 occurs for the bumping distance $x = 0.1 \text{ \AA}$.

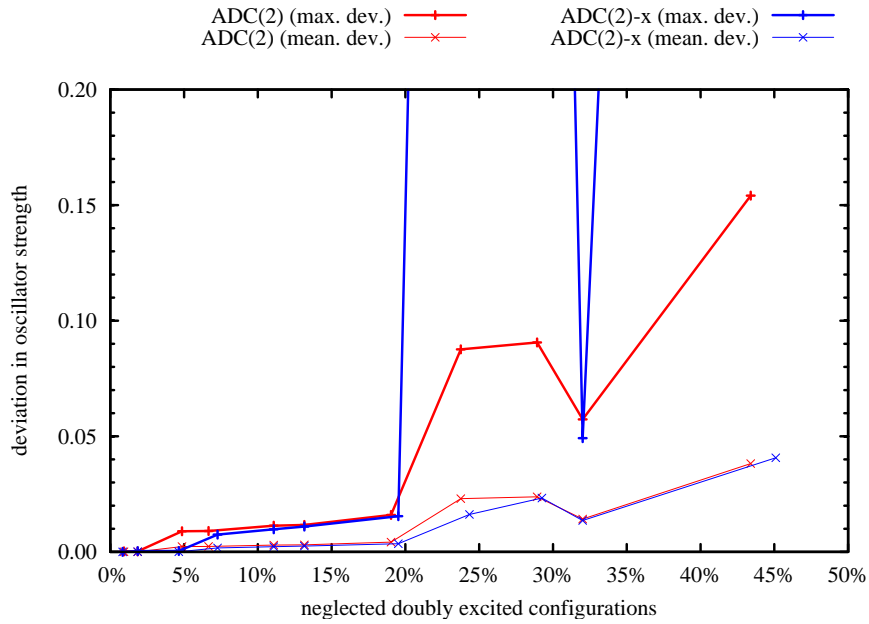


Figure 4.18: Maximum deviation (thick lines) and mean deviation (thin lines) in the oscillator strengths the four lowest excited states obtained with local ADC using bumping model 1 from the results of standard ADC as function of the amount of neglected doubly excited configurations. The ADC(2)-s values are given in red, those from ADC(2)-x in blue.

A similar picture as for the deviations of the excitation energies is found for the

deviations of the oscillator strengths (Figure 4.18). Here, the maximum deviations stay below 0.02 up to 20% of neglected doubly excited configurations and increase for larger amounts of disregarded doubly excited configurations to values of more than 0.08 for ADC(2)-s and more than 0.8 for ADC(2)-x. Also, the kink at 32% of neglected doubly excited configurations is present. The much smaller mean deviation which is especially striking in case of the ADC(2)-x results indicates that errors in the oscillator strengths compensate each other when the mean is taken. A closer look at the data reveals that indeed the deviation in oscillator strength of the lowest excited state becomes positive while the one of the second lowest excited state becomes negative. This means with increasing amount of disregarded doubly excited configurations the dipole forbidden $2^1A_g^-$ state gathers more and more oscillator strength while the optically allowed $1^1B_u^+$ state loses the same amount of oscillator strength. As result the ADC(2)-x results approach the situation with ADC(2)-s where the lowest excited state is optically allowed.

The evaluation of the local ADC method above has yielded a set of optimal parameters to use with the minimal bumping scheme. This set of parameters consists of bumping model 1, $x = 0.5 \text{ \AA}$ as bumping distance, and $N = 6$ as number of blocks in which the occupied orbital space is split. Now, the parameters will be employed in the calculation of the lowest excited states of a larger set of test molecules to verify that they are sufficient for other molecules, as well, and to test how much will be gained by the use of the local ADC scheme.

Testing the Bumping

In order to test the quality of the bumping parameters which have been determined in the previous section we employ these parameters in excited state calculations on a large set of test molecules. As test set we have chosen the same set of molecules that has already been employed by Korona and Werner [30] and Kats *et al.* [31] in the evaluation of local coupled cluster methods for excited states.

The test set comprises molecules with numbers of electrons ranging from 40 to 88. All molecules are still small enough to allow for the calculation with conventional ADC(2)-s and ADC(2)-x, as well, so that reference data on the excited states can be obtained. In the test set the non-aromatic molecules *N*-methylacetamide, propanamide, and *N*-acetylglycine are included with the ge-

ometrical parameters taken from [181] and [181], respectively. The polypeptide models dipeptide and β -dipeptide from [182] are used with geometries optimized at MP2/6-31G* level. As molecules possessing aromatic rings *trans*-urocanic acid [183] and 1-phenylpyrrole in its twisted structure from [184] are included, as well as 4-dimethylaminobenzonitrile (DMABN) as published in [185] for which the non-specified geometrical parameters have been optimized using MP2/cc-pVDZ. The molecules p-cresol, 3-(4-hydroxyphenyl) propionic acid (HPA), and phenylalanine are also part of the test set with geometries optimized at DFT/B3LYP/6-31G(d) level. The geometrical parameters of all test molecules are compiled in Appendix B.

Table 4.3: Summary of the application of the bumping scheme on the molecules in the test set. The number of orbital blocks and the amount of disregarded doubly excited configurations are given, as well as the maximum deviation in excitation energies (in eV) and oscillator strengths (in brackets) of the six lowest excited states calculated with conventional and local ADC(2)-s and ADC(2)-x using 6-31G(d) basis set.

	number of electrons	number of blocks	ADC(2)		ADC(2)-x	
			neglected doubles	maximum deviation	neglected doubles	maximum deviation
<i>N</i> -methylacetamid	40	4	6.7%	0.098 (0.0074)	6.7%	0.061 (0.0013)
Propanamide	40	4	4.4%	0.065 (0.0061)	4.4%	0.037 (0.0026)
<i>P</i> -cresol	58	6	8.9%	0.020 (0.0617)	8.9%	0.014 (0.0079)
<i>N</i> -acetylglycine	62	6	16.7%	0.083 (0.0147)	16.7%	0.061 (0.0095)
Dipeptide	70	7	23.8%	0.078 (0.0040)	21.5%	0.072 (0.0032)
<i>Trans</i> -urocanic acid	72	7	15.2%	0.047 (0.0750)	15.2%	0.078 (0.0086)
1-phenylpyrrole	76	8	15.6%	0.134 (0.0211)	15.6%	0.119 (0.0285)
β -dipeptide	78	8	33.1%	0.033 (0.0106)	33.1%	0.014 (0.0355)
DMABN	78	6	13.2%	0.069 (0.0600)	13.2%	0.056 (0.0056)
HPA	88	9	32.0%	0.026 (0.0263)	32.0%	0.022 (0.0087)
Phenylalanine	88	5	9.3%	0.015 (0.0843)	9.3%	0.010 (0.0557)

For all molecules ADC(2)-s and ADC(2)-x calculations have been performed using local orbitals, as well as canonical Hartree-Fock orbitals. For the local calculations the bumping model 1 has been employed with bumping distance x set to 0.5 Å. The number of blocks, in which the occupied and virtual orbitals are split, has been set depending on the molecular size. In general, this parameter has been chosen so that the average number of occupied orbitals per block is approximately 10. The only exceptions are DMABN and phenylalanine for which a smaller number of blocks has been tested. The average number of occupied orbitals per block

is 13 for DMABN, and 18 for phenylalanine.

The results of the calculations are compiled in Table 4.3 and Table 4.4. In both tables the molecules are sorted by their number of electrons. Examining the amount of neglected doubly excited configurations in Table 4.3, it becomes obvious that due to the rather large number of orbitals per block in case of DMABN and phenylalanine the amount of neglected doubly excited configurations is much smaller than for other molecules of similar size. This is particularly pronounced for phenylalanine for which only 9.3% of doubly excited configurations are disregarded, while for the equally large HPA molecule already 32% of the doubly excited configurations are neglected. The calculations of the two linear polypeptide models, dipeptide and β -dipeptide, show 23.8% and 33.1% neglect of doubly excited configurations. In contrast, for *trans*-urocanic acid and 1-phenylpyrrole the amount of disregarded double excited configurations is only 15.2% and 15.6%, respectively. Still, *trans*-urocanic acid is almost as large as the dipeptide molecule, and 1-phenylpyrrole has similar size to β -dipeptide. The main difference is the geometric form of the molecules. The polypeptide models are linear and thus more extended than the other two molecules possessing aromatic ring. This means the amount of neglected doubly excited configurations is clearly correlated to the spatial extension of the molecule.

Overall, the parts of the doubly excited configurations which are neglected increase with increasing system size. In the calculations of smaller molecules, like *N*-methylacetamide or propanamide, less than 10% of the doubly excited configurations are disregarded, while in the calculations of β -dipeptide as much as 33% of the doubly excited configurations do not need to be taken into account. Still, the maximum deviations of the vertical excitation energies of the six lowest excited states do not increase for larger systems. The errors are less than 0.15 eV for all test molecules. The local ADC(2)-s results exhibit in all cases a slightly larger maximum deviation from the results of the non-local calculations than the local ADC(2)-x results. The largest deviation is found in the calculation of the excited states of 1-phenylpyrrole. It amounts to 0.13 eV and 0.12 eV for local ADC(2)-s and local ADC(2)-x, respectively. As can be seen from Table 4.4, only the vertical excitation energies of the fourth excited state of 1-phenylpyrrole show this large error. The vertical excitation energies of the other states deviate by less than 0.10 eV, as do all calculated excited states of the other molecules. To motivate

the larger deviation of the fourth excited state of 1-phenylpyrrole it is helpful to analyze the respective excited states vectors. For both methods, ADC(2)-s and ADC(2)-x, they mainly consist of eight singly excited configurations which represent excitations from the pyrrole to the phenyl ring. Thus, this excited state corresponds to a charge transfer excitation from the pyrrole to the phenyl ring. The increased error of the vertical excitation energy of the state can be attributed to the way how bumping model 1 neglects doubly excited configurations. In bumping model 1 (see Figure 3.4), the doubly excited configurations describing double charge transfers, or single charge transfers combined with distant local excitations are almost always disregarded. Since these contributions most likely couple to singly excited configurations describing a charge transfer, their missing influence may be the cause of the larger error in the excitation energies of the charge transfer excitation.

Yet, the largest deviation of the vertical excitation energies obtained with local ADC(2)-s and local ADC(2)-x does not exceed the threshold specified in the previous section for any of the molecules in the test set. Thus, the bumping distance $x = 0.5 \text{ \AA}$ which has been determined by calculations on octatetraene using this threshold criterion seems to be a reasonable choice in combination with bumping model 1 for the application of the local ADC(2)-s and ADC(2)-x methods to any kind of system.

Table 4.4: Comparison of local and conventional ADC(2)-s vertical excitation energies and oscillator strengths (in brackets) for various molecules. The calculations were performed at the geometries given in Appendix B using 6-31G(d) basis set. In the local calculations bumping model 1 and bumping distance $x = 0.5 \text{ \AA}$ have been employed. All excitation energies are specified in eV.

	ADC(2)	local ADC(2)	Deviations
<i>N</i> -methylacetamide	5.58 (0.0012)	5.59 (0.0012)	0.009 (-0.0000)
	7.32 (0.2328)	7.33 (0.2348)	0.009 (0.0020)
	8.12 (0.0005)	8.13 (0.0005)	0.010 (0.0000)
	8.34 (0.0829)	8.39 (0.0832)	0.044 (0.0003)
	9.90 (0.0281)	10.00 (0.0207)	0.098 (-0.0074)
	10.03 (0.0469)	10.06 (0.0482)	0.031 (0.0013)
Propanamide	5.61 (0.0007)	5.62 (0.0007)	0.006 (-0.0000)
	7.69 (0.2002)	7.70 (0.2003)	0.005 (0.0001)
	8.51 (0.1369)	8.53 (0.1423)	0.027 (0.0054)
	8.59 (0.0026)	8.60 (0.0026)	0.004 (-0.0000)
	9.46 (0.0445)	9.53 (0.0384)	0.065 (-0.0061)
	9.81 (0.0005)	9.82 (0.0005)	0.007 (0.0000)
<i>P</i> -cresol	5.05 (0.0382)	5.06 (0.0379)	0.010 (-0.0003)
	6.39 (0.2495)	6.41 (0.2417)	0.020 (-0.0078)
	7.42 (0.7086)	7.43 (0.7703)	0.009 (0.0617)
	7.45 (0.6653)	7.46 (0.6222)	0.009 (-0.0431)
	7.61 (0.0010)	7.62 (0.0010)	0.008 (0.0000)
	8.26 (0.0000)	8.27 (0.0000)	0.013 (-0.0000)
<i>N</i> -acetylglycine	5.57 (0.0012)	5.57 (0.0012)	0.002 (0.0000)
	5.95 (0.0005)	5.95 (0.0005)	0.006 (-0.0000)
	7.28 (0.1319)	7.30 (0.1467)	0.018 (0.0147)
	7.57 (0.1637)	7.60 (0.1504)	0.030 (-0.0133)
	7.88 (0.0000)	7.96 (0.0000)	0.083 (-0.0000)
	8.45 (0.1830)	8.46 (0.1827)	0.007 (-0.0003)
Dipeptide	5.59 (0.0011)	5.59 (0.0012)	0.004 (0.0000)
	5.80 (0.0008)	5.81 (0.0008)	0.013 (-0.0000)
	7.21 (0.1270)	7.22 (0.1310)	0.011 (0.0040)
	7.30 (0.3948)	7.31 (0.3945)	0.008 (-0.0002)
	7.93 (0.0901)	7.96 (0.0898)	0.026 (-0.0003)
	8.20 (0.0000)	8.28 (0.0000)	0.078 (0.0000)

(Table 4.4 continued)

	ADC(2)	local ADC(2)	Deviation
<i>Trans</i> -urocanic acid	4.78 (0.0001)	4.82 (0.0001)	0.038 (0.0000)
	5.21 (0.8045)	5.25 (0.7953)	0.039 (-0.0092)
	6.30 (0.0731)	6.31 (0.0019)	0.012 (-0.0712)
	6.30 (0.0018)	6.35 (0.0768)	0.047 (0.0750)
	6.90 (0.1873)	6.93 (0.1908)	0.033 (0.0036)
	7.07 (0.0079)	7.07 (0.0080)	0.002 (0.0000)
1-phenylpyrrole	5.13 (0.0050)	5.15 (0.0046)	0.022 (-0.0004)
	5.62 (0.5197)	5.67 (0.5206)	0.046 (0.0009)
	5.93 (0.0201)	6.00 (0.0222)	0.075 (0.0020)
	6.33 (0.0013)	6.47 (0.0014)	0.134 (0.0001)
	6.70 (0.1350)	6.78 (0.1562)	0.085 (0.0211)
	6.90 (0.0159)	6.91 (0.0167)	0.006 (0.0009)
β -dipeptide	5.53 (0.0013)	5.55 (0.0013)	0.014 (-0.0000)
	5.60 (0.0006)	5.61 (0.0006)	0.014 (-0.0000)
	7.24 (0.3563)	7.26 (0.3668)	0.013 (0.0106)
	7.28 (0.1753)	7.30 (0.1712)	0.018 (-0.0041)
	8.10 (0.0010)	8.12 (0.0007)	0.017 (-0.0004)
	8.11 (0.0011)	8.14 (0.0014)	0.033 (0.0003)
DMABN	4.60 (0.0361)	4.63 (0.0359)	0.028 (-0.0001)
	4.80 (0.7802)	4.86 (0.7872)	0.061 (0.0070)
	6.37 (0.1570)	6.40 (0.1675)	0.031 (0.0105)
	7.21 (0.0973)	7.24 (0.1573)	0.028 (0.0600)
	7.22 (0.0000)	7.29 (0.0000)	0.069 (0.0000)
	7.42 (0.0136)	7.44 (0.0139)	0.024 (0.0002)
HPA	5.05 (0.0321)	5.06 (0.0320)	0.010 (-0.0001)
	5.69 (0.0108)	5.70 (0.0096)	0.013 (-0.0012)
	6.28 (0.3585)	6.31 (0.3480)	0.026 (-0.0105)
	7.34 (0.4985)	7.35 (0.5248)	0.016 (0.0263)
	7.39 (0.9121)	7.40 (0.9116)	0.010 (-0.0005)
	7.67 (0.0036)	7.70 (0.0026)	0.025 (-0.0011)
Phenylalanine	5.32 (0.0001)	5.32 (0.0001)	0.002 (-0.0000)
	5.81 (0.0011)	5.81 (0.0011)	0.000 (-0.0000)
	6.69 (0.1079)	6.69 (0.1060)	0.003 (-0.0019)
	7.06 (0.0528)	7.06 (0.0520)	0.003 (-0.0008)
	7.43 (0.5213)	7.44 (0.6057)	0.015 (0.0843)
	7.49 (0.5273)	7.50 (0.5517)	0.008 (0.0244)

Chapter 5

Conclusions and Outlook

5.1 Energy and Electron Transfer Processes in Photosynthesis

In this thesis, excitation energy and electron transfer processes in light-harvesting complexes LH2 and LHC-II have been investigated by means of quantum chemical methods. Therefore, model complexes for the experimentally observed carotenoid radical cation formation in LH2, and the non-photochemical quenching in LHC-II have been constructed based on the respective crystal structures of the complexes. The model complexes have been used to calculate potential energy curves along suitable reaction coordinates employing TD-DFT and CIS.

To investigate the carotenoid radical cation formation in LH2, three model complexes have been built consisting of one carotenoid and one bacteriochlorophyll molecule. For each of the model complexes potential energy curves have been calculated along the distance between the respective molecules. By comparison of the calculations with experimental data a schematic energy level diagram has been deduced. Based on this diagram we have concluded that the precursor state of the carotenoid radical cation formation is most likely the vibrationally excited S_1 state of the carotenoid. However, due to the missing influence of the protein in the models this could not be conclusively determined. Still, we could propose a pump-deplete-probe experiment to test this mechanism.

For the investigations on non-photochemical quenching in LHC-II, first, the hypothesis has been tested that the replacement of violaxanthin by zeaxanthin

in the binding pocket of LHC-II is the quenching mechanism of NPQ. As model complexes, violaxanthin–chlorophyll and zeaxanthin–chlorophyll in the geometry of the X-ray structure have been used to calculate potential energy curves along the distance coordinate between the two molecules, respectively. From these curves it could be seen that almost no difference in the excited states exist between violaxanthin and zeaxanthin in the binding pocket of LHC-II. Thus, the quenching will most likely not proceed via zeaxanthin inside the LHC-II. This could also be confirmed by pump-probe experiments on purified LHC-II complexes. Secondly, calculations on lutein–chlorophyll complexes have been performed, since based on resonance Raman and transient absorption spectroscopy the formation of a lutein–chlorophyll quenching complex has been suggested as mechanism of NPQ. Again the potential energy curves have been calculated along a distance coordinate between the two molecules of the model complexes. The resulting curves showed that if a lutein–chlorophyll quenching complex is formed during NPQ, this complex will most likely comprise the lutein 501 and not the lutein 502.

All these theoretical studies have been performed on model complexes for the LHCs which consist of just two pigment molecules. The influence of the protein environment and other surrounding molecules has been neglected almost completely. Additionally, the accuracy of the employed methods is rather limited. Thus, only limited conclusions could be drawn from the calculations. To allow for better interpretation of the model calculations the employed model complexes should be improved. One possibility to do so is to include the protein environment as point charges in the calculations. Such extended calculations on model complexes have already been performed, and preliminary results suggest that point charges might recover some effects of the protein environment. Another way to proceed is to use more accurate quantum chemical methods in the calculation of the excited states of the model complexes. Therefore, we have started developing an improved version of the algebraic diagrammatic construction scheme (see below) to be able to obtain more reliable results in the future.

5.2 ADC Calculations on Model Systems

To overcome the deficiencies in the investigations of excitation energy and electron transfer processes with respect to the employed methods we have turned to the algebraic diagrammatic construction scheme. Its second order variants are among the cheapest excited state methods which provide balanced descriptions of low-lying excited states, including local, charge transfer and Rydberg excitations. In calculations on linear polyenes which served as model systems for the much larger carotenoids in light-harvesting complexes we could show that ADC(2)-x yields excitation energies of the few lowest excited states which are in acceptable agreement with experimental data. Additionally, it became clear by this investigation that the good quality of the excitation energies obtained by TD-DFT for linear polyenes is due to fortuitous cancellation of errors. However, the large computational costs of ADC prevent its application to larger molecular systems.

Thus, we have started the development of an efficient implementation of the algebraic diagrammatic construction scheme to extend its applicability. Therefore, the second order ADC schemes have been implemented in the Q-Chem package of programs employing the Davidson algorithm as efficient solver of the eigenvalue problem inherent in ADC. Additionally, the ADC working equations have been modified to enable the use of local orbitals in the calculations. Local orbitals, first of all, increase computational costs. However, if contributions of far distant orbitals in the ADC equations are neglected, they can lead to substantial reduction of computation time and disc space for larger systems. To take advantage of the local orbitals a simple bumping scheme has been implemented which disregards parts of the eigenvectors in ADC based on the distances of the local orbitals.

The bumping scheme has introduced a set of parameters by which the bumping can be adjusted. To find optimal values for these parameters, several sets of values have been evaluated using the linear polyene octatetraene as test system. As optimal parameter set those values were regarded that maximized the neglected parts of the eigenvectors while keeping the error of the excitation energies below a threshold of 0.15 eV. The evaluation has yielded an optimal parameter set consisting of “bumping model 1”, and the bumping distance $x = 0.5 \text{ \AA}$. Using the obtained parameter set ADC calculations have been performed on a number of small and medium-sized molecules. By these calculations it has been shown that

with growing system size more and more contributions to the eigenvectors can be neglected without losing the accuracy of the calculations. No computation times have been given, since the calculations have been performed on different computers making comparisons almost impossible. Though, it can be estimated from the computation times that for molecules consisting of 80–100 electrons the local ADC method using the implemented bumping scheme will be faster than conventional ADC.

As further step, the bumping scheme can be extended, so that not only eigenvectors, but also integrals and other data objects are subject to the bumping. This way, the computation times and disk space requirements of local ADC can be reduced even more, thereby shifting the point when local ADC becomes faster than conventional ADC to smaller molecular sizes. Also, the use of a more sophisticated bumping scheme with more parameters has already been prepared.

A different approach to make ADC applicable to larger systems might be the transformation of the ADC equations into atomic orbitals. Then, the calculation of the integrals by multipole expansion can be used. Additionally, atomic orbitals are as a matter of fact local, so that the bumping scheme for local orbitals might be applicable, too.

Appendix A

Algebraic Diagrammatic Construction

In this section various ways to express the building blocks of the Algebraic Diagrammatic Construction scheme are presented.

A.1 The Original ADC Equations

The expressions for the ADC matrix have been published in [71]. Here, they are once again compiled sorted by the order of perturbation theory to which they contribute. Remember that all terms which involve doubly excited configurations are subject to the restrictions of the indices $a < b$ and $i < j$.

- Zeroth order:

$$K_{ia,jb} = (\epsilon_a - \epsilon_i) \delta_{ab} \delta_{ij} \quad (\text{A.1})$$

- First order:

$$C_{ia,jb}^{(1)} = -\langle aj | |bi \rangle \quad (\text{A.2})$$

- Second order:

$$C_{ia,jb}^{(2)} = C_{ia,jb}^{(2)A} + C_{ia,jb}^{(2)B} + C_{ia,jb}^{(2)C} \quad (\text{A.3})$$

with

$$\begin{aligned}
C_{ia,jb}^{(2)A} &= \frac{1}{4} \delta_{ij} \sum_{ckl} \left[\frac{\langle ac | kl \rangle \langle kl | bc \rangle}{\epsilon_a + \epsilon_c - \epsilon_k - \epsilon_l} + \frac{\langle ac | kl \rangle \langle kl | bc \rangle}{\epsilon_b + \epsilon_c - \epsilon_k - \epsilon_l} \right] \\
C_{ia,jb}^{(2)B} &= \frac{1}{4} \delta_{ab} \sum_{cdk} \left[\frac{\langle cd | ik \rangle \langle jk | cd \rangle}{\epsilon_c + \epsilon_d - \epsilon_i - \epsilon_k} + \frac{\langle cd | ik \rangle \langle jk | cd \rangle}{\epsilon_c + \epsilon_d - \epsilon_j - \epsilon_k} \right] \\
C_{ia,jb}^{(2)C} &= -\frac{1}{2} \sum_{ck} \left[\frac{\langle ac | ik \rangle \langle jk | bc \rangle}{\epsilon_a + \epsilon_c - \epsilon_i - \epsilon_k} + \frac{\langle ac | ik \rangle \langle jk | bc \rangle}{\epsilon_b + \epsilon_c - \epsilon_j - \epsilon_k} \right]
\end{aligned}$$

$$C_{ia,kcl}^{(1)} = \langle kl | id \rangle \delta_{ac} - \langle kl | ic \rangle \delta_{ad} - \langle al | cd \rangle \delta_{ik} + \langle ak | cd \rangle \delta_{il} \quad (\text{A.4})$$

$$C_{ia,jb,kc}^{(1)} = \langle kb | ij \rangle \delta_{ac} - \langle ka | ij \rangle \delta_{bc} - \langle ab | cj \rangle \delta_{ik} + \langle ab | ci \rangle \delta_{jk} \quad (\text{A.5})$$

$$K_{iajb,kcl} = (\epsilon_a + \epsilon_b - \epsilon_i - \epsilon_j) \delta_{ac} \delta_{bd} \delta_{ik} \delta_{jl} \quad (\text{A.6})$$

- Extension to second order:

$$\begin{aligned}
C_{iajb,kcl}^{(1)} &= \langle ab || cd \rangle \delta_{ik} \delta_{jl} + \langle kl || ij \rangle \delta_{ac} \delta_{bd} \\
&- \left[\langle ak || ci \rangle \delta_{bd} \delta_{jl} + \langle al || cj \rangle \delta_{bd} \delta_{ik} + \langle bk || di \rangle \delta_{ac} \delta_{jl} + \langle bl || dj \rangle \delta_{ac} \delta_{ik} \right] \\
&+ \left[\langle al || ci \rangle \delta_{bd} \delta_{jk} + \langle ak || cj \rangle \delta_{bd} \delta_{il} + \langle bl || di \rangle \delta_{ac} \delta_{jk} + \langle bk || dj \rangle \delta_{ac} \delta_{il} \right] \quad (\text{A.7}) \\
&+ \left[\langle ak || di \rangle \delta_{bc} \delta_{jl} + \langle al || dj \rangle \delta_{bc} \delta_{ik} + \langle bk || ci \rangle \delta_{ad} \delta_{jl} + \langle bl || cj \rangle \delta_{ad} \delta_{ik} \right] \\
&- \left[\langle al || di \rangle \delta_{bc} \delta_{jk} + \langle ak || dj \rangle \delta_{bc} \delta_{il} + \langle bl || ci \rangle \delta_{ad} \delta_{jk} + \langle bk || cj \rangle \delta_{ad} \delta_{il} \right]
\end{aligned}$$

To the originally published ADC equations belong as well the modified transition moments listed in the following.

- Zeroth order:

$$F_{ia}^{(0)} = D_{ia} \quad (\text{A.8})$$

- First order:

$$F_{ia}^{(1)} = \sum_{bj} \frac{\langle ab || ji \rangle}{\epsilon_a + \epsilon_b - \epsilon_j - \epsilon_i} D_{jb} \quad (\text{A.9})$$

- Second order:

$$F_{ia}^{(2)} = F_{ia}^{(2)A} + F_{ia}^{(2)B} + F_{ia}^{(2)C} + \sum_{I=1}^{10} F_{ia}^{(2,I)} \quad (\text{A.10})$$

$$F_{ia}^{(2)A} = -\frac{1}{4} \sum_{bjck} \frac{\langle ab | jk \rangle}{\epsilon_a + \epsilon_b - \epsilon_j - \epsilon_k} \frac{\langle jk | cb \rangle}{\epsilon_c + \epsilon_b - \epsilon_j - \epsilon_k} D_{ci}$$

$$F_{ia}^{(2)B} = -\frac{1}{4} \sum_{bjck} \frac{\langle bc | ij \rangle}{\epsilon_b + \epsilon_c - \epsilon_i - \epsilon_j} \frac{\langle kj | bc \rangle}{\epsilon_b + \epsilon_c - \epsilon_k - \epsilon_j} D_{ak}$$

$$F_{ia}^{(2)C} = \frac{1}{2} \sum_{bjck} \frac{\langle ab | ij \rangle}{\epsilon_a + \epsilon_b - \epsilon_i - \epsilon_j} \frac{\langle kj | cb \rangle}{\epsilon_c + \epsilon_b - \epsilon_k - \epsilon_j} D_{ck}$$

$$F_{ia}^{(2,1)} = -\frac{1}{2} \sum_{bjck} \frac{\langle bc | jk \rangle}{\epsilon_b + \epsilon_c - \epsilon_j - \epsilon_k} \frac{\langle ja | bc \rangle}{\epsilon_a - \epsilon_k} D_{ki}$$

$$F_{ia}^{(2,2)} = \frac{1}{2} \sum_{bjkl} \frac{\langle ba | jk \rangle}{\epsilon_a + \epsilon_b - \epsilon_j - \epsilon_k} \frac{\langle jk | bl \rangle}{\epsilon_a - \epsilon_l} D_{li}$$

$$F_{ia}^{(2,3)} = -\frac{1}{2} \sum_{bjck} \frac{\langle bc | jk \rangle}{\epsilon_b + \epsilon_c - \epsilon_j - \epsilon_k} \frac{\langle jk | ic \rangle}{\epsilon_b - \epsilon_i} D_{ab}$$

$$F_{ia}^{(2,4)} = \frac{1}{2} \sum_{bcjd} \frac{\langle bc | ij \rangle}{\epsilon_b + \epsilon_c - \epsilon_i - \epsilon_j} \frac{\langle dj | bc \rangle}{\epsilon_d - \epsilon_i} D_{ad}$$

$$F_{ia}^{(2,5)} = \sum_{bjck} \frac{\langle bc | kj \rangle}{\epsilon_b + \epsilon_c - \epsilon_k - \epsilon_j} \frac{\langle aj | bi \rangle}{\epsilon_a + \epsilon_c - \epsilon_i - \epsilon_k} D_{kc}$$

$$F_{ia}^{(2,6)} = \sum_{bjck} \frac{\langle ab | ji \rangle}{\epsilon_a + \epsilon_b - \epsilon_j - \epsilon_i} \frac{\langle jc | kb \rangle}{\epsilon_a + \epsilon_c - \epsilon_i - \epsilon_k} D_{kc}$$

$$F_{ia}^{(2,7)} = -\sum_{bjck} \frac{\langle cb | ji \rangle}{\epsilon_c + \epsilon_b - \epsilon_j - \epsilon_i} \frac{\langle aj | kc \rangle}{\epsilon_a + \epsilon_b - \epsilon_i - \epsilon_k} D_{kb}$$

$$F_{ia}^{(2,8)} = -\sum_{bjck} \frac{\langle ac | kj \rangle}{\epsilon_a + \epsilon_c - \epsilon_k - \epsilon_j} \frac{\langle jb | ci \rangle}{\epsilon_a + \epsilon_b - \epsilon_i - \epsilon_k} D_{kb}$$

$$F_{ia}^{(2,9)} = -\frac{1}{2} \sum_{bjcd} \frac{\langle cd | ji \rangle}{\epsilon_c + \epsilon_d - \epsilon_j - \epsilon_i} \frac{\langle ab | cd \rangle}{\epsilon_a + \epsilon_b - \epsilon_i - \epsilon_j} D_{jb}$$

$$F_{ia}^{(2,10)} = -\frac{1}{2} \sum_{bjkl} \frac{\langle ab | kl \rangle}{\epsilon_a + \epsilon_b - \epsilon_k - \epsilon_l} \frac{\langle kl | ji \rangle}{\epsilon_a + \epsilon_b - \epsilon_i - \epsilon_j} D_{jb}$$

$$\begin{aligned}
F_{iajb}^{(2)} = & \sum_k \frac{\langle ab | ki \rangle}{\epsilon_a + \epsilon_b - \epsilon_k - \epsilon_i} D_{kj} - \sum_k \frac{\langle ab | kj \rangle}{\epsilon_a + \epsilon_b - \epsilon_k - \epsilon_j} D_{ki} \\
& + \sum_c \frac{\langle cb | ij \rangle}{\epsilon_c + \epsilon_b - \epsilon_i - \epsilon_j} D_{ac} - \sum_c \frac{\langle ca | ij \rangle}{\epsilon_c + \epsilon_a - \epsilon_i - \epsilon_j} D_{bc}
\end{aligned} \tag{A.11}$$

A.2 Multiplying the ADC Matrix

Utilization of the Davidson algorithm along with the ADC scheme requires to rewrite the matrix expressions above as matrix-vector products. The corresponding equations are compiled in the table below sorted by the order of perturbation theory at which the terms occur first.

0 th	$r_{ia} = (\epsilon_a - \epsilon_i) v_{ia}$
1 st	$-\sum_{bj} \langle aj bi \rangle v_{jb}$
2 nd	$ \begin{aligned} & + \sum_b \tilde{v}_{ab} v_{ib} + \sum_j \tilde{v}_{ij} v_{ja} - \frac{1}{2} \sum_{jb} \left[\frac{\langle ab ij \rangle}{\epsilon_a + \epsilon_b - \epsilon_i - \epsilon_j} \tilde{v}_{jb}^{(1)} + \langle ab ij \rangle \tilde{v}_{jb}^{(2)} \right] \\ & - \sum_{c < a, k < l}^{kcl} v_{kcla} \langle ic kl \rangle + \sum_{c > a, k < l}^{kcl} v_{kalc} \langle ic kl \rangle \\ & + \sum_{c < d, k < i}^{ckd} \langle ak cd \rangle v_{kcid} - \sum_{c < d, k > i}^{ckd} \langle ak cd \rangle v_{ickd} \end{aligned} $
$r_{iajb} =$	$ \begin{aligned} & (\epsilon_a - \epsilon_i + \epsilon_b - \epsilon_j) v_{iajb} \\ & + \sum_k [v_{ka} \langle kb ij \rangle - v_{kb} \langle ka ij \rangle] - \sum_c [\langle ab cj \rangle v_{ic} - \langle ab ci \rangle v_{jc}] \end{aligned} $
2 ^{nd-X}	$ \begin{aligned} & + \sum_{c < d}^{cd} \langle ab cd \rangle v_{icjd} + \sum_{k < l}^{kl} v_{kalb} \langle ij kl \rangle \\ & - \sum_{c < b, k < j}^{kc} \langle ak ci \rangle v_{kcjb} + \sum_{c > b, k < j}^{kc} \langle ak ci \rangle v_{kbjc} \\ & + \sum_{c < b, k > j}^{kc} \langle ak ci \rangle v_{jckb} - \sum_{c > b, k > j}^{kc} \langle ak ci \rangle v_{jbkc} \\ & + \sum_{c < b, k < i}^{kc} \langle ak cj \rangle v_{kcib} - \sum_{c > b, k < i}^{kc} \langle ak cj \rangle v_{kbic} \\ & - \sum_{c < b, k > i}^{kc} \langle ak cj \rangle v_{ickb} + \sum_{c > b, k > i}^{kc} \langle ak cj \rangle v_{ibkc} \\ & + \sum_{c < a, k < j}^{kc} \langle bk ci \rangle v_{kcja} - \sum_{c > a, k < j}^{kc} \langle bk ci \rangle v_{kajc} \\ & - \sum_{c < a, k > j}^{kc} \langle bk ci \rangle v_{jcka} + \sum_{c > a, k > j}^{kc} \langle bk ci \rangle v_{jakc} \\ & - \sum_{c < a, k < i}^{kc} \langle bk cj \rangle v_{kcia} + \sum_{c > a, k < i}^{kc} \langle bk cj \rangle v_{kaic} \\ & + \sum_{c < a, k > i}^{kc} \langle bk cj \rangle v_{icka} - \sum_{c > a, k > i}^{kc} \langle bk cj \rangle v_{iakc} \end{aligned} $

The intermediates used in these expressions have been given in equations (3.98) and (3.99).

A.3 ADC in Spin Components

For numerical purposes it is advantageous to extract the spin from the indices in the ADC equations. This results in five blocks for each vector. For the two pure-spin blocks of doubly excited configurations the restrictions $a < b$ and $i < j$ have been lifted. The notation of the two-electron integrals has been changed to the Mulliken notation: $\langle pq || rs \rangle = (pr|qs) - (ps|qr)$. Additionally, so-called t-amplitudes have been introduced as $t_{iajb} = \frac{(ai|bj)}{\epsilon_a - \epsilon_i + \epsilon_b - \epsilon_j}$. The resulting equations are given below.

1. Singly excited configurations:

$$\begin{aligned}
r_{ia} = & (\epsilon_a - \epsilon_i) v_{ia} - \sum_{jb} [(ab|ji) - (ai|jb)] v_{jb} + \sum_{\bar{j}\bar{b}} (ai|\bar{j}\bar{b}) v_{\bar{j}\bar{b}} \\
& + \sum_b \tilde{v}_{ab} v_{ib} + \sum_j \tilde{v}_{ij} v_{ja} - \frac{1}{2} \sum_{\bar{j}\bar{b}} [t_{ia\bar{j}\bar{b}} \tilde{v}_{\bar{j}\bar{b}}^{(1)} + (ai|\bar{b}\bar{j}) \tilde{v}_{\bar{j}\bar{b}}^{(2)}] \\
& - \frac{1}{2} \sum_{jb} [(t_{iajb} - t_{jaib}) \tilde{v}_{jb}^{(1)} + [(ai|bj) - (aj|bi)] \tilde{v}_{jb}^{(2)}] \\
& + \sum_{kcl} v_{kalc} (ik|cl) + \sum_{\bar{k}\bar{c}\bar{l}} v_{ka\bar{l}\bar{c}} (i\bar{k}|\bar{c}\bar{l}) \\
& - \sum_{ckd} (ac|kd) v_{ickd} - \sum_{\bar{c}\bar{k}\bar{d}} (ac|\bar{k}\bar{d}) v_{i\bar{c}\bar{k}\bar{d}} \quad (A.12)
\end{aligned}$$

with

$$\begin{aligned}
\tilde{v}_{ab} = & \frac{1}{2} \sum_{kcl} [t_{kalc} (kb|lc) - t_{kalc} (kc|lb) + (ak|cl) t_{kblc}^* - (al|ck) t_{kblc}^*] \\
& + \frac{1}{2} \sum_{\bar{k}\bar{c}\bar{l}} [t_{ka\bar{l}\bar{c}} (k\bar{b}|\bar{l}\bar{c}) + (ak|\bar{c}\bar{l}) t_{kbl\bar{c}}^*] \quad (A.13)
\end{aligned}$$

$$\begin{aligned}
\tilde{v}_{ij} = & \frac{1}{2} \sum_{ckd} [t_{ickd} (jc|kd) - t_{ickd} (jd|kc) + (ci|dk) t_{jckd}^* - (ck|di) t_{jckd}^*] \\
& + \frac{1}{2} \sum_{\bar{c}\bar{k}\bar{d}} [t_{i\bar{c}\bar{k}\bar{d}} (j\bar{c}|\bar{k}\bar{d}) + (ci|\bar{d}\bar{k}) t_{j\bar{c}\bar{k}\bar{d}}^*] \quad (A.14)
\end{aligned}$$

$$\tilde{v}_{ia}^{(1)} = \sum_{jb} [(jb|ia) - (ja|ib)] v_{jb} + \sum_{\bar{j}\bar{b}} (\bar{j}\bar{b}|ia) v_{\bar{j}\bar{b}} \quad (A.15)$$

$$\tilde{v}_{ia}^{(2)} = \sum_{jb} [t_{iajb}^* - t_{jaib}^*] v_{jb} + \sum_{\bar{j}\bar{b}} t_{ia\bar{j}\bar{b}}^* v_{\bar{j}\bar{b}} \quad (A.16)$$

The corresponding expressions for β -spin can be obtained by replacing every α -spin index (without bar) with a β -spin index (with bar) and vice versa. The opposite-spin parts of the doubly excited configurations $v_{ia\bar{j}b}$ become $v_{j\bar{b}i\bar{a}}$.

2. Doubly excited configurations

$$\begin{aligned}
r_{iajb} = & (\epsilon_a - \epsilon_i + \epsilon_b - \epsilon_j) v_{iajb} \\
& + \sum_k [v_{ka}(ki|bj) - v_{ka}(kj|bi) - v_{kb}(ki|aj) + v_{kb}(kj|ai)] \\
& - \sum_c [v_{ic}(ac|bj) - v_{ic}(aj|bc) - v_{jc}(ac|bi) + v_{jc}(bc|ai)] \\
& + \sum_{cd} (ac|bd) v_{icjd} + \sum_{kl} (ik|jl) v_{kalb} \\
& - \sum_{kc} [(ac|ki) v_{jbkc} - (ai|kc) v_{jbkc} - (ac|kj) v_{ibkc} + (aj|kc) v_{ibkc} \\
& - (bc|ki) v_{jake} + (bi|kc) v_{jake} + (bc|kj) v_{iack} - (bj|kc) v_{iack}] \\
& + \sum_{\bar{k}\bar{c}} [(ai|\bar{k}\bar{c}) v_{j\bar{b}\bar{k}\bar{c}} - (aj|\bar{k}\bar{c}) v_{i\bar{b}\bar{k}\bar{c}} - (bi|\bar{k}\bar{c}) v_{j\bar{a}\bar{k}\bar{c}} + (bj|\bar{k}\bar{c}) v_{i\bar{a}\bar{k}\bar{c}}] \quad (A.17)
\end{aligned}$$

$$\begin{aligned}
r_{ia\bar{j}b} = & (\epsilon_a - \epsilon_i + \epsilon_{\bar{b}} - \epsilon_{\bar{j}}) v_{ia\bar{j}b} \\
& + \sum_k v_{ka}(ki|\bar{b}\bar{j}) + \sum_{\bar{k}} v_{\bar{k}\bar{b}}(\bar{k}\bar{j}|ai) - \sum_c v_{ic}(ac|\bar{b}\bar{j}) - \sum_{\bar{c}} v_{j\bar{c}}(\bar{b}\bar{c}|ai) \\
& + \sum_{\bar{c}\bar{d}} (ac|\bar{b}\bar{d}) v_{ic\bar{j}\bar{d}} + \sum_{\bar{k}\bar{l}} (ik|\bar{j}\bar{l}) v_{kal\bar{b}} \\
& - \sum_{kc} [(ac|ki) v_{kc\bar{j}\bar{b}} - (ai|kc) v_{kc\bar{j}\bar{b}} - (bj|kc) v_{iack}] \\
& - \sum_{\bar{k}\bar{c}} [(\bar{b}\bar{c}|\bar{k}\bar{j}) v_{i\bar{a}\bar{k}\bar{c}} - (\bar{b}\bar{j}|\bar{k}\bar{c}) v_{i\bar{a}\bar{k}\bar{c}} - (ai|\bar{k}\bar{c}) v_{j\bar{b}\bar{k}\bar{c}}] \\
& - \sum_{\bar{k}\bar{c}} (ac|\bar{k}\bar{j}) v_{i\bar{c}\bar{k}\bar{b}} - \sum_{\bar{k}\bar{c}} (\bar{b}\bar{c}|\bar{k}\bar{i}) v_{k\bar{a}\bar{j}\bar{c}} \quad (A.18)
\end{aligned}$$

Again, the pure β -spin expressions can be obtained from the pure α -spin expressions.

Similar to the ADC matrix-vector products the scalar products of the transition moments with some arbitrary vectors can be written in spin components. This results in the

following expressions for ADC(0) and ADC(1).

$$T^{(0)} = \sum_{ia} D_{ai} v_{ia} + \sum_{\bar{a}\bar{i}} D_{\bar{a}\bar{i}} v_{\bar{a}\bar{i}} \quad (\text{A.19})$$

$$\begin{aligned} T^{(1)} = & - \sum_{ia} v_{ia} \sum_{jb} (t_{iajb} - t_{ibja}) D_{jb} - \sum_{ia} v_{ia} \sum_{\bar{j}\bar{b}} t_{ia\bar{j}\bar{b}} D_{\bar{j}\bar{b}} \\ & - \sum_{\bar{i}\bar{a}} v_{\bar{i}\bar{a}} \sum_{jb} t_{j\bar{b}\bar{i}\bar{a}} D_{jb} - \sum_{\bar{i}\bar{a}} v_{\bar{i}\bar{a}} \sum_{\bar{j}\bar{b}} (t_{\bar{i}\bar{a}\bar{j}\bar{b}} - t_{\bar{i}\bar{b}\bar{j}\bar{a}}) D_{\bar{j}\bar{b}} \end{aligned} \quad (\text{A.20})$$

The second order term consists of six contributions

$$T^{(2)} = T_1^{(2)} + T_2^{(2)} + T_3^{(2)} + T_4^{(2)} + T_5^{(2)} + T_6^{(2)} \quad (\text{A.21})$$

with

$$\begin{aligned} T_1^{(2)} = & \frac{1}{2} \sum_{ia} v_{ia} \sum_{jb} (t_{iajb} - t_{ibja}) \left(\sum_{kc} (t_{jbkc} - t_{jckb}) D_{ck} + \sum_{\bar{k}\bar{c}} t_{jb\bar{k}\bar{c}} D_{\bar{k}\bar{c}} \right) \\ & + \frac{1}{2} \sum_{ia} v_{ia} \sum_{\bar{j}\bar{b}} t_{ia\bar{j}\bar{b}} \left(\sum_{kc} t_{kc\bar{j}\bar{b}} D_{ck} + \sum_{\bar{k}\bar{c}} (t_{\bar{j}bkc} - t_{\bar{j}ckb}) D_{\bar{k}\bar{c}} \right) \\ & + \frac{1}{2} \sum_{\bar{i}\bar{a}} v_{\bar{i}\bar{a}} \sum_{jb} t_{j\bar{b}\bar{i}\bar{a}} \left(\sum_{kc} (t_{jbkc} - t_{jckb}) D_{ck} + \sum_{\bar{k}\bar{c}} t_{j\bar{b}\bar{k}\bar{c}} D_{\bar{k}\bar{c}} \right) \\ & + \frac{1}{2} \sum_{\bar{i}\bar{a}} v_{\bar{i}\bar{a}} \sum_{\bar{j}\bar{b}} (t_{\bar{i}\bar{a}\bar{j}\bar{b}} - t_{\bar{i}\bar{b}\bar{j}\bar{a}}) \left(\sum_{kc} t_{kc\bar{j}\bar{b}} D_{ck} + \sum_{\bar{k}\bar{c}} (t_{\bar{j}bkc} - t_{\bar{j}ckb}) D_{\bar{k}\bar{c}} \right) \end{aligned} \quad (\text{A.22})$$

$$\begin{aligned}
T_2^{(2)} = & -\frac{1}{4} \sum_{ac} \left(\sum_i v_{ia} D_{ci} \right) \sum_{kjb} (t_{kajb} - t_{kbja}) (t_{kcjb} - t_{kbjc}) \\
& -\frac{1}{4} \sum_{ik} \left(\sum_a v_{ia} D_{ak} \right) \sum_{bjc} (t_{ibjc} - t_{icjb}) (t_{kbjc} - t_{kcjb}) \\
& -\frac{1}{4} \sum_{\bar{a}\bar{c}} \left(\sum_{\bar{i}} v_{\bar{i}\bar{a}} D_{\bar{c}\bar{i}} \right) \sum_{\bar{k}\bar{j}\bar{b}} \left(t_{\bar{k}\bar{a}\bar{j}\bar{b}} - t_{\bar{k}\bar{b}\bar{j}\bar{a}} \right) \left(t_{\bar{k}\bar{c}\bar{j}\bar{b}} - t_{\bar{k}\bar{b}\bar{j}\bar{c}} \right) \\
& -\frac{1}{4} \sum_{\bar{i}\bar{k}} \left(\sum_{\bar{a}} v_{\bar{i}\bar{a}} D_{\bar{a}\bar{k}} \right) \sum_{\bar{b}\bar{j}\bar{c}} \left(t_{\bar{i}\bar{b}\bar{j}\bar{c}} - t_{\bar{i}\bar{c}\bar{j}\bar{b}} \right) \left(t_{\bar{k}\bar{b}\bar{j}\bar{c}} - t_{\bar{k}\bar{c}\bar{j}\bar{b}} \right) \\
& -\frac{1}{2} \sum_{ac} \left(\sum_i v_{ia} D_{ci} \right) \sum_{kjb} t_{ka\bar{j}\bar{b}} t_{kc\bar{j}\bar{b}} - \frac{1}{2} \sum_{ik} \left(\sum_a v_{ia} D_{ak} \right) \sum_{bjc} t_{ib\bar{j}\bar{c}} t_{kb\bar{j}\bar{c}} \\
& -\frac{1}{2} \sum_{\bar{a}\bar{c}} \left(\sum_{\bar{i}} v_{\bar{i}\bar{a}} D_{\bar{c}\bar{i}} \right) \sum_{\bar{j}\bar{b}\bar{k}} t_{\bar{j}\bar{b}\bar{k}\bar{a}} t_{\bar{j}\bar{b}\bar{k}\bar{c}} - \frac{1}{2} \sum_{\bar{i}\bar{k}} \left(\sum_{\bar{a}} v_{\bar{i}\bar{a}} D_{\bar{a}\bar{k}} \right) \sum_{\bar{j}\bar{c}\bar{b}} t_{\bar{j}\bar{c}\bar{i}\bar{b}} t_{\bar{j}\bar{c}\bar{k}\bar{b}} \quad (\text{A.23})
\end{aligned}$$

$$\begin{aligned}
T_3^{(2)} = & \sum_{ia} t_{ia}^D \left[\sum_{cjb} (t_{icjb} - t_{ibjc}) (jb|ac) + \sum_{\bar{c}\bar{j}\bar{b}} (\bar{j}\bar{b}|ac) t_{ic\bar{j}\bar{b}} \right. \\
& \left. - \sum_{kjb} (t_{kajb} - t_{kbja}) (ki|jb) - \sum_{\bar{k}\bar{j}\bar{b}} t_{ka\bar{j}\bar{b}} (ki|\bar{j}\bar{b}) \right] \\
& + \sum_{\bar{i}\bar{a}} t_{\bar{i}\bar{a}}^D \left[\sum_{\bar{c}\bar{j}\bar{b}} (\bar{j}\bar{b}|\bar{a}\bar{c}) (t_{\bar{i}\bar{c}\bar{j}\bar{b}} - t_{\bar{i}\bar{b}\bar{j}\bar{c}}) + \sum_{\bar{j}\bar{b}\bar{c}} (jb|\bar{a}\bar{c}) t_{\bar{j}\bar{b}\bar{i}\bar{c}} \right. \\
& \left. - \sum_{\bar{k}\bar{j}\bar{b}} (t_{\bar{k}\bar{a}\bar{j}\bar{b}} - t_{\bar{k}\bar{b}\bar{j}\bar{a}}) (\bar{k}\bar{i}|\bar{j}\bar{b}) - \sum_{\bar{j}\bar{b}\bar{k}} t_{\bar{j}\bar{b}\bar{k}\bar{a}} (\bar{k}\bar{i}|\bar{j}\bar{b}) \right] \quad (\text{A.24})
\end{aligned}$$

$$\begin{aligned}
T_4^{(2)} = & \sum_{iajb} t_{iajb}^D \left[\sum_{kc} (t_{iakc} - t_{icka}) ((jb|kc) - (jk|bc)) + \sum_{\bar{k}\bar{c}} t_{ia\bar{k}\bar{c}} (jb|\bar{k}\bar{c}) \right. \\
& \left. - \sum_{kc} (t_{ibkc} - t_{ickb}) ((ja|kc) - (jk|ac)) - \sum_{\bar{k}\bar{c}} t_{ib\bar{k}\bar{c}} (ja|\bar{k}\bar{c}) \right] \\
& + \sum_{iaj\bar{b}} t_{iaj\bar{b}}^D \left[\sum_{\bar{k}\bar{c}} (t_{ia\bar{k}\bar{c}} - t_{icka}) ((\bar{j}\bar{b}|\bar{k}\bar{c}) - (\bar{j}\bar{k}|\bar{b}\bar{c})) + \sum_{kc} t_{kc\bar{c}\bar{a}} (\bar{j}\bar{b}|kc) \right. \\
& \left. - \sum_{\bar{k}\bar{c}} (t_{\bar{i}\bar{b}\bar{k}\bar{c}} - t_{\bar{i}\bar{c}\bar{k}\bar{b}}) ((\bar{j}\bar{a}|\bar{k}\bar{c}) - (\bar{j}\bar{k}|\bar{a}\bar{c})) - \sum_{kc} t_{kc\bar{c}\bar{b}} (\bar{j}\bar{a}|kc) \right] \\
& + \sum_{iaj\bar{b}} t_{iaj\bar{b}}^D \left[\sum_{kc} (t_{iakc} - t_{icka}) (\bar{j}\bar{b}|kc) + \sum_{\bar{k}\bar{c}} t_{ia\bar{k}\bar{c}} ((\bar{j}\bar{b}|\bar{k}\bar{c}) - (\bar{j}\bar{k}|\bar{b}\bar{c})) \right. \\
& + \sum_{kc} t_{kc\bar{c}\bar{b}} ((ia|kc) - (ik|ac)) + \sum_{kc} (t_{\bar{j}\bar{b}kc} - t_{\bar{j}\bar{c}kb}) (ia|\bar{k}\bar{c}) \\
& \left. - \sum_{\bar{k}\bar{c}} t_{ka\bar{j}\bar{c}} (ik|\bar{b}\bar{c}) - \sum_{\bar{k}\bar{c}} t_{ic\bar{k}\bar{b}} (\bar{j}\bar{k}|ac) \right] \tag{A.25}
\end{aligned}$$

$$\begin{aligned}
T_5^{(2)} = & \frac{1}{2} \sum_{iajb} (t_{iajb}^D - t_{ibja}^D) \left[\sum_{cd} (ac|bd) t_{icjd} + \sum_{kl} (ik|jl) t_{kalb} \right] \\
& + \frac{1}{2} \sum_{iaj\bar{b}} (t_{iaj\bar{b}}^D - t_{ibja}^D) \left[\sum_{\bar{c}\bar{d}} (\bar{a}\bar{c}|\bar{b}\bar{d}) t_{i\bar{c}\bar{j}\bar{d}} + \sum_{\bar{k}\bar{l}} (\bar{i}\bar{k}|\bar{j}\bar{l}) t_{\bar{k}\bar{a}\bar{l}\bar{b}} \right] \\
& + \sum_{iaj\bar{b}} t_{iaj\bar{b}}^D \left[\sum_{\bar{c}\bar{d}} (ac|\bar{b}\bar{d}) t_{i\bar{c}\bar{j}\bar{d}} + \sum_{\bar{k}\bar{l}} (ik|\bar{j}\bar{l}) t_{\bar{k}\bar{a}\bar{l}\bar{b}} \right] \tag{A.26}
\end{aligned}$$

$$\begin{aligned}
T_6^{(2)} = & \frac{1}{2} \sum_{ac} D_{ac} \sum_{ijb} v_{iajb} (t_{icjb} - t_{ibjc}) - \frac{1}{2} \sum_{ik} D_{ki} \sum_{ajb} v_{iajb} (t_{kajb} - t_{kbja}) \\
& + \frac{1}{2} \sum_{\bar{a}\bar{c}} D_{\bar{a}\bar{c}} \sum_{\bar{i}\bar{j}\bar{b}} v_{\bar{i}\bar{a}\bar{j}\bar{b}} (t_{\bar{i}\bar{c}\bar{j}\bar{b}} - t_{\bar{i}\bar{b}\bar{j}\bar{c}}) - \frac{1}{2} \sum_{\bar{i}\bar{k}} D_{\bar{k}\bar{i}} \sum_{\bar{a}\bar{j}\bar{b}} v_{\bar{i}\bar{a}\bar{j}\bar{b}} (t_{\bar{k}\bar{a}\bar{j}\bar{b}} - t_{\bar{a}\bar{k}\bar{b}\bar{j}}) \\
& + \sum_{ac} D_{ac} \sum_{ij\bar{b}} v_{iaj\bar{b}} t_{icj\bar{b}} - \sum_{ik} D_{ki} \sum_{aj\bar{b}} v_{iaj\bar{b}} t_{ka\bar{j}\bar{b}} \\
& + \sum_{\bar{b}\bar{c}} D_{\bar{b}\bar{c}} \sum_{ia\bar{j}} v_{iaj\bar{b}} t_{ia\bar{j}\bar{c}} - \sum_{\bar{j}\bar{k}} D_{\bar{k}\bar{j}} \sum_{ia\bar{b}} v_{iaj\bar{b}} t_{ia\bar{k}\bar{b}} \tag{A.27}
\end{aligned}$$

Here, some additional t-amplitudes t_{ia}^D and t_{iajb}^D have been introduced which are defined as

$$t_{ia}^D = \frac{\sum_c v_{ic} D_{ca} - \sum_k D_{ik} v_{ka}}{\epsilon_a - \epsilon_i} \tag{A.28}$$

$$t_{iajb}^D = \frac{v_{ia} D_{jb} + D_{ia} v_{jb}}{\epsilon_a - \epsilon_i + \epsilon_b - \epsilon_j} \tag{A.29}$$

In contrast to the initial t-amplitudes the new ones depend on the eigenvectors of the ADC matrix.

A.4 Restricted ADC Equations

For restricted calculations the previous ADC equations simplify drastically by introducing new vectors \mathbf{V}^S , \mathbf{V}^T and \mathbf{V}^Q for singlet, triplet and quintet states respectively. How to do so has been described in section 3.3.2. This yields a set of restricted ADC equations for each type of state which are compiled below. For each type the matrix-vector product with the ADC matrix is given first, followed by the equations to calculate the transition moment T for an eigenvector \mathbf{V} and a transition operator \mathbf{D} .

- Singlet states:

$$\begin{aligned}
R_{ia}^S &= (\epsilon_a - \epsilon_i) V_{ia}^S + \sum_{bj} (2(ia|jb) - (ij|ab)) V_{jb}^S \\
&+ \sum_b \tilde{v}_{ab} V_{ib}^S + \sum_j \tilde{v}_{ij} V_{ja}^S \\
&- \frac{1}{2} \sum_{jb} [2t_{iajb} - t_{ibja}] \tilde{v}_{jb}^{(1)S} - \frac{1}{2} \sum_{jb} [2(ia|jb) - (ib|ja)] \tilde{v}_{jb}^{(2)S} \\
&+ \sum_{kcl} (ik|lc) (2V_{kalc}^S - V_{kclda}^S) + \sum_{ckd} (2V_{ickd}^S - V_{idkc}^S) (ac|kd) \quad (\text{A.30})
\end{aligned}$$

with

$$\tilde{v}_{ab} = \frac{1}{2} \sum_{kcl} [(2t_{kalc} - t_{kclda}) (kb|lc) + (2t_{kblc} - t_{kclb}) (ka|lc)] \quad (\text{A.31})$$

$$\tilde{v}_{ij} = \frac{1}{2} \sum_{ckd} [(2t_{ickd} - t_{idkc}) (jc|kd) + (2t_{jckd} - t_{jdkc}) (ic|kd)] \quad (\text{A.32})$$

$$\tilde{v}_{ia}^{(1)S} = \sum_{jb} (2(ia|jb) - (ib|ja)) V_{jb}^S \quad (\text{A.33})$$

$$\tilde{v}_{ia}^{(2)S} = \sum_{jb} (2t_{iajb} - t_{ibja}) V_{jb}^S \quad (\text{A.34})$$

$$\begin{aligned}
R_{iajb}^S &= (\epsilon_a - \epsilon_i + \epsilon_b - \epsilon_j) V_{iajb}^S \\
&+ \sum_k [V_{ka}^S (ik|jb) + (ia|jk) V_{kb}^S] - \sum_c [V_{ic}^S (ac|jb) + (ia|bc) V_{jc}^S] \\
&+ \sum_{cd} V_{icjd}^S (ac|bd) + \sum_{kl} (ik|jl) V_{kalb}^S \\
&+ \sum_{kc} (ia|kc) (2V_{jbkc}^S - V_{jckb}^S) + \sum_{kc} (2V_{iakc}^S - V_{icka}^S) (jb|kc) \\
&- \sum_{kc} [(ik|ac) V_{jbkc}^S + (jk|ac) V_{ickb}^S + (ik|bc) V_{kajc}^S + (jk|bc) V_{iakc}^S] \quad (A.35)
\end{aligned}$$

$$\begin{aligned}
T &= 2 \sum_{ia} D_{ia} V_{ia}^S - 2 \sum_{ia} V_{ia}^S \sum_{jb} (2t_{iajb} - t_{ibja}) D_{jb} \\
&+ \sum_{ia} V_{ia}^S \left[\sum_{jb} (2t_{iajb} - t_{ibja}) \sum_{kc} (2t_{iakc} - t_{icka}) D_{kc} \right] \\
&- \sum_{ac} \left(\sum_i V_{ia}^S D_{ci} \right) \sum_{kjb} t_{kajb} (2t_{kcjb} - t_{kbjc}) \\
&- \sum_{ik} \left(\sum_a V_{ia}^S D_{ka} \right) \sum_{bcj} t_{ibjc} (2t_{kbjc} - t_{kcjb}) \\
&+ 2 \sum_{ia} t_{ia}^D \left[\sum_{cjb} (2t_{icjb} - t_{ibjc}) (ac|jb) - \sum_{kjb} (ki|jb) (2t_{kajb} - t_{kbja}) \right] \\
&+ 2 \sum_{iajb} t_{iajb}^D \sum_{kc} (2t_{iakc} - t_{icka}) (2(jb|kc) - (jk|bc)) \\
&- 2 \sum_{iajb} t_{iajb}^D \sum_{kc} [(ib|kc) (2t_{jakc} - t_{jcka}) + (ik|bc) (2t_{kajc} - t_{kcja})] \\
&+ \sum_{iajb} t_{iajb}^D \left[\sum_{cd} (2t_{icjd} - t_{idjc}) (ac|bd) + \sum_{kl} (ik|jl) (2t_{kalb} - t_{kbla}) \right] \\
&+ 2 \sum_{ac} D_{ac} \sum_{ibj} V_{iajb}^S (2t_{cibj} - t_{cjb i}) \\
&- 2 \sum_{ik} D_{ik} \sum_{ajb} V_{iajb}^S (2t_{kajb} - t_{kbja}) \quad (A.36)
\end{aligned}$$

- Triplet states:

$$\begin{aligned}
R_{ia}^T &= (\epsilon_a - \epsilon_i) V_{ia}^T - \sum_{jb} (ij|ab) V_{jb}^T \\
&+ \sum_b \tilde{v}_{ab} V_{ib}^T + \sum_j \tilde{v}_{ij} V_{ja}^T + \frac{1}{2} \sum_{jb} t_{ibja} \tilde{v}_{jb}^{(1)T} + \frac{1}{2} \sum_{jb} (ib|ja) \tilde{v}_{jb}^{(2)T} \\
&+ \sum_{kcl} (ik|lc) (2V_{kalc}^T - V_{kcla}^T - V_{lckc}^T) \\
&+ \sum_{ckd} (2V_{ickd}^T - V_{idkc}^T - V_{kcid}^T) (ac|kd)
\end{aligned} \tag{A.37}$$

with \tilde{v}_{ab} and \tilde{v}_{ij} being the same as for singlet states, and

$$\tilde{v}_{ia}^{(1)T} = - \sum_{jb} (ib|ja) V_{jb}^T \quad \tilde{v}_{ia}^{(2)T} = - \sum_{jb} t_{ibja} V_{jb}^T \tag{A.38}$$

$$\begin{aligned}
R_{iajb}^T &= (\epsilon_a - \epsilon_i + \epsilon_b - \epsilon_j) V_{iajb}^T + \sum_k V_{ka}^T (ik|jb) - \sum_c V_{ic}^T (ac|jb) \\
&+ \sum_{cd} V_{icjd}^T (ac|bd) + \sum_{kl} (ik|jl) V_{kalb}^T \\
&+ \sum_{kc} (2V_{iakc}^T - V_{icka}^T - V_{kaic}^T) (jb|kc) \\
&- \sum_{kc} [V_{iakc}^T (jk|bc) + (ik|bc) V_{kajc}^T + V_{ickb}^T (jk|ac) + (ik|ac) V_{kcjb}^T]
\end{aligned} \tag{A.39}$$

$$T = 0 \tag{A.40}$$

- Quintet states:

$$\begin{aligned}
R_{iajb}^Q &= (\epsilon_a - \epsilon_i + \epsilon_b - \epsilon_j) V_{iajb}^Q \\
&+ \sum_{cd} V_{icjd}^Q (ac|bd) + \sum_{kl} (ik|jl) V_{kalb}^Q \\
&- \sum_{kc} [V_{iakc}^Q (jk|bc) + (ik|bc) V_{kajc}^Q + V_{ickb}^Q (jk|ac) + (ik|ac) V_{kcjb}^Q]
\end{aligned} \tag{A.41}$$

$$T = 0 \tag{A.42}$$

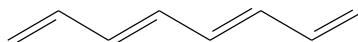
Appendix B

Molecular Parameters

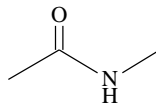
B.1 Molecules Employed in Section 4.2.2

During the evaluation and testing of the minimal bumping scheme for local ADC several molecules have been employed. The structures and geometrical parameters of all molecules are listed in the following. Positions and distances are given in Ångström, angles in degrees.

1. Octatetraene:

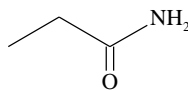


C							cc1 = 1.454611
C	1	cc1					cc2 = 1.335497
C	1	cc2	2	ccc1			cc3 = 1.458948
C	2	cc2	1	ccc1	3	180.0	cc4 = 1.328848
C	3	cc3	1	ccc2	2	180.0	ccc1 = 124.327
C	4	cc3	2	ccc2	1	180.0	ccc2 = 124.134
C	5	cc4	3	ccc3	1	180.0	ccc3 = 124.473
C	6	cc4	4	ccc3	2	180.0	hc1 = 1.077409
H	1	hc1	2	hcc1	4	0.0	hc2 = 1.077310
H	2	hc1	1	hcc1	3	0.0	hc3 = 1.076870
H	3	hc2	1	hcc2	2	0.0	hc4 = 1.072368
H	4	hc2	2	hcc2	1	0.0	hc5 = 1.074780
H	5	hc3	3	hcc3	1	0.0	hcc1 = 116.470
H	6	hc3	4	hcc3	2	0.0	hcc2 = 119.396
H	7	hc4	5	hcc4	3	180.0	hcc3 = 116.186
H	8	hc4	6	hcc4	4	180.0	hcc4 = 121.780
H	7	hc5	5	hcc5	3	0.0	hcc5 = 121.846
H	8	hc5	6	hcc5	4	0.0	

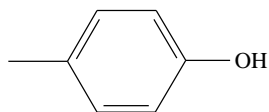
2. *N*-methylacetamide:

C					cc = 1.515		
C	1	cc			nc = 1.363		
N	1	nc	2	ncc	cn = 1.45		
C	3	cn	1	cnc	2	180.0	oc = 1.232
O	1	oc	3	ocn	4	0.0	ncc = 115.1
H	3	hn	1	hnc	2	0.0	cnc = 120.4
H	2	hc1	1	hcc1	3	0.0	onc = 121.6
H	2	hc2	1	hcc2	2	0.0	hm1 = 1.01
H	2	hc2	2	hcc2	1	0.0	hc1 = 1.089
H	4	hc3	3	hcn1	1	180.0	hc2 = 1.094
H	4	hc4	3	hcn2	1	dih	hc3 = 1.09
H	4	hc4	3	hcn2	1	-dih	hc4 = 1.093
							hnc = 119.9
							hcc1 = 108.9
							hcc2 = 110.9
							hcn1 = 108.7
							hcn2 = 110.7
							dih = 59.9

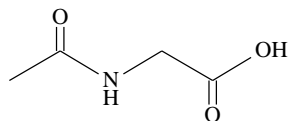
3. Propanamide:



C					cc = 1.52		
C	1	cc			nc = 1.367		
C	2	cc	1	ccc		oc = 1.229	
N	1	nc	2	ncc	3	180.0	ccc = 112.1
O	1	oc	2	occ	3	0.0	ncc = 114.7
H	4	hn1	1	hnc1	2	0.0	occ = 123.2
H	4	hn2	1	hnc2	2	180.0	hm1 = 1.01
H	2	hc1	1	hcc1	4	dih1	hn2 = 1.008
H	2	hc1	1	hcc1	4	-dih1	hc1 = 1.097
H	3	hc2	2	hcc2	1	180.0	hc2 = 1.093
H	3	hc3	2	hcc3	1	dih2	hc3 = 1.091
H	3	hc3	2	hcc3	1	-dih2	hnc1 = 118.3
							hnc2 = 122.8
							hcc1 = 108.5
							hcc2 = 110.5
							hcc3 = 110.6
							dih1 = 57.4
							dih2 = 59.5

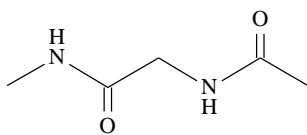
4. *P*-cresol:

C	1.467515	-0.043327	0.000000
C	0.798423	1.181968	0.000000
C	-0.597475	1.213463	0.000000
C	-1.354023	0.037893	0.000000
C	-0.658457	-1.181992	0.000000
C	0.731686	-1.233352	0.000000
O	2.835035	-0.138343	0.000000
C	-2.865419	0.070913	0.000000
H	1.367770	2.110650	0.000000
H	-1.100982	2.177263	0.000000
H	-1.218741	-2.114913	0.000000
H	1.262127	-2.180587	0.000000
H	3.203921	0.757936	0.000000
H	-3.241005	1.098921	0.000000
H	-3.281077	-0.433214	-0.881748
H	-3.281077	-0.433214	0.881748

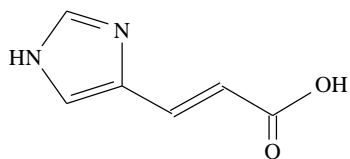
5. *N*-acetylglycine:

C					cc1 = 1.512
C	1	cc1			cc2 = 1.505
N	1	nc	2	ncc	nc = 1.363
C	3	cn	1	cnc	cn = 1.438
C	4	cc2	3	cen	1 180.0
O	1	oc1	3	ocn	4 0.0
O	5	oc2	4	occ1	3 0.0
O	5	oc3	4	occ2	3 180.0
H	2	hc1	1	hec1	2 120.0
H	2	hc1	1	hec1	2 -120.0
H	2	hc2	1	hec2	4 0.0
H	3	hn	1	hnc	4 180.0
H	4	hc3	3	hcn	1 dih
H	4	hc3	3	hcn	1 -dih
H	8	ho	5	hoc	1 0.0
					cc1 = 1.512
					cc2 = 1.505
					nc = 1.363
					cn = 1.438
					oc1 = 1.233
					oc2 = 1.219
					oc3 = 1.351
					ncc = 115.0
					cnc = 120.2
					cen = 109.0
					occ1 = 125.3
					occ2 = 111.1
					hc1 = 1.094
					hc2 = 1.089
					hc3 = 1.096
					hn = 1.013
					ho = 0.980
					hec1 = 110.8
					hec2 = 108.5
					hnc = 122.6
					hcn = 111.7
					hoc = 106.1
					dih = 59.3

6. Model dipeptide:

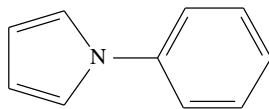


C	3.743342	-0.100497	0.000000
N	2.449284	0.558113	0.000000
C	1.307099	-0.168063	0.000000
C	0.019706	0.643092	0.000000
N	-1.088345	-0.271668	0.000000
C	-2.367765	0.187502	0.000000
C	-3.432619	-0.887758	0.000000
O	-2.621269	1.395475	0.000000
O	1.307520	-1.403377	0.000000
H	-0.848192	-1.257343	0.000000
H	2.400020	1.567470	0.000000
H	4.520895	0.662985	0.000000
H	3.853930	-0.730455	0.885236
H	3.853930	-0.730455	-0.885236
H	-0.014658	1.299699	0.879213
H	-0.014658	1.299699	-0.879213
H	-4.410041	-0.407191	0.000000
H	-3.341121	-1.523979	-0.884770
H	-3.341121	-1.523979	0.884770

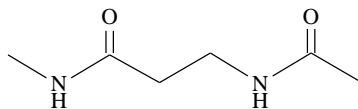
7. *Trans*-urocanic acid:

N	0.000000	0.000000	0.000000
H	1.010901	0.000000	0.000000
C	-0.675088	1.186968	0.000000
O	-1.907028	1.233085	0.000000
C	-0.716828	-1.266803	0.000000
H	-1.368701	-1.328190	-0.875815
H	-1.368701	-1.328190	0.875815
C	0.203217	2.423460	0.000000
H	-0.440308	3.302693	0.000000
H	0.844663	2.446107	0.886203
H	0.844663	2.446107	-0.886203
C	0.279237	-2.415695	0.000000
H	0.930136	-2.354420	-0.882330
H	0.930136	-2.354420	0.882330
C	-0.430332	-3.762634	0.000000
O	-1.659089	-3.870825	0.000000
N	0.389460	-4.850109	0.000000
H	1.391618	-4.724921	0.000000
C	-0.167642	-6.191594	0.000000
H	0.653670	-6.909101	0.000000
H	-0.788049	-6.350316	0.885238
H	-0.788049	-6.350316	-0.885238

8. 1-phenylpyrrole:

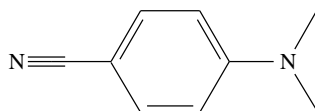


C	0.000000	0.000000	0.000000
C	0.000000	0.000000	1.372000
N	1.303536	0.000000	1.815760
C	2.136069	0.000000	0.718938
C	1.368856	0.000000	-0.418501
C	1.716073	0.000000	3.165106
C	2.793158	0.794846	3.571687
C	3.199552	0.793244	4.907223
C	2.536418	0.000342	5.846994
C	1.050486	-0.794846	4.104476
C	1.460392	-0.793244	5.438938
H	-0.875138	0.000000	-0.631169
H	1.741433	0.000000	-1.431135
H	-0.815753	0.000000	2.073658
H	3.204721	0.000000	0.844476
H	3.308136	1.409073	2.847863
H	0.218792	-1.409073	3.792370
H	4.034741	1.412883	5.209543
H	0.937044	-1.412883	6.156604
H	2.852764	0.000342	6.881715

9. Model β -dipeptide:

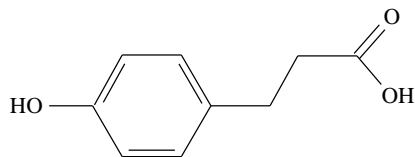
N	0.000000	0.000000	0.000000
H	0.000000	0.000000	1.010901
C	1.186968	0.000000	-0.675088
O	1.233085	0.000000	-1.907028
C	-1.266803	0.000000	-0.716828
H	-1.328190	-0.875815	-1.368701
H	-1.328190	0.875815	-1.368701
C	2.423460	0.000000	0.203217
H	3.302693	0.000000	-0.440308
H	2.446107	0.886203	0.844663
H	2.446107	-0.886203	0.844663
C	-2.415695	0.000000	0.279237
H	-2.354420	-0.882330	0.930136
H	-2.354420	0.882330	0.930136
C	-3.762634	0.000000	-0.430332
O	-3.870825	0.000000	-1.659089
N	-4.850109	0.000000	0.389460
H	-4.724921	0.000000	1.391618
C	-6.191594	0.000000	-0.167642
H	-6.909101	0.000000	0.653670
H	-6.350316	0.885238	-0.788049
H	-6.350316	-0.885238	-0.788049

10. 4-dimethylaminobenzonitrile (DMABN):



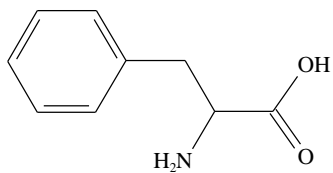
C	1.921221	0.000040	0.000000
C	1.201416	1.207464	0.000000
C	-0.183978	1.211445	0.000000
C	-0.920526	-0.000023	0.000000
C	1.201469	-1.207416	0.000000
C	-0.183025	-1.211456	0.000000
C	3.350221	0.000071	0.000000
N	4.514921	0.000098	0.000000
N	-2.297326	-0.000053	0.000000
C	-3.027748	1.257398	0.000000
C	-3.027693	-1.257535	0.000000
H	1.745441	2.156682	0.000000
H	-0.701439	2.172035	0.000000
H	1.745655	-2.156544	0.000000
H	-0.700556	-2.172042	0.000000
H	-4.103530	1.042250	0.000000
H	-2.797367	1.865442	-0.893738
H	-2.797367	1.865442	0.893738
H	-4.103495	-1.042483	0.000000
H	-2.797286	-1.865571	-0.893738
H	-2.797286	-1.865571	0.893738

11. 3-(4-hydroxy-phenyl)propionic acid (HPA):



C	3.378254	-0.115436	-0.522434
C	1.903468	0.201748	-0.616496
C	1.069571	-0.635452	0.389590
C	-0.413273	-0.357042	0.278083
C	-1.001631	0.714412	0.966871
C	-2.357255	1.002715	0.845577
C	-3.162672	0.210701	0.020107
C	-2.597770	-0.862995	-0.674104
C	-1.236437	-1.136715	-0.541242
O	3.928008	0.385457	0.616351
O	4.022562	-0.759140	-1.320676
O	-4.490698	0.530450	-0.061242
H	1.749962	1.267223	-0.412944
H	1.582308	-0.007308	-1.639762
H	1.265082	-1.698677	0.205397
H	1.422337	-0.416616	1.403537
H	-0.386243	1.333518	1.616790
H	-2.809194	1.829400	1.384499
H	-3.220301	-1.486939	-1.313773
H	-0.812251	-1.978783	-1.083727
H	4.861445	0.101246	0.608793
H	-4.929232	-0.100565	-0.652994

12. Phenylalanine:



C	2.852675	-0.006657	0.069363
C	1.374675	0.283748	0.299174
C	0.456611	-0.704720	-0.465236
C	-1.007867	-0.339735	-0.347585
C	-1.619792	0.468882	-1.315745
C	-2.963712	0.828482	-1.207228
C	-3.721251	0.383540	-0.122513
C	-3.124665	-0.422009	0.849513
C	-1.780271	-0.780383	0.737540
O	3.145585	-0.212039	-1.236855
O	3.702629	-0.009678	0.933109
N	1.113835	0.226049	1.732270
H	1.214819	1.285816	-0.144141
H	0.754931	-0.719391	-1.517731
H	0.630303	-1.703565	-0.050145
H	-1.319301	-1.406601	1.496703
H	-3.708587	-0.777984	1.694617
H	-4.769559	0.657135	-0.037420
H	-3.419669	1.450076	-1.973691
H	-1.038609	0.812783	-2.168933
H	0.295661	0.783614	1.960345
H	1.912649	0.599736	2.239297
H	4.110737	-0.349844	-1.274852

Bibliography

- [1] *Photosynthesis: From Light to Biosphere*, ed. P. Mathis, Kluwer Academic Pub., 1996.
- [2] D.-P. Häder, *Photosynthese*, Georg Thieme Verlag, Stuttgart, Germany, 1999.
- [3] *Handbook of Photosensory Receptors*, ed. W. R. Briggs and J. L. Spudich, Wiley-VCH, Weinheim, Germany, 2005.
- [4] H.-J. Timpe, in *Photoinduced Electron Transfer I*, Springer, Berlin / Heidelberg, 2006, vol. 156, pp. 167–197.
- [5] A. Wrzyszczyński, P. Filipiak, G. L. Hug, B. Marciniak and J. Pączkowski, *Macromolecules*, 2000, **33**, 1577–1582.
- [6] A. Boulesbaa, A. Issac, D. Stockwell, Z. Huang, J. Huang, J. Guo and T. Lian, *J. Am. Chem. Soc.*, 2007, **129**, 15132–15133.
- [7] A. H. Zewail, F. C. de Schryver, S. De Feyter and G. Schweitzer, *Femtochemistry*, Wiley-VCH, 2001.
- [8] M. A. Kahlow, W. Jarzęba, T. P. DuBruil and P. F. Barbara, *Rev. Sci. Instr.*, 1988, **59**, 1098–1109.
- [9] S. Akimoto, S. Takaichi, T. Ogata, Y. Nishimura, I. Yamazaki and M. Mimuro, *Chem. Phys. Lett.*, 1996, **260**, 147–152.
- [10] M. Chachisvilis and V. Sundström, *Chem. Phys. Lett.*, 1998, **261**, 165–174.
- [11] C. Wan, T. Fiebig, S. O. Kelley, C. R. Treadway, J. K. Barton and A. H. Zewail, *Proc. Natl. Acad. Sci. U.S.A.*, 1999, **96**, 6014–6019.

- [12] R. Croce, M. G. Müller, R. Bassi and A. R. Holzwarth, *Biophys. J.*, 2001, **80**, 901–915.
- [13] L. Lorenz, J. Plötner, V. Matylitsky, A. Dreuw and J. Wachtveitl, *J. Phys. Chem. A*, 2007, **111**, 10891–10898.
- [14] M. O. Lenz and J. Wachtveitl, *J. Phys. Chem. C*, 2008, **112**, 11973–11977.
- [15] M. Ricci, S. E. Bradforth, R. Jimenez and G. R. Fleming, *Chem. Phys. Lett.*, 1996, **259**, 381–390.
- [16] T. Polivka, J. L. Herek, D. Zigmantas, H.-E. Åkerlund and V. Sundström, *Proc. Nat. Acad. Sci. USA*, 1999, **96**, 4914–4917.
- [17] V. Sundström, T. Pullerits and R. van Grondelle, *J. Phys. Chem. B*, 1999, **103**, 2327–2346.
- [18] C. C. Gradinaru, J. T. M. Kennis, E. Papagiannakis, I. H. M. van Stokkum, R. J. Cogdell, G. R. Fleming, R. A. Niederman and R. van Grondelle, *Proc. Natl. Acad. Sci. U.S.A.*, 2001, **38**, 2364–2369.
- [19] Z. He, V. Sundström and T. Pullerits, *J. Phys. Chem. B*, 2002, **106**, 11606–11612.
- [20] J. E. Ridley and M. C. Zerner, *Theor. Chim. Acta*, 1973, **32**, 111–134.
- [21] M. Kotzian, N. Rösch and M. C. Zerner, *Theor. Chim. Acta*, 1992, **81**, 201–222.
- [22] W. Weber and W. Thiel, *Theor. Chem. Acc.*, 2000, **103**, 495–506.
- [23] J. del Bene, R. Ditchfield and J. A. Pople, *J. Chem. Phys.*, 1971, **55**, 2236–2241.
- [24] J. B. Foresman, M. Head-Gordon, J. A. Pople and M. J. Frisch, *J. Phys. Chem.*, 1992, **96**, 135–149.
- [25] A. L. Fetter and J. D. Walecka, *Quantum Theory of Many-Particle Systems*, McGraw-Hill, New York, 1971.

- [26] D. Hegarthy and M. A. Robb, *Mol. Phys.*, 1979, **38**, 1795–1812.
- [27] R. H. E. Eade and M. A. Robb, *Chem. Phys. Lett.*, 1981, **83**, 362–368.
- [28] E. Runge and E. K. U. Gross, *Phys. Rev. Lett.*, 1984, **52**, 997–1000.
- [29] M. E. Casida, in *Recent Advances in Density Functional Methods, Part I*, ed. D. P. Chong, World Scientific, Singapore, 1995, pp. 155–192.
- [30] T. Korona and H.-J. Werner, *J. Chem. Phys.*, 2003, **118**, 3006–3019.
- [31] D. Kats, T. Korona and M. Schütz, *J. Chem. Phys.*, 2006, **125**, 104106.
- [32] P. Hohenberg and W. Kohn, *Phys. Rev.*, 1964, **136**, B864–B871.
- [33] W. Kohn and L. J. Sham, *Phys. Rev.*, 1965, **140**, A1133–A1138.
- [34] R. G. Parr and W. Yang, *Density-Functional Theory of Atoms and Molecules*, Oxford Science Publication, New York, 1989.
- [35] A. D. Becke, *Phys. Rev. A*, 1988, **38**, 3098–3100.
- [36] A. D. Becke, *J. Chem. Phys.*, 1993, **98**, 5648–5652.
- [37] C. Lee, W. Yang and R. G. Parr, *Phys. Rev. B*, 1988, **37**, 785–789.
- [38] J. P. Perdew, *Phys. Rev. B*, 1986, **33**, 8822–8824.
- [39] C. Møller and M. S. Plesset, *Phys. Rev.*, 1934, **46**, 618–622.
- [40] E. Schrödinger, *Ann. d. Phys.*, 1926, **385**, 437–490.
- [41] R. K. Nesbet, *Proc. Roy. Soc. A*, 1955, **320**, 312–321.
- [42] P.-O. Löwdin, *Adv. Chem. Phys.*, 1959, **2**, 207–322.
- [43] A. Szabo and N. S. Ostlund, *Modern Quantum Chemistry*, MacMillan Publishing, 1982.
- [44] J. A. Pople, J. S. Binkley and R. Seeger, *Int. J. Quant. Chem. Symp.*, 1976, **10**, 1–19.

- [45] E. K. U. Gross and W. Kohn, *Phys. Rev. Lett.*, 1985, **55**, 2850–2852.
- [46] E. K. U. Gross and W. Kohn, *Adv. Quant. Chem.*, 1990, **21**, 255–291.
- [47] E. R. Davidson, *J. Comp. Phys.*, 1975, **17**, 87–94.
- [48] A. Dreuw and M. Head-Gordon, *Chem. Rev.*, 2005, **105**, 4009–4037.
- [49] S. Hirata, M. Head-Gordon and R. J. Bartlett, *J. Chem. Phys.*, 1999, **111**, 10774–10786.
- [50] M. Head-Gordon, R. J. Rico, M. Oumi and T. J. Lee, *Chem. Phys. Lett.*, 1994, **219**, 21–29.
- [51] J. Schirmer and A. Dreuw, *Phys. Rev. A*, 2007, **75**, 022513.
- [52] S. Hirata and M. Head-Gordon, *Chem. Phys. Lett.*, 1999, **302**, 375–382.
- [53] S. Hirata and M. Head-Gordon, *Chem. Phys. Lett.*, 1999, **314**, 291–299.
- [54] C.-P. Hsu, S. Hirata and M. Head-Gordon, *J. Phys. Chem. A*, 2001, **105**, 451–458.
- [55] A. Dreuw, G. R. Fleming and M. Head-Gordon, *J. Phys. Chem. B*, 2003, **107**, 6500–6503.
- [56] A. Dreuw, G. R. Fleming and M. Head-Gordon, *Phys. Chem. Chem. Phys.*, 2003, **5**, 3247–3256.
- [57] S. Grimme, *Rev. Comp. Chem.*, 2004, **20**, 153–218.
- [58] M. W. Casida, C. Jamorski, K. C. Casida and D. R. Salahub, *J. Chem. Phys.*, 1998, **108**, 4439–4449.
- [59] R. J. Cave, F. Zhang, N. T. Maitra and K. Burke, *Chem. Phys. Lett.*, 2004, **389**, 39–42.
- [60] N. T. Maitra, F. Zhang, R. J. Cave and K. Burke, *J. Chem. Phys.*, 2004, **120**, 5932–5937.

- [61] J. H. Starcke, M. Wormit, J. Schirmer and A. Dreuw, *Chem. Phys.*, 2006, **329**, 39–49.
- [62] D. J. Tozer, R. D. Amos, N. C. Handy, B. J. Roos and L. Serrano-Andrés, *Mol. Phys.*, 1999, **97**, 859–868.
- [63] A. Dreuw, J. L. Weisman and M. Head-Gordon, *J. Chem. Phys.*, 2003, **119**, 2943–2946.
- [64] A. Dreuw and M. Head-Gordon, *J. Am. Chem. Soc.*, 2004, **126**, 4007–4016.
- [65] A. Görling, *Phys. Rev. Lett.*, 1999, **83**, 5459–5462.
- [66] S. Ivanov, S. Hirata and R. J. Bartlett, *Phys. Rev. Lett.*, 1999, **83**, 5455–5458.
- [67] Y. Tawada, T. Tsuneda, S. Yanagisawa, T. Yanai and K. Hirao, *J. Chem. Phys.*, 2004, **120**, 8425–8433.
- [68] T. Yanai, D. P. Tew and N. C. Handy, *Chem. Phys. Lett.*, 2004, **393**, 51–57.
- [69] R. Baer and D. Neuhauser, *Phys. Rev. Lett.*, 2005, **94**, 043002.
- [70] T. Ziegler, A. Rauk and E. J. Baerends, *Theo. Chim. Acta*, 1977, **43**, 261–271.
- [71] J. Schirmer, *Phys. Rev. A*, 1982, **26**, 2395–2416.
- [72] A. B. Trofimov and J. Schirmer, *J. Phys. B*, 1995, **28**, 2299.
- [73] J. Schirmer and F. Mertins, *Int. J. Quant. Chem.*, 1996, **58**, 329.
- [74] A. B. Trofimov, G. Stelter and J. Schirmer, *J. Chem. Phys.*, 2002, **117**, 6402–6410.
- [75] A. Abrikosov, L. P. Gorkov and I. E. Dzyaloshinski, *Methods of Quantum Field Theory in Statistical Physics*, Prentice-Hall, Englewood Cliffs, NJ, 1963.
- [76] J. Schirmer, *Phys. Rev. A*, 1991, **43**, 4647–4659.

- [77] Y. Shao, L. F. Molnar, Y. Jung, J. Kussmann, C. Ochsenfeld, S. T. Brown, A. T. Gilbert, L. V. Slipchenko, S. V. Levchenko, D. P. O'Neill, R. A. D. Jr, R. C. Lochan, T. Wang, G. J. Beran, N. A. Besley, J. M. Herbert, C. Y. Lin, T. V. Voorhis, S. H. Chien, A. Sodt, R. P. Steele, V. A. Rassolov, P. E. Maslen, P. P. Korambath, R. D. Adamson, B. Austin, J. Baker, E. F. C. Byrd, H. Dachsel, R. J. Doerksen, A. Dreuw, B. D. Dunietz, A. D. Dutoi, T. R. Furlani, S. R. Gwaltney, A. Heyden, S. Hirata, C.-P. Hsu, G. Kedziora, R. Z. Khalliulin, P. Klunzinger, A. M. Lee, M. S. Lee, W. Liang, I. Lotan, N. Nair, B. Peters, E. I. Proynov, P. A. Pieniazek, Y. M. Rhee, J. Ritchie, E. Rosta, C. D. Sherrill, A. C. Simmonett, J. E. Subotnik, H. L. W. III, W. Zhang, A. T. Bell and A. K. Chakraborty, *Phys. Chem. Chem. Phys.*, 2006, **8**, 3172–3191.
- [78] D. van Heesch, *Doxygen*, <http://www.doxygen.org>.
- [79] M. Feyereisen, G. Fitzgerald and A. Komornicki, *Chem. Phys. Lett.*, 1993, **208**, 359–363.
- [80] R. A. Kendall and H. A. Früchtl, *Theor. Chem. Acc.*, 1997, **97**, 158–163.
- [81] P. Pulay, *Chem. Phys. Lett.*, 1983, **100**, 151–154.
- [82] S. Sæbø and P. Pulay, *Chem. Phys. Lett.*, 1985, **113**, 13–18.
- [83] P. Pulay and S. Sæbø, *Theor. Chim. Acta*, 1986, **69**, 357–368.
- [84] S. Sæbø and P. Pulay, *J. Chem. Phys.*, 1987, **86**, 914–922.
- [85] G. Hetzer, P. Pulay and J.-H. Werner, *Chem. Phys. Lett.*, 1998, **290**, 143–149.
- [86] M. Schütz, G. Hetzer and H.-J. Werner, *J. Chem. Phys.*, 1999, **111**, 5691–5705.
- [87] M. Schütz and H.-J. Werner, *J. Chem. Phys.*, 2001, **114**, 661–681.
- [88] H.-J. Werner, F. R. Manby and P. J. Knowles, *J. Chem. Phys.*, 2003, **118**, 8149–8160.

- [89] S. F. Boys, *Rev. Mod. Phys.*, 1960, **32**, 296–299.
- [90] S. F. Boys, in *Quantum Theory of Atoms, Molecules and the Solid State*, ed. P. O. Löwdin, Academic, New York, 1966, pp. 253–262.
- [91] C. Edmiston and K. Ruedenberg, *Rev. Mod. Phys.*, 1963, **35**, 457–464.
- [92] J. Pipek and P. G. Mezey, *J. Chem. Phys.*, 1989, **90**, 4916–4926.
- [93] J. E. Subotnik, A. D. Dutoi and M. Head-Gordon, *J. Chem. Phys.*, 2005, **123**, 114108.
- [94] J. Almlöf, *Chem. Phys. Lett.*, 1991, **181**, 319–320.
- [95] P. Y. Ayala and G. E. Scuseria, *J. Chem. Phys.*, 1999, **110**, 3660–3671.
- [96] J. E. Subotnik and M. Head-Gordon, *J. Chem. Phys.*, 2005, **123**, 064108.
- [97] J. E. Subotnik, A. Sodt and M. Head-Gordon, *J. Chem. Phys.*, 2006, **125**, 074116.
- [98] N. J. Russ and T. D. Crawford, *J. Chem. Phys.*, 2004, **121**, 691–696.
- [99] J. E. Subotnik, A. Sodt and M. Head-Gordon, *J. Chem. Phys.*, 2008, **128**, 034103.
- [100] *Light-harvesting Antennas in Photosynthesis*, ed. B. R. Green and W. W. Parson, Kluwer Academic Publisher, 2003, pp. 219–251.
- [101] Z. Liu, H. Yan, K. Wang, T. Kuang, J. Zhang, L. Gui, X. An and W. Chang, *Nature*, 2004, **428**, 287–292.
- [102] J. Standfuss, A. C. Terwisscha van Scheltinga, M. Lamborghini and W. Kühlbrandt, *EMBO J.*, 2005, **24**, 919–928.
- [103] S. M. Prince, M. Z. Papiz, A. A. Freer, G. McDermott, A. M. Hawthornthwaite-Lawless, R. J. Cogdell and N. W. Isaacs, *J. Mol. Biol.*, 1997, **268**, 412–423.
- [104] M. Z. Papiz, S. M. Prince, T. Howard, R. J. Cogdell and N. W. Isaacs, *J. Mol. Biol.*, 2003, **326**, 1523–1538.

- [105] J. Köpke, X. Hu, C. Münke, K. Schulten and H. Michel, *Structure*, 1996, **4**, 581–597.
- [106] E. Papagiannakis, J. T. M. Kennis, I. H. M. van Stokkum, R. J. Cogdell and R. van Grondelle, *Proc. Natl. Acad. Sci. U.S.A.*, 2002, **99**, 6017–6022.
- [107] T. Polívka, D. Zigmantas, J. L. Herek, Z. He, T. Pascher, T. Pullertis, R. J. Cogdell, H. A. Frank and V. Sundström, *J. Phys. Chem. B*, 2002, **106**, 11016–11025.
- [108] D. S. Larsen, E. Papagiannakis, I. H. M. van Stokkum, M. Vengris, J. T. M. Kennis and R. van Grondelle, *Chem. Phys. Lett.*, 2003, **381**, 733–742.
- [109] T. Polívka, T. Pullertis, H. A. Frank, R. J. Cogdell and V. Sundström, *J. Phys. Chem. B*, 2004, **108**, 15398–15407.
- [110] S. Amarie, J. Standfuss, T. Barros, W. Kühlbrandt, A. Dreuw and J. Wachtveitl, *J. Phys. Chem. B*, 2007, **111**, 3481–3487.
- [111] M. Wormit and A. Dreuw, *J. Phys. Chem. B*, 2006, **110**, 24200–24206.
- [112] J. Linnanto and J. Korppi-Tommola, *Phys. Chem. Chem. Phys.*, 2006, **8**, 663–687.
- [113] A. Damjanovic, H. M. Vaswani, P. Fromme and G. R. Fleming, *J. Phys. Chem. B*, 2002, **106**, 10251–10262.
- [114] V. I. Novoderezhkin, J. M. Salverda, H. van Amerongen and R. J. van Grondelle, *J. Phys. Chem. B*, 2003, **107**, 1893–1912.
- [115] V. I. Novoderezhkin, M. A. Palacios, H. van Amerongen and R. J. van Grondelle, *J. Phys. Chem. B*, 2004, **108**, 10363–10375.
- [116] A. A. Pascal, Z. Liu, K. Broess, B. van Oort, H. van Amerongen, C. Wang, P. Horton, B. Robert, W. Chang and A. Ruban, *Nature*, 2005, **436**, 134–137.
- [117] A. Dreuw, G. R. Fleming and M. Head-Gordon, *Biochem. Soc. Trans.*, 2005, **33**, 858–862.
- [118] M. Wormit and A. Dreuw, *Phys. Chem. Chem. Phys.*, 2007, **9**, 2917–2931.

- [119] A. Dreuw and M. Wormit, *J. Inorg. Biochem.*, 2008, **102**, 458–465.
- [120] A. Dreuw, *J. Phys. Chem. A*, 2006, **110**, 4592–4599.
- [121] G. McDermott, S. M. Prince, A. Freer, A. M. Hawthornewaite-Lawless, M. Z. Papiz, R. J. Cogdell and N. W. Isaacs, *Nature*, 1995, **374**, 517–521.
- [122] T. Walz, S. J. Jamieson, C. M. Bowers, P. A. Bullough and C. N. Hunter, *J. Mol. Biol.*, 1998, **282**, 833–845.
- [123] B. P. Krueger, J. Yom, P. J. Walla and G. R. Fleming, *Chem. Phys. Lett.*, 1999, **310**, 57–64.
- [124] B. P. Krueger, G. D. Scholes and G. R. Fleming, *J. Phys. Chem. B*, 1998, **102**, 5378–5386.
- [125] B. P. Krueger, G. D. Scholes, R. Jimenez and G. R. Fleming, *J. Phys. Chem. B*, 1998, **102**, 2284–2292.
- [126] R. Z. B. Desamero, V. Chynwat, I. van der Hoef, F. J. Jansen, J. Lugtenburg, D. Gosztola, M. R. Wasielewski, A. Cua, D. F. Bocian and H. A. Frank, *J. Phys. Chem. B*, 1998, **102**, 8151–8162.
- [127] P. O. Andersson, R. J. Cogdell and T. Gillbro, *Chem. Phys.*, 1996, **210**, 195–217.
- [128] J.-P. Zhang, R. Fujii, P. Qian, T. Inaba, T. Mizoguchi, Y. Koyama, K. Onaka, Y. Watanabe and H. Nagae, *J. Phys. Chem. B*, 2000, **104**, 3683–3691.
- [129] P. J. Walla, P. A. Linden, C.-P. Hsu, G. D. Scholes and G. R. Fleming, *Proc. Natl. Acad. Sci. U.S.A.*, 2000, **97**, 10808–10813.
- [130] C.-P. Hsu, P. J. Walla, M. Head-Gordon and G. R. Fleming, *J. Phys. Chem. B*, 2001, **105**, 11016–11025.
- [131] R. G. Alden, E. Johnson, V. Nagarajan, W. W. Parson, C. J. Law and R. G. Cogdell, *J. Phys. Chem. B*, 1997, **101**, 4667–4680.
- [132] G. D. Scholes, R. D. Harcourt and G. R. Fleming, *J. Phys. Chem. B*, 1997, **101**, 7302–7312.

- [133] G. D. Scholes, I. R. Gould, R. J. Cogdell and G. R. Fleming, *J. Phys. Chem. B*, 1999, **103**, 2543–2553.
- [134] A. Damjanovic, T. Ritz and K. Schulten, *Phys. Rev. E*, 1999, **59**, 3293–3311.
- [135] A. Gall, G. J. S. Fowler, C. N. Hunter and B. Robert, *Biochemistry*, 1997, **36**, 16282–16287.
- [136] A. Gall, R. J. Cogdell and B. Robert, *Biochemistry*, 2003, **42**, 7252–7258.
- [137] H. Rogl, W. Kühlbrandt and A. Barth, *Biochemistry*, 2003, **42**, 10223–10228.
- [138] M. F. Ng, Y. Zhao and G. H. Chen, *J. Phys. Chem. B*, 2003, **107**, 9589–9600.
- [139] X. J. Jordanides, G. D. Scholes and G. R. Fleming, *J. Phys. Chem. B*, 2001, **105**, 1652–1669.
- [140] X. Hu, T. Ritz, A. Damjanovic and K. Schulten, *J. Phys. Chem. B*, 1997, **101**, 3854–3871.
- [141] X. Hu, A. Damjanovic, T. Ritz and K. Schulten, *Proc. Nat. Acad. Sci. USA*, 1998, **95**, 5935–5941.
- [142] W. Wohlleben, T. Buckup, J. L. Herek, R. J. Codgell and M. Motzkus, *Biophys. J.*, 2003, **85**, 442–450.
- [143] P. Flükiger, H. P. Lüthi, S. Portmann and J. Weber, *MOLEKEL 4.0*, Swiss center for scientific computing technical report, 2000.
- [144] A. Dreuw, G. A. Worth., L. S. Cederbaum and M. Head-Gordon, *J. Phys. Chem. B*, 2004, **108**, 19049–19055.
- [145] G. F. Peter and J. P. Thorber, *Biol. Chem.*, 1991, **266**, 16745–16754.
- [146] H. van Amerongen and J. P. Dekker, in *Light-harvesting Antennas in Photosynthesis*, ed. B. R. Green and W. W. Parson, Kluwer Academic Publisher, 2003, pp. 219–251.
- [147] B. Demmig, K. Winter, A. Krüger and F.-C. Czygan, *Plant Physiol.*, 1987, **84**, 218–224.

- [148] J. Barber and B. Andersson, *Trends Biochem. Sci.*, 1992, **17**, 61–66.
- [149] P. Horton, A. V. Ruban and R. G. Walters, *Annu. Rev. Plant Physiol. Plant Mol. Biol.*, 1996, **47**, 655–684.
- [150] P. Müller, X.-P. Li and K. K. Niyogi, *Plant Physiol.*, 2001, **125**, 1558–1566.
- [151] N. E. Holt, G. R. Fleming and K. K. Niyogi, *Biochemistry*, 2004, **43**, 8281–8289.
- [152] H. Rogl and W. Kühnbrandt, *Biochemistry*, 1999, **38**, 16214–16222.
- [153] H. Rogl, R. Schödel, H. Lokstein, W. Kühnbrandt and A. Schubert, *Biochemistry*, 2002, **41**, 2281–2287.
- [154] A. M. Gilmore, *Physiol. Plant*, 1997, **99**, 197–209.
- [155] X.-P. Li, O. Bjorkman, C. Shih, A. R. Grossman, M. Rosenquist, S. Jansson and K. K. Niyogi, *Nature*, 2000, **403**, 391–395.
- [156] N. E. Holt, D. Zigmantas, L. Valkunas, X.-P. Li, K. K. Niyogi and G. R. Fleming, *Science*, 2005, **307**, 433–436.
- [157] A. M. Gilmore and H. Y. Yamamoto, *Proc. Natl. Acad. Sci. U.S.A.*, 1992, **89**, 1899–1903.
- [158] Y. Miloslavina, A. Wehner, P. H. Lambrev, E. Wientjes, M. Reus, G. Garab, R. Croce and A. R. Holzwarth, *FEBS Letters*, 2008, **582**, 3625–3631.
- [159] A. V. Ruban, R. Berera, C. Iliaia, I. H. M. van Stokkum, J. T. M. Kennis, A. A. Pascal, H. van Amerongen, B. Robert, P. Horton and R. van Grondelle, *Nature*, 2007, **450**, 575–578.
- [160] B. S. Hudson and B. E. Kohler, *Chem. Phys. Lett.*, 1972, **14**, 299–304.
- [161] B. S. Hudson and B. E. Kohler, *Ann. Rev. Phys. Chem.*, 1974, **25**, 437–460.
- [162] K. Schulten, I. Ohmine and M. Karplus, *J. Chem. Phys.*, 1976, **64**, 4422–4441.
- [163] P. Tavan and K. Schulten, *Phys. Rev. B*, 1987, **36**, 4337–4358.

- [164] R. J. Cave and E. R. Davidson, *J. Phys. Chem. B*, 1987, **91**, 4481–4490.
- [165] R. J. Cave and E. R. Davidson, *J. Phys. Chem. B*, 1988, **92**, 614–620.
- [166] G. Orlandi, F. Zerbetto and M. Z. Zgierski, *Chem. Rev*, 1991, **91**, 867–891.
- [167] W. J. Buma, B. E. Kohler and K. Song, *J. Chem. Phys.*, 1991, **94**, 6367–6376.
- [168] L. Serrano-Andrés, M. Merchán, I. Nebot-Gil, R. Lindh and B. O. Roos, *J. Chem. Phys.*, 1993, **98**, 3151–3162.
- [169] L. Serrano-Andrés, R. Lindh, B. O. Roos and M. Merchán, *J. Chem. Phys.*, 1993, **97**, 9360–9368.
- [170] R. P. Krawczyk, K. Malscha, G. Hohlneicher, R. C. Gillen and W. Domcke, *Chem. Phys. Lett.*, 2000, **320**, 535–541.
- [171] R. Pariser, *J. Chem. Phys.*, 1956, **24**, 250–268.
- [172] P. Strodel and P. Tavan, *J. Chem. Phys.*, 2002, **117**, 4677–4683.
- [173] K. Nakayama, H. Nakano and K. Hirao, *J. Quant. Chem.*, 1998, **66**, 157–175.
- [174] Y. Kurashige, H. Nakano, Y. Nakao and K. Hirao, *Chem. Phys. Lett.*, 2004, **400**, 425–429.
- [175] Polarization propagator ADC code written by A. B. Trofimov.
- [176] D. L. Phillips, M. Z. Zgierski and A. B. Myers, *J. Phys. Chem.*, 1993, **97**, 1800–1809.
- [177] D. G. Leopold, R. D. Pendley, J. L. Roebber, R. J. Hemley and V. Vaida, *J. Chem. Phys.*, 1984, **81**, 4218–4229.
- [178] K. L. D’Amico, C. Manos and R. L. Christensen, *J. Am. Chem. Soc.*, 1980, **102**, 1777–1782.
- [179] R. Snyder, E. Arvidson, C. Foote, L. Harrigan and R. L. Christensen, *J. Am. Chem. Soc.*, 1985, **107**, 4117–4122.

- [180] T. Fujii, A. Kamata, M. Shimizu, Y. Adachi and S. Maeda, *Chem. Phys. Lett.*, 1985, **115**, 369–372.
- [181] L. Serrano-Andrés and M. P. Fülcher, *J. Am. Chem. Soc.*, 1996, **118**, 12190–12199.
- [182] L. Serrano-Andrés and M. P. Fülcher, *J. Am. Chem. Soc.*, 1998, **120**, 10912–10920.
- [183] C. S. Page, M. Merchán, L. Serrano-Andrés and M. Olivucci, *J. Phys. Chem. A*, 1999, **103**, 9864–9871.
- [184] B. Proppe, M. Merchán and L. Serrano-Andrés, *J. Phys. Chem. A*, 2000, **104**, 1608–1616.
- [185] R. Cammi, B. Mennucci and J. Tomasi, *J. Phys. Chem. A*, 2000, **104**, 5631–5637.

List of Publications

- [1] M. Wormit and A. Dreuw, Carotenoid radical cation formation in LH2 of purple bacteria: a quantum chemical study, *J. Phys. Chem. B*, 2006, **110**, 24200–24206
- [2] J. H. Starcke, M. Wormit, J. Schirmer and A. Dreuw, How much double excitation character do the lowest excited states of linear polyenes have?, *Chem. Phys.*, 2006, **329**, 39–49
- [3] M. Wormit and A. Dreuw, Quantum chemical insights in energy dissipation and radical cation formation in light harvesting complexes, *Phys. Chem. Chem. Phys.*, 2007, **9**, 2917–2931
- [4] A. Dreuw and M. Wormit, Simple replacement of violaxanthin by zeaxanthin in LHC-II does not invoke chlorophyll fluorescence quenching, *J. Inorg. Biochem.*, 2008, **102**, 458–465
- [5] J. H. Starcke, M. Wormit and A. Dreuw, Unrestricted algebraic diagrammatic construction scheme of second order for the calculation of excited states of medium-sized and large molecules, *J. Chem. Phys.*, 2009, **130**, 024104
- [6] M. Wormit, P. H. P. Harbach, J. M. Mewes, S. Amarie, J. Wachtveitl and A. Dreuw, Excitation energy and electron transfer in light harvesting complexes - a theoretical perspective, *BBA Bioenergetics*, 2009, accepted for publication
- [7] J. H. Starcke, M. Wormit and A. Dreuw, Excited State Properties of Neutral Polyenyl Radicals and Polyene Radical Cations, 2009, submitted for publication
- [8] M. Wormit, M. Head-Gordon and A. Dreuw, Local Variant of the Algebraic Diagrammatic Construction, 2009, in preparation

Danksagung

An dieser Stelle möchte ich all den Personen danken, die zum Gelingen meiner Doktorarbeit auf die eine oder andere Weise beigetragen haben.

Herrn Prof. Dr. Andreas Dreuw danke ich außerordentlich dafür, dass er mir die Möglichkeit geboten hat, ohne Vorkenntnisse auf diesem interessanten und reizvollen Themengebiet in seiner Arbeitsgruppe zu promovieren. Durch seine exzellente Betreuung, die vielen hilfreichen Diskussionen und die freundschaftliche Art der Zusammenarbeit ist das Gelingen dieser Arbeit erst möglich geworden.

Herrn Prof. Dr. Martin Head-Gordon möchte ich für die freundliche Aufnahme in seine Arbeitsgruppe während meines Aufenthalts an der University of California, Berkeley danken. Die vielen interessanten und lehrreichen Diskussionen mit ihm und den Mitgliedern seiner Arbeitsgruppe haben sich sehr positiv auf den wissenschaftlichen Fortgang meiner Arbeit ausgewirkt.

Herrn Prof. Dr. Jochen Schirmer und Herrn Dr. Anthony Dutoi gilt mein Dank für die vielen Diskussionen und die Hilfe bei meinen Fragen zur Theorie und zur Implementierung von ADC.

Herrn Dr. Rainer Hegger danke ich für die hervorragende Administration der Computerinfrastruktur und die Möglichkeit mich daran zu beteiligen und kleinere Probleme auch kurzfristig selbst beheben zu können. Sein Büro stand für Fragen und Gespräche jeglicher Art jederzeit offen.

Bei Herrn Jan Hendrik Starcke und Herrn Jürgen Plötner möchte ich mich für vier Jahre gute Zusammenarbeit, die angenehme Büroatmosphäre und die vielen wissenschaftlichen und nicht wissenschaftlichen Diskussionen bedanken. Ebenso

danke ich Stefan, Philipp, Maxim, Miriam, Dirk, Jan und Daniel für die angenehme Arbeitsatmosphäre in unserer Arbeitsgruppe.

Bedanken möchte ich mich auch bei allen aktuellen oder ehemaligen Mitgliedern der Arbeitsgruppen Prof. Dr. Gerhard Stock und Prof. Dr. Josef Wachtveitl für die freundschaftliche Atmosphäre während und außerhalb der Arbeitszeiten.

Für das Korrekturlesen dieser Arbeit gilt mein Danke Jan Hendrik Starcke, Stefan Knippenberg, Dirk Rehn und meiner Freundin Isabel.

Zu guter letzt möchte ich noch meinen Eltern für die uneingeschränkte Unterstützung während meines persönlichen und beruflichen Werdegangs danken. Ohne sie wäre diese Arbeit nicht zustande gekommen.

LEBENS LAUF

Michael Wormit
geboren am 05.11.1977 in Speyer
ledig

SCHULBILDUNG

1984 – 1988	Grundschule Nord, Schifferstadt
1988 – 1997	Gymnasium im Paul-von-Denis Schulzentrum, Schifferstadt
Jun. 1997	Allgemeine Hochschulreife

WEHRDIENST

Nov. 1997 – Aug. 1998	Sanitätsregiment 5, Rennerod
-----------------------	------------------------------

STUDIUM

Okt. 1998 – Feb. 2004	Physikstudium an der Universität Heidelberg
Feb. 2003 – Feb. 2004	Diplomarbeit bei Prof. Dr. P. Bachert am Deutschen Krebsforschungszentrum (DKFZ), Heidelberg Thema: <i>Hochaufgelöste, lokalisierte $^1\text{H-NMR-Spektroskopie an schwer zugänglichen Körperregionen.$</i>
Feb. 2004	Diplom in Physik
seit Sep. 2004	Promotion bei Prof. Dr. A. Dreuw am Institut für physikalische und theoretische Chemie (IPTC) der Johann Wolfgang Goethe-Universität Frankfurt Thema: <i>Development and Application of Reliable Methods for the Calculation of Excited States: From Light-Harvesting Complexes to Medium-Sized Molecules</i>
Jun. 2007 – Aug. 2007	Dreimonatiger Forschungsaufenthalt in der Arbeitsgruppe von Prof. M. Head-Gordon an der University of California, Berkeley (DAAD Stipendium)

VORTRÄGE

- Mär. 2005 Winterseminar des IPTC. Titel: „Energy and Charge Transfer in LH2 Antenna Complexes of Purple Bacteria”
- Mär. 2007 Winterseminar des IPTC. Titel: „Theoretical View on Carotenoid Cation Formation in Light-Harvesting Complexes”
- Aug. 2007 Seminar der Gruppe von Prof. M. Head-Gordon. Titel: „Algebraic Diagrammatic Construction”
- Mai 2008 Seminar des SFB 472. Titel: „Theoretical View on Carotenoid Radical Cation Formation in Light-Harvesting Complexes”
- Dez. 2008 Seminar des IPTC. Titel: „The ADC Approach - Towards Efficient and Reliable Calculation of Excited States of Large and Medium-sized Molecules.”

POSTERPRÄSENTATIONEN

- Sep. 2005 Symposium für Theoretische Chemie (STC). Titel: „Charge and Energy Transfer in LH2 Complexes of Purple Bacteria - Studied by Means of TDDFT”
- Sep. 2006 STC. Titel: „Modelling Charge Transfer in LH2 Complexes of Purple Bacteria Using a TDDFT Approach”
- Sep. 2007 STC. Titel: „A Local Version of the Algebraic Diagrammatic Construction Scheme to Calculate Electronic Excited States of Large Molecules”
- Sep. 2008 STC. Titel: „Calculation of Electronic Excited States Using the Algebraic Diagrammatic Construction Scheme with Local Orbitals and Resolution-Of-The-Identity”

STIPENDIEN

- Sep. 2006 Reisestipendium der Freunde und Förderer der Universität Frankfurt zum Besuch des STC 2006
- Jun. 2007 – Aug. 2007 DAAD-Stipendium für eine dreimonatigen Forschungsaufenthalt an der University of California, Berkeley